UNIVERSITY *of* York

This is a repository copy of *Hyperpolarised benchtop NMR spectroscopy for analytical applications*.

Article:

Contents lists available at ScienceDirect

Progress in Nuclear Magnetic Resonance Spectroscopy

journal homepage: www.elsevier.com/locate/pnmrs

Hyperpolarised benchtop NMR spectroscopy for analytical applications

Ana I. Silva Terra, Daniel A. Taylor, Meghan E. Halse *

Department of Chemistry, University of York, York, YO10 5DD, UK

ARTICLE INFO

ABSTRACT

Benchtop NMR spectrometers, with moderate magnetic field strengths ($B_0 = 1 - 2.4$ T) and sub-ppm chemical shift resolution, are an affordable and portable alternative to standard laboratory NMR ($B_0 \geq 7$ T). However, in moving to lower magnetic field instruments, sensitivity and chemical shift resolution are significantly reduced. The sensitivity limitation can be overcome by using hyperpolarisation to boost benchtop NMR signals by orders of magnitude. Of the wide range of hyperpolarisation methods currently available, dynamic nuclear polarisation (DNP), *para*hydrogen-induced polarisation (PHIP) and photochemically-induced dynamic nuclear polarisation (photo-CIDNP) have, to date, shown the most promise for integration with benchtop NMR for analytical applications. In this review we provide a summary of the theory of each of these techniques and discuss examples of how they have been integrated with benchtop NMR detection. Progress towards the use of hyperpolarised benchtop NMR for analytical applications, ranging from reaction monitoring to probing biomolecular interactions, is discussed, along with perspectives for the future.

Contents

* Corresponding author.
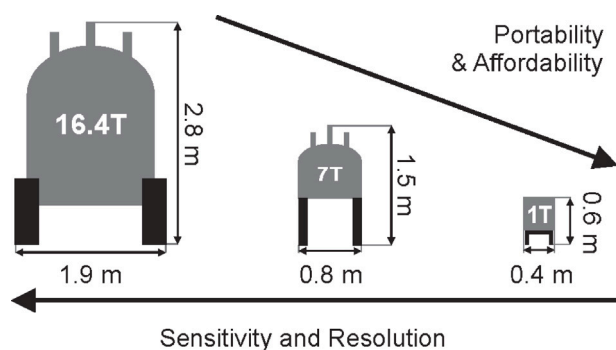 *E-mail address:* meghan.halse@york.ac.uk (M.E. Halse).

Fig. 1. Illustration of the relative dimensions of a range of NMR spectrometers (left to right): 16.4 T (700 MHz), 7 T (300 MHz), and 1 T (43 MHz) benchtop.

1. Introduction

Nuclear Magnetic Resonance (NMR) spectroscopy is a powerful analytical technique that is used throughout the chemical and physical sciences to provide detailed and quantitative information about the structure and dynamics of molecules. Modern NMR instrumentation exploits superconducting magnet technology to achieve high magnetic field strengths, with $B_0 = 28$ T (1.2 GHz) magnets now available [1]. High magnetic fields increase sensitivity and improve spectral resolution along the chemical shift axis. Chemical shift is defined in parts per million (ppm) of the nuclear Larmor frequency, which is directly proportional to B_0. Therefore, peak separation in frequency units (Hz) increases and chemical shift resolution improves as the strength of the magnetic field increases. For example, high-resolution ^{1}H NMR spectra are typically characterised by peak linewidths of around 1 Hz, which corresponds to a chemical shift resolution of less than 1 part per billion (ppb) in a field of $B_0 = 28$ T (1.2 GHz) but only 23 ppb at $B_0 = 1$ T (43 MHz). While high-resolution NMR spectrometers typically use a standard sample size, a 5 mm diameter NMR tube containing *ca.* 0.7 mL of solution, the physical size of the NMR magnet generally increases with the strength of the magnetic field (Fig. 1). As a result, high-field NMR spectrometers are expensive and are typically located in dedicated facilities managed by expert technical staff. Furthermore, most superconducting magnets also require regular input of liquid helium, a limited resource whose cost has seen dramatic increases in recent years [2].

NMR devices can be made smaller, cheaper and more portable by replacing the large superconducting magnet with compact designs based on permanent magnet arrays or electromagnets (Fig. 1) [3]. However, the magnetic field strengths that can be achieved using these technologies are typically lower by an order of magnitude or more when compared to superconducting magnets. Additionally, it is challenging to achieve the desired level of magnetic field homogeneity across the standard sample volume in a compact and portable instrument [4]. Therefore, NMR spectra acquired using compact NMR instruments have lower signal-to-noise ratios (SNRs) and can be more difficult to interpret, due to signal overlap and the effects of strong scalar coupling, than those acquired using a high-field laboratory NMR spectrometer. Furthermore, if a sufficient level of field homogeneity cannot be achieved to resolve chemical shift differences, limited chemical differentiation is possible within the NMR spectrum because only a single response is observed for each NMR-active nuclear isotope (^{1}H, ^{13}C, *etc.*), regardless of differences in chemical shift.

There is a long tradition, dating back to the very early years of magnetic resonance, of using low-field, low-resolution NMR devices for applications in, for example, the food and petrochemical industries [5–8]. These so-called time-domain NMR devices provide no detailed spectral information because they have insufficient magnetic field homogeneity. Instead, they are used to perform bulk measurements of

properties such as NMR relaxation times and molecular self-diffusion coefficients. These parameters report on molecular structure and dynamics and can be related to key macroscopic properties such as food spoiling [9], or the fluid properties of an oil reservoir [10].

Over the last decade, there has been a renaissance in the area of compact NMR with the introduction of commercial benchtop NMR spectrometers operating at magnetic field strengths of 1–3 T (^{1}H Larmor frequencies of 43–125 MHz) with field homogeneities <10 ppb allowing for peak linewidths <1 Hz [11–16]. These instruments are much more cost-effective than high-field spectrometers, being both cheaper to buy and having minimal maintenance costs, including no cryogen consumption. Furthermore, they are typically very robust and do not require routine expert technical maintenance and support. Benchtop NMR spectrometers have been used for a range of applications, including reaction monitoring inside a fume hood [17], detection of adulteration of dietary supplements with pharmaceutical substances [18], and at-line process monitoring and control in an industrial plant [19]. Whilst benchtop NMR spectrometers are able to interrogate any NMR-active nucleus, most applications target ^{1}H or other highly abundant, high receptivity nuclei (*e.g.*, ^{19}F [20,21], ^{31}P[22–24]) for samples in the tens to hundreds of millimolar concentration range.

A promising route for boosting the sensitivity of benchtop NMR is through the use of hyperpolarisation. Hyperpolarisation is a general term for a range of techniques that amplify NMR signals by creating a large population imbalance across the nuclear spin states. The signal in an NMR experiment arises from the Zeeman interaction between an ensemble of nuclear spins and an external magnetic field. In the presence of this field, a nucleus with spin quantum number $I = \frac{1}{2}$ (*e.g.*, ^{1}H, ^{13}C, ^{19}F) populates either the spin-up ($m_I = +\frac{1}{2}$, $|\alpha\rangle$) or spin-down ($m_I = -\frac{1}{2}$, $|\beta\rangle$) energy state (Fig. 2a). The difference in population between these two states, the so-called polarisation (P), gives rise to a net bulk magnetisation within the sample along the direction of the external field. The maximum signal observed in an NMR experiment is proportional to the size of the net magnetisation and hence the polarisation. At thermal equilibrium, polarisation is governed by Boltzmann statistics and is defined in Eq. (1), where γ is the gyromagnetic ratio (a property of the nucleus), B_0 is the strength of the external magnetic field, T is the temperature, and k_B is the Boltzmann constant.

$$P = \tanh \frac{\gamma B_0 \hbar}{2 k_B T} \simeq \frac{\gamma B_0 \hbar}{2 k_B T} \tag{1}$$

The expression on the right-hand side of Eq. (1) corresponds to the high-temperature approximation, which holds for all temperatures above a few milliKelvin for nuclei. The temperature dependence of polarisation in a field of $B_0 = 1$ T is shown in Fig. 2c for ^{1}H (black) and ^{13}C (red) nuclei, with the thermal polarisation for an electron spin (blue) shown for comparison. The differences between these curves reflect the relative sizes of their gyromagnetic ratios ($|\gamma_{e^-}| > |\gamma_{^1H}| > |\gamma_{^{13}C}|$).

As shown schematically in Fig. 2a, the difference in population at thermal equilibrium at room temperature is very small (3.5 ppm T^{-1} for ^{1}H at 295 K). This is because the difference in energy between the two nuclear spin states is small compared to the available thermal energy. Under hyperpolarisation conditions, one of these states is overpopulated, as shown schematically in Fig. 2b, generating polarisation levels up to tens of percent. This gives rise to a larger net bulk magnetisation and therefore an enhanced NMR signal. Since the level of polarisation is very small at thermal equilibrium (tens of ppm), signal enhancements of many orders of magnitude are possible.

A wide range of hyperpolarisation methods have been developed, with the most widely used falling within one of the following broad categories: brute force hyperpolarisation, dynamic nuclear polarisation (DNP), spin-exchange optical pumping (SEOP), chemically-induced dynamic nuclear polarisation (CIDNP), and *para*hydrogen-induced polarisation (PHIP). These methods differ based on the source of polarisation and the method and conditions of polarisation transfer [25].
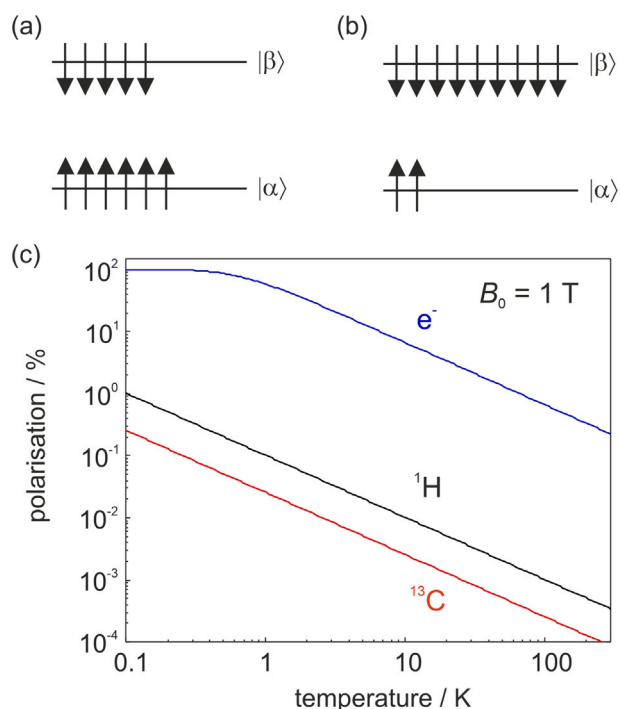
Fig. 2. (a) Schematic representation of the relative populations of the two nuclear spin energy levels, spin-up ($m_I = +\frac{1}{2}$, $|\alpha\rangle$) and spin-down ($m_I = -\frac{1}{2}$, $|\beta\rangle$), for an $I = \frac{1}{2}$ nucleus (*e.g.*, ^{1}H, ^{13}C) at thermal equilibrium at room temperature. (b) Schematic representation of hyperpolarisation, where the higher energy state ($|\beta\rangle$) has been overpopulated, giving rise to a larger population difference and therefore a higher polarisation. (c) Thermal equilibrium spin polarisation percentage as a function of temperature at $B_0 = 1$ T for an electron spin (blue), for ^{1}H (black), and for ^{13}C (red) nuclei.

2. Dynamic nuclear polarisation (DNP)

DNP, first proposed by Overhauser in 1953 [26], uses unpaired electrons as the source of polarisation. Overhauser theorised that if the electron paramagnetic resonance (EPR) of the conduction electrons in a metal were saturated, then cross-relaxation from the electrons to the nuclei in the metal would lead to a build-up of enhanced nuclear polarisation, with a limiting enhancement factor equal to the ratio of the electron and nuclear gyromagnetic ratios [27]. A very interesting account of this remarkable prediction and how it came to be published can be found in Overhauser's memoir in *eMagRes* published in 2007 [26]. Overhauser's prediction was verified experimentally later the same year by Carver and Slichter, who observed significant increases in the ^{7}Li NMR signal for a sample of lithium metal dispersed in oil following saturation of the EPR line of the conduction electrons [28]. Whilst in this first demonstration of DNP the conduction electrons in a metal were used as the source of polarisation, in the majority of DNP experiments a source of unpaired electrons, such as paramagnetic ions or a stable free radical, is added to the sample to enable hyperpolarisation.

Early applications of DNP included ^{13}C NMR of solids such as coal and diamond [29]. However, these experiments were largely limited to relatively low magnetic fields (≤ 1.4 T) due to microwave instrumentation limitations. This challenge was overcome by Griffin and co-workers in the 1990s, who introduced the gyrotron as a means of generating high-powered microwaves in the hundreds of gigahertz frequency range to achieve EPR saturation inside a standard high-field NMR spectrometer ($B_0 \geq 4.7$ T) [30]. This was combined with cryogenic magic angle spinning (MAS) at temperatures <100 K to achieve NMR signal enhancements of up to 100-fold on biomolecules in frozen solution [31]. Despite significant instrumentation and operational costs, the MAS-DNP approach has developed into a powerful analytical tool for the study of proteins in the solid state, particularly membrane proteins and amyloid fibrils [32,33], and in the field of materials science for the study of polymers, porous materials, nanoparticles, and pharmaceuticals [34, 35].

DNP can also be used to enhance NMR signals in the liquid state, as first demonstrated by Bennett and Torrey in 1957 [36]. In liquids, the dominant mechanism of polarisation transfer is the Overhauser effect and so liquid-state DNP is commonly known as Overhauser DNP (ODNP). ODNP enhancement factors are highly dependent on local molecular dynamics, making it a unique tool for the study of molecular motion in the hydration shell of biomolecules [37].

In 2003, Ardenkjær-Larsen and co-workers proposed dissolution DNP (dDNP), a novel approach that combines the high electron polarisation levels and efficient polarisation transfer at cryogenic temperatures with the chemical shift resolution and potential clinical applications associated with room-temperature NMR and magnetic resonance imaging (MRI) [38]. Similar to MAS DNP, dissolution DNP has significant instrumentation and operational costs. Nevertheless it has many interesting applications, such as the production of hyperpolarised contrast agents for metabolic ^{13}C MRI for use in diagnosis and monitoring treatment response [39–42]. In addition, dDNP has shown great promise for mixture analysis in fields such as metabolomics, due to the high levels of ^{13}C polarisation that can be achieved for samples at natural isotopic abundance and the diversity of molecules that can be efficiently enhanced [43,44].

Benchtop NMR spectroscopy is predominantly performed on liquid-state samples. Therefore, in the following sections we focus on ODNP and dDNP, where detection of the hyperpolarised NMR signal is achieved in solution.

2.1. Overhauser dynamic nuclear polarisation (ODNP)

2.1.1. Background theory of ODNP

DNP *via* the Overhauser effect can be understood by considering the energy level diagram and associated transition probabilities, shown

When evaluating a hyperpolarisation method for a potential application, key factors to consider are the instrumentation requirements, the level of polarisation enhancement that can be achieved, and the range of species whose NMR signals can be enhanced. For analytical applications, the ideal method would have limited instrumentation requirements and deliver high levels of renewable polarisation for all target nuclei in the sample. However, all hyperpolarisation methods present trade-offs between these aspects, and therefore have both strengths and weaknesses depending on the desired application. For combination with benchtop NMR spectroscopy, the instrumentation requirements of the hyperpolarisation method are of particular relevance, due to the desire to maintain the overall affordability and portability of the technique. Another key consideration is the reproducibility of the hyperpolarisation response and scope for quantification. Quantification is a particular challenge, because unlike standard NMR, hyperpolarised NMR signal amplitudes depend not only on the relative concentration of a given analyte, but also on the efficiency of the hyperpolarisation process. For all methods, hyperpolarisation efficiency involves a complex interplay between experimental and sample-specific factors. Therefore a robust and quantitative interpretation of hyperpolarised signals poses a significant challenge.

In this article, we focus in particular on the DNP, PHIP, and CIDNP hyperpolarisation methods, which have to date shown the most promise for integration with benchtop NMR spectroscopy for analytical applications. We provide a general theoretical background for each technique, and describe how they have been integrated with benchtop NMR spectroscopy. Progress towards analytical applications of hyperpolarised benchtop NMR spectroscopy is discussed, along with perspectives for the future.

Fig. 3. Energy level diagram and transition probabilities ($w_0^{IS}, w_1^I, w_1^S, w_2^{IS}$) for a hyperfine-coupled electron (S) and nucleus (I), where the nucleus has spin $I = \frac{1}{2}$ and a positive gyromagnetic ratio (*e.g.*, ^{1}H or ^{13}C). The kets $|m_S, m_I\rangle$ describe each state, where α is $m = +\frac{1}{2}$ and β is $m = -\frac{1}{2}$. The electron spins possess a negative gyromagnetic ratio and so its lowest energy state is the spin-down ($m_S = -\frac{1}{2}$) state, whilst for the nucleus it is spin-up ($m_I = +\frac{1}{2}$).

in Fig. 3, for an isolated electron–nucleus spin system coupled *via* a hyperfine interaction, where the nucleus has spin $I = \frac{1}{2}$ and a positive gyromagnetic ratio (*e.g.*, ^{1}H, ^{13}C).

The transition probabilities define the rate at which the populations of the different energy levels come to equilibrium with one another within this isolated spin system. Following Solomon [45], and using the transition probabilities in Fig. 3 ($w_0^{IS}, w_1^I, w_1^S, w_2^{IS}$), the time rate of change of the nuclear magnetisation, M_z^I, is given by Eq. (2), where $M_{z,0}^I$ and $M_{z,0}^S$ the thermal equilibrium magnetisations for the nuclear and electron spins, respectively.

$$
\begin{aligned}
\frac{dM_z^I(t)}{dt} &= -(\rho_I + R_{1,dia})(M_z^I(t) - M_{z,0}^I) \\
&\quad - \sigma_{IS}(M_z^S(t) - M_{z,0}^S) \\
\rho_I &= w_0^{IS} + 2w_1^I + w_2^{IS} \\
\sigma_{IS} &= w_2^{IS} - w_0^{IS}
\end{aligned}
\tag{2}
$$

The first term on the right-hand-side in Eq. (2) corresponds to the longitudinal nuclear spin relaxation. The longitudinal nuclear relaxation rate has two contributions: ρ_I and $R_{1,dia}$. ρ_I is the rate of relaxation due to the electron–nuclear interaction and is defined in terms of the transition probabilities illustrated in Fig. 3. $R_{1,dia}$, includes all other contributions to the nuclear relaxation rate and accounts for the relaxation of the nuclei in the sample that are not in direct contact with the unpaired electron and therefore do not experience a hyperfine interaction. The second term in Eq. (2) corresponds to the cross-relaxation between the electron and nuclear spins, where σ_{IS} is the cross-relaxation rate. During an ODNP experiment, microwave (MW) irradiation is applied at the EPR frequency to saturate the electron spins. In the case of complete saturation, this equalises the electron spin populations and reduces the electron magnetisation to zero. More generally, we define a steady-state electron magnetisation, $M_{z,SS}^S$, that is established under continuous MW irradiation. Under steady-state conditions, where $\frac{dM_z^I}{dt} = 0$, we can express the steady-state nuclear magnetisation, $M_{z,SS}^I$, as a function of $M_{z,SS}^S$ (Eq. (3)).

$$
M_{z,SS}^I = M_{z,0}^I - \frac{\sigma_{IS}}{\rho_I + R_{1,dia}}(M_{z,SS}^S - M_{z,0}^S)
\tag{3}
$$

Eq. (3) can be re-written to describe the ODNP enhancement factor, ϵ, as a function of a coupling factor (ξ), a leakage factor (f), and a saturation factor (s) (Eq. (4)).

$$
\epsilon = \frac{M_z^I(t)}{M_{z,0}^I} = 1 - \xi f s \frac{|\gamma_S|}{\gamma_I}
\tag{4}
$$

The final factor in Eq. (4) corresponds to the ratio of the equilibrium electron and nuclear polarisation (Eq. (5)).

$$
\frac{M_{z,0}^S}{M_{z,0}^I} = -\frac{|\gamma_S|}{\gamma_I}
\tag{5}
$$

For ^{1}H nuclei, this factor is approximately 658 and represents the maximum theoretical ODNP enhancement. In principle, any NMR-active nucleus can be enhanced by ODNP, as long as it experiences a suitable coupling to the electron spin. Indeed, due to their lower gyromagnetic ratio, nuclei other than ^{1}H have a larger maximum ODNP enhancement factor and thus greater hyperpolarisation potential. The extent to which this maximum enhancement factor can be achieved depends on the other three parameters in Eq. (4). The saturation factor, s, quantifies the extent of saturation of the electron transition during MW irradiation (Eq. (6)).

$$
s = \frac{(M_{z,0}^S - M_{z,SS}^S)}{M_{z,0}^S}
\tag{6}
$$

The saturation factor will approach unity if there is sufficient MW power to overcome the electron relaxation rates and achieve a steady-state electron polarisation of zero. Therefore, paramagnetic species with a narrow EPR line (long transverse electron relaxation time, T_{2e}) and long electron longitudinal relaxation time, T_{1e}, are desirable for achieving optimal ODNP enhancements with minimum MW power. Minimising the required MW power is desirable from an instrumental perspective and reduces the extent of sample heating, which can be a significant challenge for ODNP in the case of samples with strong MW absorption (*e.g.*, aqueous solutions).

The leakage factor, f, is the fraction of the total nuclear relaxation rate that is due to the paramagnetic interaction (Eq. (7)). This can be calculated from measurements of the nuclear longitudinal relaxation rate of the sample in the presence ($R_1 = \rho_I + R_{1,dia}$) and absence ($R_1 = R_{1,dia}$) of the paramagnetic species.

$$
f = \frac{\rho_I}{\rho_I + R_{1,dia}} = 1 - \frac{R_{1,dia}}{\rho_I + R_{1,dia}}
\tag{7}
$$

As the contribution to the nuclear relaxation rate from non-paramagnetic sources becomes insignificant compared to the paramagnetic relaxation contribution, f approaches unity. This is optimal because the paramagnetic interaction drives the desired polarisation transfer mechanism, and so any significant source of non-paramagnetic nuclear relaxation reduces the build-up of nuclear polarisation and limits the enhancement factor. The paramagnetic component of relaxation rate, ρ_I, has been shown to increase linearly with concentration of the paramagnetic species, as this increases the interactions between the unpaired electrons and nuclei in the sample [46]. A leakage factor approaching unity can be achieved by increasing the concentration of the paramagnetic species. However, this reduces the nuclear transverse relaxation time, T_2, and causes line broadening. Therefore, in practice there exists an upper limit to the concentration of paramagnetic species that can be added to the sample while maintaining sufficient spectral resolution.

The coupling factor, ξ, is defined as the ratio between the cross-relaxation rate and the rate of paramagnetic relaxation of the nucleus (Eq. (8)).

$$
\xi = \frac{\sigma_{IS}}{\rho_I} = \frac{w_2^{IS} - w_0^{IS}}{w_0^{IS} + 2w_1^I + w_2^{IS}}
\tag{8}
$$

ξ is dependent on the relative size of the zero-quantum (w_0^{IS}), single-quantum (w_1^I), and double-quantum (w_2^{IS}) transition probabilities. To
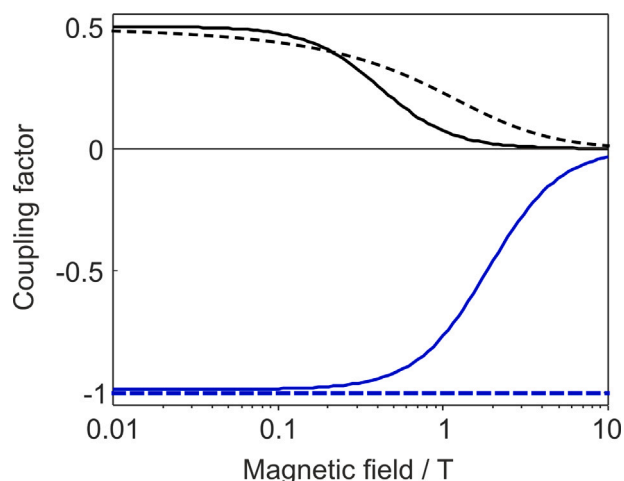
Fig. 4. Coupling factor (ξ) as a function of magnetic field strength for pure dipolar coupling modulated by rotational diffusion (solid black line), translational diffusion (dashed black line), pure scalar coupling (blue dashed line), and scalar coupling with 1% contribution from dipolar nuclear relaxation (blue solid line) calculated according to the formalism from Ref. [48]. Dipolar coupling factors were calculated using the relevant equations from Ref. [47] with a correlation time of $\tau = 25$ ps.

maximise the coupling factor, cross-relaxation between the electron and nuclear spins, which acts to increase the nuclear polarisation, must be more efficient than the nuclear relaxation, which acts to return the nuclear polarisation to equilibrium.

For relaxation to occur between two spin states it is necessary to have a coupling term that connects the two states, and the strength of this coupling must be modulated at the transition frequency between the states. Therefore, the relative size of the transition probabilities, and hence ξ, will depend on the coupling mechanism, the relative strength of the coupling between the different states and the frequency of modulation. The strength of the magnetic field, B_0, also contributes as this determines the transition frequency between the spin states. In the liquid state, coupling between the unpaired electron and target nuclei can occur through space (*via* dipolar coupling) or through a scalar coupling interaction between the nuclei and the unpaired electron spins.

Dipolar coupling drives zero-, single- and double-quantum transitions (Fig. 3) and is dependent on both the relative orientation of the axis between the coupled spins and the magnetic field, B_0, and the distance between the coupled spins. Therefore, the strength of the intermolecular dipolar interaction in liquids is modulated by both rotational and translational diffusion, with the frequency of modulation determined by the correlation times (τ) for these diffusion processes. At low magnetic field strengths, the inverses of typical liquid-state correlation times (*i.e.*, the rates of molecular rotation and translational diffusion) are much greater than the Larmor frequencies of both the electron and nuclear spins ($\tau^{-1} \gg \omega_S \gg \omega_I$). In this case, the coupling factor tends to a maximum value of $\xi = 0.5$. However, as B_0 increases, the system enters a regime where the electron Larmor frequency is larger than the inverse of the correlation time ($\omega_S > \tau^{-1}$). In this regime, the single-quantum transition probabilities increase such that nuclear relaxation dominates over cross-relaxation and ξ tends to zero [47]. This is illustrated by the magnetic field dependence of the dipolar coupling factor presented in Fig. 4 for pure rotational diffusion (solid black line) and pure translational diffusion (dashed black line) with $\tau = 25$ ps.

Scalar coupling between an unpaired electron and a nucleus, also known as the Fermi contact interaction, arises from electron density in *s*-orbitals at the nucleus. Therefore, it only occurs for nuclei on the molecule bearing the unpaired electron, or if the molecule containing the target nucleus binds to the paramagnetic species. Scalar coupling

between an unpaired electron and target nuclei gives rise to relaxation if the coupling is modulated either by chemical exchange (scalar relaxation of the first kind), or by rapid relaxation of one of the spins (scalar relaxation of the second kind). Unlike dipolar coupling, scalar coupling only drives zero-quantum transitions. Therefore it only contributes to the zero-quantum transition probability, w_0^{IS}. According to Eq. (8), this means that the coupling factor for pure scalar relaxation is $\xi = -1$ (blue dashed line in Fig. 4). However, it is necessary to consider the relative contribution of other relaxation mechanisms (*e.g.*, dipolar relaxation) to the transition probabilities in order to correctly predict the observed enhancement factor as a function of magnetic field. The field dependence of the scalar coupling factor, calculated with a 1% contribution from dipolar relaxation following the formalism of Loening et al. [48], for a correlation time of $\tau = 25$ ps is presented in Fig. 4 (blue solid line). As with the case of pure dipolar coupling, the scalar coupling factor tends to zero at high magnetic field strengths. However, as illustrated by the solid blue line in Fig. 4, the reduction in the coupling factor is due to relaxation from other sources (*e.g.*, dipolar coupling). Therefore, for polarisation agents that interact with the target nuclei *via* the scalar coupling mechanism, non-zero ODNP enhancements can still be observed at the higher magnetic field strengths of standard NMR spectrometers if other sources of relaxation can be minimised [48].

Whilst endogenous paramagnetic species can be used for ODNP, in the majority of experiments a polarising agent is added to the sample, in the form of paramagnetic metal ions or a stable organic radical. Nitroxide radicals such as TEMPO (2,2,6,6-tetramethylpiperidin-1-oxyl), TEMPOL and TEMPONE (4-hydroxy- and 4-oxo-TEMPO, respectively) have been widely studied for use in ODNP because they are stable, have relatively narrow EPR lines, and are biocompatible [49]. Nitroxide radicals have been found to have a negligible scalar relaxation contribution for ^{1}H hyperpolarisation, meaning their coupling factors are dominated by dipolar relaxation with a maximum value of $\xi = 0.5$ in relatively low magnetic fields ($B_0 < 1$ T) [46,49,50]. However, it should be noted that this is not always the case for ODNP of other nuclei. For example, Küçük et al. found a significant scalar coupling contribution to the coupling factor for ^{13}C in the methyl group of acetone, where TEMPOL was used as the stable free radical [50].

2.1.2. Integration of ODNP with benchtop NMR detection

The first compact ODNP-enhanced NMR systems were introduced by Armstrong et al. [51] and Münnemann et al. [52] in 2008. In both cases, a permanent magnet array with a field of $B_0 = 0.3$–0.35 T was chosen as this corresponds to an EPR frequency in the X-band (8–12 GHz), where microwave instrumentation is readily available, and the dipolar coupling factor is expected to be close to $\xi = 0.5$ for typical correlation times in liquid-state NMR samples (Fig. 4). Armstrong et al. demonstrated a maximum ^{1}H enhancement factor of -130 for an aqueous solution of ^{15}N-substituted TEMPONE [51], whilst Münnemann et al. measured a maximum enhancement factor of -50 for a solution of a nitroxide spin labelled cationic polyelectrolyte in 55:45 (vol %) glycerol–water [52]. Whilst these enhancement factors show promise, the NMR detection fields used in these instruments were of insufficient homogeneity to provide any chemical shift resolution, limiting spectroscopic applications. More recently, Überrück et al. presented an X-band ODNP system that includes a 0.34 T NMR magnet that can achieve a linewidth on the order of 3 ppm using passive shimming [53]. Whilst maximum ODNP enhancements for water of -140, comparable to that of Armstrong et al., are reported, the maximum ODNP enhancements for the ^{1}H chemical shift resolved spectrum of acetic acid were -12 and -35 for the methyl and carboxylic acid resonances, respectively [53]. Similarly, Keller et al. have presented a 0.35 T ODNP instrument that incorporates electronic shimming to achieve linewidths of <1 ppm. Enhancement factors on the order of -30 were observed for a wide range of chemical systems [54]. While the absolute linewidths of 0.66 Hz achieved by Keller et al. are similar to those in commercial

benchtop NMR spectrometers, the resolution on the ppm scale is limited at 0.35 T by the [1]H Larmor frequency (15 MHz).

Lee and co-workers have demonstrated ODNP on a 1.4 T (60 MHz) benchtop NMR spectrometer [55]. However, these experiments were limited by the lack of chemical shift resolution due to the inhomogeneity of the detection field and the very high levels of radical concentration (500 mM TEMPOL) that were required to observe a maximum enhancement factor of −40 for water [55]. Significant ODNP enhancements on the order of −20 have been reported in magnetic fields up to 9.2 T for aqueous solutions of nitroxide radicals in the tens of mM concentration regime, despite many theoretical models predicting negligible enhancements in this regime [56]. Therefore efficient *in situ* ODNP in the 1–2 T field strengths of commercial benchtop NMR spectrometers should be achievable. However, a key challenge of performing liquid-state ODNP at 1–2 T magnetic field strengths is the significant dielectric sample heating during Q-band MW irradiation, particularly for strongly absorbing aqueous samples. Effectively limiting and/or dissipating this heat deposition is critical, in particular for permanent-magnet-based benchtop NMR spectrometers whose field homogeneity and hence spectral resolution are highly sensitive to temperature gradients. Interestingly, in the experiments of Lee et al. [55], the increase in sample temperature under MW irradiation was found to increase the observed ODNP factor. This was attributed to an increase in the rate of molecular motion leading to a higher ODNP coupling factor.

Another example of ODNP in the field range of benchtop NMR spectrometers was recently presented by Reinhard et al., who performed their experiments using a hybrid EPR/NMR system operating at 1.2 T with limited MW power to prevent extreme sample heating [57]. [31]P ODNP enhancements of +360 were observed for triphyenylphosphine in benzene [57]. This large enhancement corresponds to a negative coupling factor $\xi = -0.312$, which is indicative of polarisation transfer *via* scalar coupling. The authors attribute the presence of a strong hyperfine interaction in this case to the formation of a weak complex between the phosphine and the aromatic radical *via* non-covalent interactions. While this interaction was found to be particular to this chemical system, these results demonstrate that large ODNP enhancements can, in favourable cases, be obtained in the typical field strengths of benchtop NMR spectrometers.

A flow approach to combining ODNP with benchtop NMR spectroscopy was demonstrated by Kircher et al. in 2021 [58]. In this work, ODNP transfer was carried out at 0.35 T followed by enhanced signal detection in a commercial 1 T (43 MHz) benchtop NMR spectrometer. This was achieved by continuously flowing the sample, first through a 0.35 T magnet under MW irradiation, and then through the 1 T benchtop NMR spectrometer for signal detection (Fig. 5) [58]. A key to the success of this experiment was the use of an immobilised radical matrix as the source of unpaired electrons [59–61]. The radical matrix was fixed within the 0.35 T magnet, such that the nuclear relaxation enhancement caused by electron–nuclear interactions was only experienced by the sample within the ODNP polariser, where it helps to drive polarisation transfer, and not during transport to the NMR detector. This work builds on the solid–liquid intermolecular transfer method introduced by Dorn and co-workers in the late 1980s, where ODNP at 0.33 T was coupled with high-field (4.7 T, 200 MHz) NMR detection [62–64]. Using the experimental setup in Fig. 5, Kircher et al. report enhancements on the order of −40 for water and acetonitrile in an equimolar mixture at a continuous flow rate of up to 2 mL min⁻¹ [58]. While this paper focuses solely on ^{1}H detection, the authors highlight that it is expected that this flow-based ODNP approach should also be highly effective for polarising other less sensitive nuclei, such as ^{13}C and [31]P. Indeed, observed hyperpolarisation levels would be expected to be higher in many cases due to the longer relaxation times (and hence hyperpolarisation lifetimes) of low-gyromagnetic ratio nuclei when compared to ^{1}H, leading to reduced loss of hyperpolarisation during transport between the ODNP polariser and the NMR detector. A
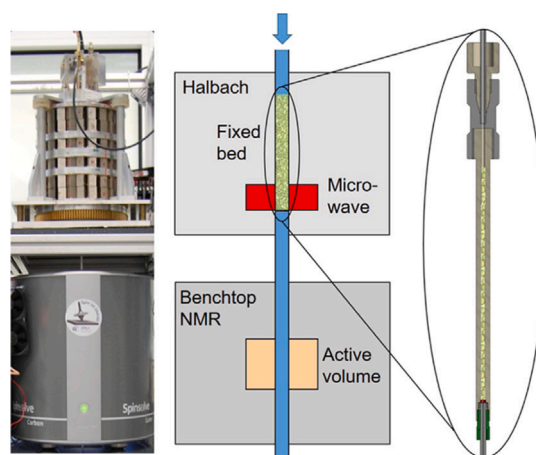

Fig. 5. Experimental setup of Keller et al. for ODNP-enhanced continuous-flow 1 T benchtop NMR spectroscopy using an immobilised radical matrix within a Halbach magnetic array (0.34 T). Reprinted with permission from R. Kircher, H. Hasse, K. Münnemann, Analytical Chemistry 93 (25) (2021) 8897–8905. Copyright 2021 American Chemical Society.

particular advantage of this approach is that it combines the efficiency of ODNP at 0.33 T with the spectral resolution provided by the 1 T benchtop NMR spectrometer.

ODNP has many potential advantages for integration with benchtop NMR spectroscopy, using either the *in situ* or flow-based approaches discussed above. These include the ability to hyperpolarise different nuclear isotopes in a wide range of molecules, and the relative simplicity and affordability of the instrumentation, which does not require cryogens or strong magnetic fields. However, one disadvantage is the limit on the enhancement factor imposed by the nature of the Overhauser effect in liquids (Eq. (4)), particularly for ^{1}H, which has a high gyromagnetic ratio and relatively short hyperpolarisation lifetimes. In order to significantly increase the enhancement factor, DNP needs to take place at higher fields and/or lower temperatures, where electron polarisation is higher, and/or under conditions of more efficient polarisation transfer throughout the sample.

2.2. Dissolution dynamic nuclear polarisation (dDNP)

2.2.1. Background theory of dDNP

Dissolution DNP provides a route to much higher enhancement factors than ODNP, whilst maintaining liquid-state NMR detection [38]. In dDNP, polarisation transfer takes place at cryogenic temperatures ($1.2 < T < 4.2$ K) in a strong magnetic field ($3.35 < B_0 < 10$ T), prior to rapid dissolution for detection in the liquid state. The instrumentation required to perform dDNP is illustrated schematically in Fig. 6.

Dissolution DNP has two key advantages in terms of the level of achievable nuclear hyperpolarisation. Firstly, under cryogenic conditions in a strong magnetic field, the electron polarisation approaches unity (Fig. 2). Secondly, spin diffusion (*i.e.*, the transfer of polarisation between nuclear spins mediated by dipole–dipole coupling) [65], provides a mechanism for efficient transport of hyperpolarisation from the source (the region immediately surrounding the paramagnetic species where nuclear relaxation times are very short), to the bulk of the sample (where nuclear relaxation times are much longer) [66]. This enables significant build-up of nuclear hyperpolarisation on the timescale of T_1.

In the original experiments of Ardenkjaer-Larsen and co-workers, 42% [13]C polarisation of urea in the solid state was obtained with a build-up time constant of 4900 s (82 min), where the ^{13}C hyperpolarisation lifetime at 1.2 K was measured to be 28,200 s (470 min) [38]. The polarisation build-up time can be reduced to tens of minutes by first transferring polarisation to ^{1}H, which typically has much shorter
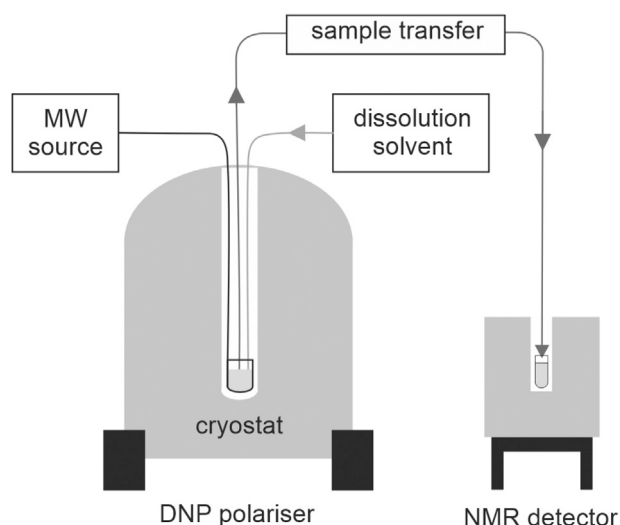
Fig. 6. Schematic of the instrumentation required to carry out a dissolution DNP experiment. The DNP polariser contains a strong magnet, typically a superconducting magnet with a field in the range $3.35 < B_0 < 10$ T, a cryostat operating within the range $1.2 < T < 4.2$ K, a source of MW irradiation, a source of hot solvent for the dissolution step, and a mechanism for rapid sample transfer to the NMR spectrometer for detection.

T_1, and then transferring this to ^{13}C *via* cross-polarisation [67,68]. Following rapid dissolution and transfer to the NMR spectrometer, dDNP can deliver signal enhancements of >10,000-fold, a dramatic improvement over ODNP [38]. However, the necessary freezing of the sample to build up hyperpolarisation, then followed by dissolution with hot solvent for liquid-state NMR detection, means that, in practice, a single sample is only hyperpolarised once. This is a limitation in the context of analytical applications because the sample can only be analysed over the relatively limited period (typically tens of seconds) of the hyperpolarisation lifetime in solution. Furthermore, the cost of the dDNP instrumentation is very large compared to that of a benchtop NMR spectrometer. Nevertheless, the very high levels of signal enhancement that can be achieved, and the broad range of chemical species that can, in principle, be hyperpolarised, make dDNP an important technology to consider in the context of hyperpolarised benchtop NMR spectroscopy.

A well-executed dDNP experiment requires optimisation of several different elements, from sample composition to instrumental setup. In the following, we provide a short summary of some of the key elements of dDNP. A comprehensive guide outlining practical aspects for execution of dDNP experiments can be found in the review by Elliott et al. [69]

The first step of a dDNP experiment is to homogeneously freeze the sample, doped with an optimal concentration of the paramagnetic DNP agent (typically on the order of 10–50 mM), into a glassy matrix. To achieve this, the sample of interest (*i.e.*, the target molecule or mixture of molecules) is first dissolved in solvent, often a mixture of D_2O and H_2O, along with a glassing agent such as glycerol or dimethylsulfoxide (DMSO), and the paramagnetic DNP agent. The DNP agent is typically either a nitroxide radical such as TEMPOL [70], or an aromatic radical such as trityl [71]. Next, the sample is rapidly frozen to cryogenic temperatures ($1.2 < T < 4.2$ K) by inserting it into a reservoir of liquid helium within the DNP polariser. This reservoir sits within a superconducting magnet, which provides a strong magnetic field ($3.35 < B_0 < 10$ T). Once frozen, the electron spins within the DNP polarising agent come to rapid thermal equilibrium to produce an electron spin polarisation approaching unity, according to Eq. (1).

The next step of the dDNP experiment is polarisation transfer to the target nuclei. This is achieved by irradiating at or near the EPR

frequency of the free radical. A number of polarisation transfer mechanisms have been identified and studied in the solid state in the context of MAS-DNP and dDNP. These include the Overhauser effect (OE) [28,72], the solid effect (SE) [73,74], the cross effect (CE), and thermal mixing (TM) mechanisms [75–79]. In insulating solids, polarisation transfer by the OE has only been observed for a limited range of radicals and is typically less efficient than the SE; however, it has been found to have more favourable scaling properties with magnetic field compared to SE and CE, and is therefore of interest for ultra-high-field DNP applications [80,81]. The CE and TM mechanisms require a coupled three-spin system involving two electrons and a nucleus, where the frequency difference between the two electron spins matches the Larmor frequency of the nuclear spin [79]. A wide range of biradicals that exploit the CE have been designed to provide efficient hyperpolarisation in high-field MAS-DNP experiments [82,83]. Dissolution DNP, however, is typically achieved using a disperse monoradical, where polarisation transfer is dominated by the SE [69].

The solid effect can be understood with reference to the energy level diagram in Fig. 7, which presents the same hyperfine-coupled electron–nuclear spin system as in Fig. 3. The grey circles represent the relative populations of each of the energy levels. For the purpose of this discussion, we assume that at thermal equilibrium within the DNP polariser the electron spin is fully polarised in its lower energy state, $|\beta\rangle$, and the nuclear spins are roughly evenly populated across their two spin states (*i.e.*, there is negligible nuclear polarisation). During polarisation transfer, the system is irradiated at a microwave frequency equal to either the sum ($\omega_{DQ} = \omega_S + \omega_I$) of or difference ($\omega_{ZQ} = \omega_S - \omega_I$) between the electron and nuclear Larmor frequencies, to excite either the double-quantum (DQ) (Fig. 7a, centre) or zero-quantum (ZQ) (Fig. 7b, centre) transition, respectively. By saturating one of these transitions, the populations of the connected states are equalised. Subsequent rapid relaxation to the lower energy $|\beta\rangle$ state for the electron spin gives rise to overpopulation of the $|\beta\rangle$ and $|\alpha\rangle$ states of the nuclear spin, for the cases of DQ and ZQ irradiation, respectively. This produces negative NMR signal enhancement for DQ irradiation, and positive NMR signal enhancement for ZQ irradiation.

The SE involves the excitation of forbidden two-spin DQ or ZQ transitions. Narrow-line radicals, where the DQ and ZQ transitions are well separated, and strong microwave irradiation (25–125 mW) are therefore required for efficient polarisation transfer. An ability to modulate the frequency and bandwidth of the MW irradiation can further boost efficiency, reduce build-up times and reduce the required concentration of radical [69].

Following the generation of nuclear spin polarisation in the solid state, the sample is dissolved rapidly by injection of hot solvent and then transported to the NMR spectrometer for detection. The sample can either be transported manually, or under pneumatically-driven flow. The latter automated procedure is beneficial as it reduces transport times and increases repeatability [84]. A key consideration during sample transfer is the loss of polarisation due to relaxation in the liquid state, the rate of which is field-dependent. If the radical is not filtered or neutralised prior to transfer, paramagnetic relaxation of the hyperpolarised nuclei will cause extensive polarisation loss. To limit the effects of paramagnetic relaxation, the sample must not be exposed to very weak magnetic fields or regions of zero field during transport. This can be achieved through the use of a magnetic tunnel that maintains a magnetic field of at least a few millitesla along the entirety of the transfer path [84].

2.2.2. Integration of dDNP with benchtop NMR detection

In principle, the same DNP polariser can be used for dDNP regardless of the NMR spectrometer used for detection. All that is required is a means of transporting the sample to the NMR spectrometer. Therefore, while the instrumentation costs are significant for dDNP, these are centred on the DNP polariser and not the interface with the NMR detector.
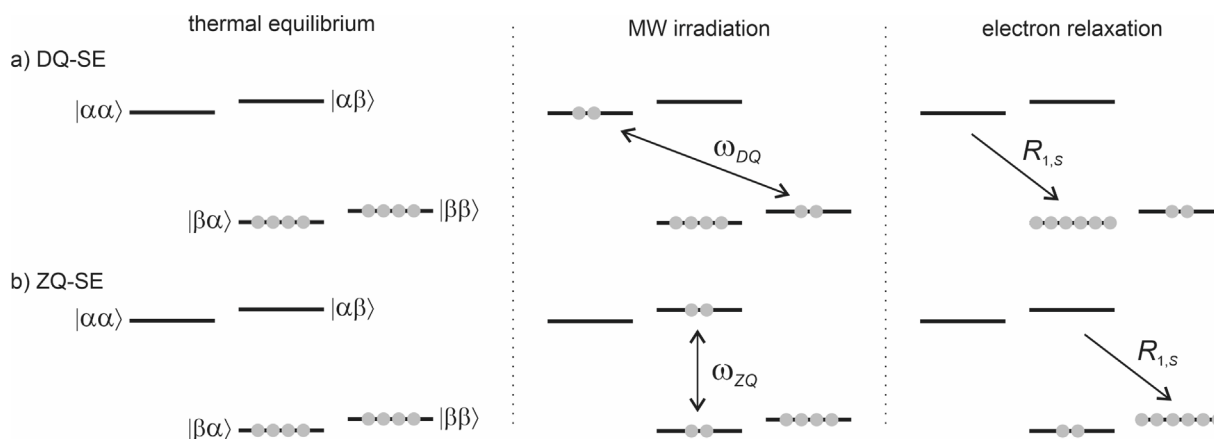
Fig. 7. Schematic representation of polarisation transfer *via* the Solid Effect (SE) using (a) DQ irradiation and (b) ZQ irradiation. The spin system consists of a hyperfine-coupled electron (S) and nucleus (I), where the nucleus has spin $I = \frac{1}{2}$ and a positive gyromagnetic ratio (*e.g.*, ^{1}H or ^{13}C). The kets, $|m_S, m_I\rangle$, describe each state, where α is $m = +\frac{1}{2}$ and β is $m = -\frac{1}{2}$. The electron spin has a negative gyromagnetic ratio and so its lowest energy state is the spin-down ($m_S = -\frac{1}{2}$) state, while for the nucleus it is spin-up ($m_I = +\frac{1}{2}$). Microwave irradiation frequencies are given by $\omega_{DQ} = \omega_S + \omega_I$ and $\omega_{ZQ} = \omega_S - \omega_I$ and $R_{1,S}$ is the rate of electron spin relaxation.

The first use of dDNP with benchtop NMR detection was for reaction monitoring, by Tee and co-workers in 2016 [85]. In this work, hyperpolarised [1-^{13}C]pyruvate was produced by a commercial DNP polariser (SPINlab^{TM} GE) and added to a solution containing lactate dehydrogenase. Here, sample dissolution and transfer to the benchtop NMR spectrometer were achieved in approximately 20 s. During transfer, the sample was exposed to the field of a permanent magnet to minimise paramagnetic relaxation loss. The conversion to [1-^{13}C]lactate was monitored and the associated enzyme kinetics were quantified (Fig. 8). The same chemical transformation was monitored *in vitro* using prostate cancer cells doped with hyperpolarised [1-^{13}C]pyruvate. The authors highlighted several advantages of using benchtop NMR detection instead of a standard high-field NMR spectrometer for this work. Firstly, the increase in hyperpolarisation lifetime in the 1 T field of the benchtop NMR spectrometer facilitates the monitoring of a hyperpolarised metabolite through a multi-enzyme cascade following a single dissolution step. Secondly, the portability and compact size of the benchtop NMR spectrometer allow it to be positioned in close proximity to the DNP polariser, reducing sample transfer times and thus increasing the time period over which reactivity can be monitored. Thirdly, the integration of the perfusion and gaseous exchange platforms that are required to perform live cell studies is arguably easier with a benchtop NMR spectrometer than with a much more expensive and sensitive high-field NMR spectrometer [85].

Another benefit of combining dDNP with a benchtop NMR spectrometer is that they typically operate at clinically relevant magnetic field strengths (*ca.* 1.5 T), enabling direct investigation and optimisation of the behaviour of dDNP-enhanced molecules for clinical imaging applications. Jannin and co-workers have employed 1.9 T benchtop NMR detection to optimise dDNP dissolution and transfer steps for the efficient ^{13}C hyperpolarisation of polymers [86], to extend the hyperpolarisation lifetime of biologically interesting molecules [87], and to propose more efficient ^{1}H to ^{13}C polarisation transfer schemes [68,88]. Similarly, dDNP in combination with benchtop NMR was used recently to optimise ^{15}N hyperpolarisation conditions for [1-^{15}N]nicotinamide-based metabolic imaging tracers in a biocompatible environment [89].

3. *Para*hydrogen-induced polarisation (PHIP)

3.1. Background theory of parahydrogen hyperpolarisation

*Para*hydrogen-induced polarisation (PHIP) was first predicted theoretically and demonstrated experimentally by Bowers and Weitekamp
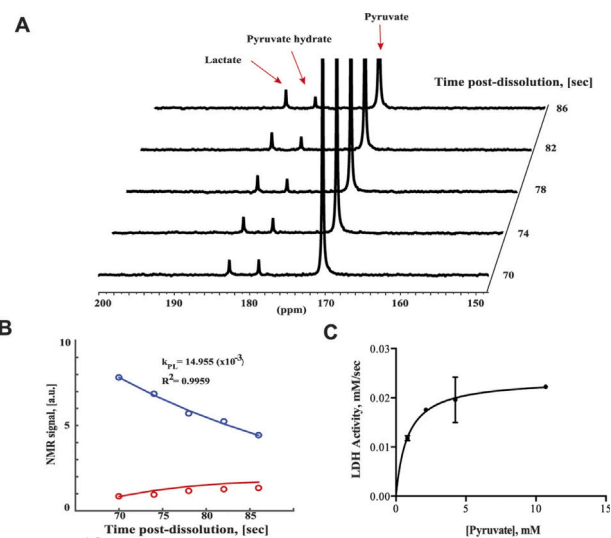
Fig. 8. A) Low-field (1 T) ^{13}C NMR spectra showing the conversion of dDNP-hyperpolarised [1-^{13}C]pyruvate to [1-^{13}C]lactate mediated by lactate dehydrogenase (LDH). B) Data fitted to model to obtain flux rate, k_{PL}. C) Kinetics of LDH obtained by repeating the NMR experiment for different [1-^{13}C]pyruvate concentrations, to obtain a K_m value in agreement with literature values. Reprinted with permission under a CC-BY licence from Ref. [85].

in 1986 and 1987 [90,91], with concurrent, independent observations of the same phenomenon by Eisenberg and co-workers [92,93]. PHIP uses the nuclear singlet isomer of molecular hydrogen, *para*hydrogen (pH_2), as the source of hyperpolarisation. In itself, pH_2 has no net angular momentum ($I_{total} = 0$), and is therefore NMR silent. However, once the symmetry of pH_2 is broken in a chemical reaction, the singlet state can evolve into observable magnetisation such that the pH_2-derived ^{1}H nuclei in the product molecule(s) exhibit highly enhanced NMR signals [94]. The PHIP methodology has been used for mechanistic studies of hydrogenation reactions [95], and has been explored for the production of hyperpolarised contrast agents for *in vivo* MRI [96–102]. In 2009, Duckett and co-workers introduced a non-hydrogenative version of PHIP, signal amplification by reversible exchange (SABRE) [103], whereby a transition metal (typically iridium) complex is used to catalytically transfer nuclear spin order from pH_2 to a target analyte in free solution by means of a reversible exchange reaction. A key advantage of the SABRE approach compared to the original,
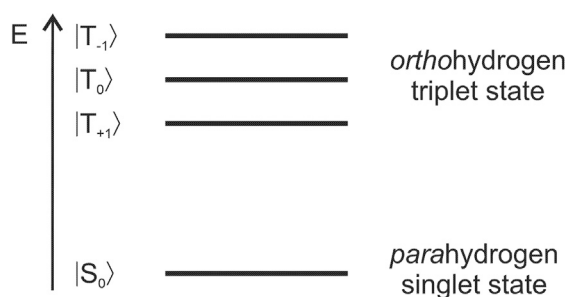
Fig. 9. Schematic energy level diagram for the nuclear spin states of H_2 in the presence of a magnetic field, where $|T_{+1}\rangle$, $|T_0\rangle$ and $|T_{-1}\rangle$ represent the triplet states and $|S_0\rangle$ the singlet state, as defined in Eq. (10). Note: the energy gaps are not drawn to scale.
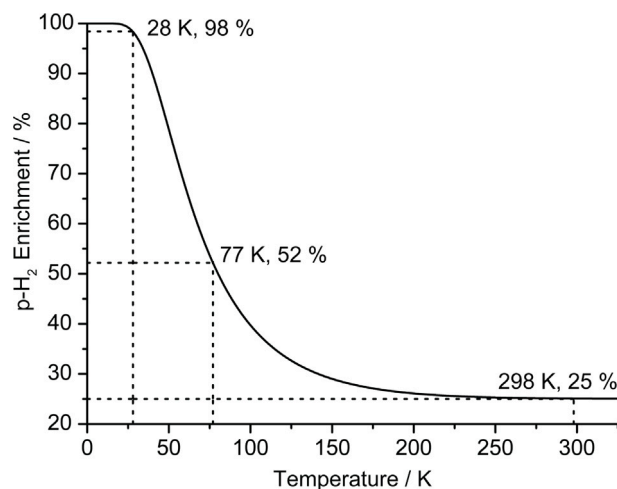

Fig. 10. Theoretical percentage of pH_2 in an equilibrium mixture of oH_2 and pH_2 as a function of temperature for $\theta_R = 87.8$ K.

hydrogenative PHIP method is that the chemical identity of the target analyte is unchanged by the exchange reaction. Consequently, the same sample can be repeatedly repolarised as long as fresh pH_2 is supplied. *Para*hydrogen-based methods do not require a strong magnetic field to achieve high levels of hyperpolarisation. Therefore they are very attractive for use with low-field, portable NMR detectors.

The dihydrogen molecule, H_2, exists in two isomeric forms that differ in their nuclear spin arrangements. These nuclear spin isomers, *ortho*hydrogen (oH_2) and *para*hydrogen (pH_2), arise from the requirement for the total wavefunction of H_2 to be anti-symmetric with respect to particle exchange [104]. The total wavefunction for dihydrogen can be represented as the dot product of the individual wavefunctions for translational (ψ_T), rotational (ψ_R), vibrational (ψ_V), electronic (ψ_E) and nuclear spin (ψ_N) degrees of freedom (Eq. (9)).

$$\Psi = \psi_T \cdot \psi_R \cdot \psi_V \cdot \psi_E \cdot \psi_N \tag{9}$$

ψ_T, ψ_V, and ψ_E are symmetric with respect to particle exchange, so the dot product $\psi_R \cdot \psi_N$ must be anti-symmetric to fulfil Pauli's exclusion principle [105]. Hence, ψ_R and ψ_N are strictly correlated: symmetric rotational states must combine with anti-symmetric nuclear spin states, and *vice versa*.

Dihydrogen possesses two magnetically equivalent $I = \frac{1}{2}$ nuclei that combine to form four nuclear spin states under their mutual scalar coupling (Eq. (10)), where $|\alpha\rangle$ and $|\beta\rangle$ correspond to the $m = +\frac{1}{2}$ and $m = -\frac{1}{2}$ states of the individual nuclei, respectively. Therefore the molecule forms an A_2 spin system according to Pople notation. [106,107]

$$|T_{+1}\rangle = |\alpha\alpha\rangle$$
$$|T_0\rangle = \frac{1}{\sqrt{2}}(|\alpha\beta\rangle + |\beta\alpha\rangle)$$
$$|T_{-1}\rangle = |\beta\beta\rangle \tag{10}$$
$$|S_0\rangle = \frac{1}{\sqrt{2}}(|\alpha\beta\rangle - |\beta\alpha\rangle)$$

$|T_{+1}\rangle$, $|T_0\rangle$ and $|T_{-1}\rangle$ form the symmetric triplet state of oH_2, whilst $|S_0\rangle$ is the antisymmetric singlet state of pH_2. The correlation between ψ_R and ψ_N means that all pH_2 molecules are described by symmetric rotational states ($J = 0, 2, 4, etc.$), whilst oH_2 molecules are described by antisymmetric rotational states ($J = 1, 3, 5, etc.$). The energy difference between the pH_2 singlet state and the oH_2 triplet states is therefore dominated by the difference in energy between the $J = 0$ and $J = 1$ rotational states (Fig. 9).

The absolute populations of pH_2 (N_p) and oH_2 (N_o) as a function of temperature (T) are described by Boltzmann statistics according to Eq. (11), where θ_R is the rotational constant for the molecule.

$$N_p = \sum_{J=even} (2J+1)e^{\frac{-J(J+1)\theta_R}{T}}$$
$$N_o = 3 \sum_{J=odd} (2J+1)e^{\frac{-J(J+1)\theta_R}{T}} \tag{11}$$

The relative proportions of pH_2 and oH_2 in an equilibrium mixture of H_2 gas can then be expressed as fractions, n_p and n_o, respectively (Eq. (12)).

$$n_p = \frac{N_p}{N_p + N_o}$$
$$n_o = 1 - n_p = \frac{N_o}{N_p + N_o} \tag{12}$$

At thermal equilibrium at room temperature there is sufficient thermal energy to populate all four energy states approximately equally, leading to overall populations of $n_p \approx 25$ % and $n_o \approx 75$ %. As T decreases, the proportion of pH_2 (n_p) at thermal equilibrium increases; $n_p \approx 52$ % at 77 K and $n_p > 98$ % at $T < 28$ K (Fig. 10).

Spin isomer interconversion between oH_2 and pH_2 is ordinarily symmetry-forbidden. Simply cooling H_2 is therefore insufficient to rapidly enrich the *para* state. In the presence of an interacting paramagnetic species or suitable surface, the symmetry of the H_2 molecule is broken. Rapid pH_2 enrichment is thus achieved by cooling H_2 in the presence of a spin isomer interconversion catalyst, such as iron(III) oxide [108,109]. Following conversion, the *para*-enriched H_2 gas is separated from the catalyst and returned to room temperature, where it can be stored for weeks to months [110,111]. Whilst in most practical applications health and safety considerations mean that pH_2 is produced in small quantities for immediate use, pH_2 can be enriched and stored for later transport to an off-site location. This has the benefit of removing the need for an on-site pH_2 generator for pH_2-enhanced NMR applications outside of the typical laboratory environment. A range of home-built pH_2 generators are described in the literature, employing either liquid nitrogen ($n_p \approx 52$ %) [108,112–114], or closed-cycle helium cooling ($n_p > 98$ %) [115–117], and commercial pH_2 generators are available. When evaluating a pH_2-based hyperpolarisation method for a potential application, there exists a compromise between the level of pH_2 enrichment required and the size and cost of the instrumentation. Closed-cycle helium cooled systems provide the highest pH_2 enrichment and hence largest signal enhancement (up to 3-fold over liquid nitrogen cooled systems) [118], but require more sophisticated equipment, which is both costly to procure and requires routine maintenance.

3.1.1. Hydrogenative parahydrogen induced polarisation (PHIP)

In the first PHIP experiments, the requirement to break the symmetry of the two protons in pH_2 was achieved through the hydrogenation
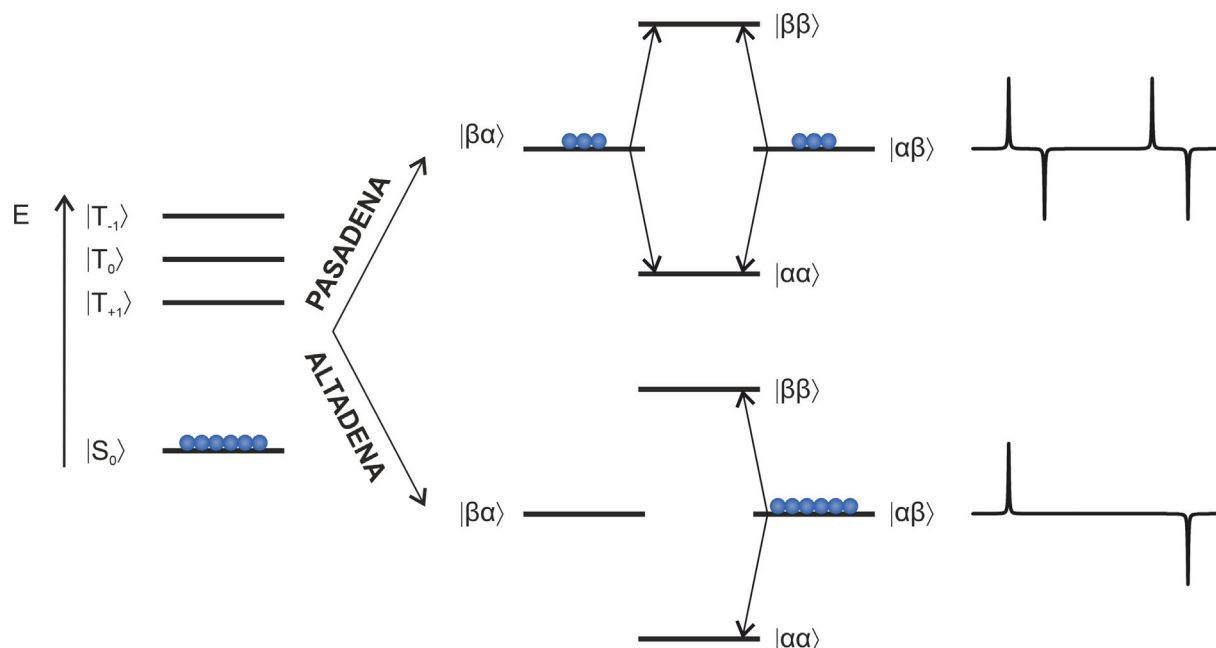
Fig. 11. Schematic of the effect of incorporation of $p\mathrm{H}_2$ into an unsaturated molecule *via* hydrogenation under (top) PASADENA (high-field, weak coupling) and (bottom) ALTADENA (low-field, strong coupling) conditions. Under PASADENA conditions, the $p\mathrm{H}_2$-derived protons are transformed into an AX spin system, where the population of the $|S_0\rangle$ starting state is divided equally between near-degenerate $|\alpha\beta\rangle$ and $|\beta\alpha\rangle$ product states. This produces a spectrum with an enhanced pair of anti-phase doublets. Conversely under ALTADENA conditions, the $p\mathrm{H}_2$-derived protons are transformed into an AB spin system during polarisation transfer, where the population of the $|S_0\rangle$ starting state is channelled into a superposition of the $|\alpha\beta\rangle$ and $|\beta\alpha\rangle$ product states. Following adiabatic transfer into the NMR spectrometer for detection, this leads to overpopulation of either the $|\alpha\beta\rangle$ or $|\beta\alpha\rangle$ product states, giving rise to an NMR spectrum with preferential enhancement of one half of each doublet.

of an unsaturated molecule [91,92,119]. The form of the enhanced NMR signals that are observed following hydrogenation depends on the strength of the magnetic field in which the reaction occurs and the features of the spin system that contains the $p\mathrm{H}_2$-derived protons in the product. In the following description, we assume that the $p\mathrm{H}_2$-derived protons in the product are chemically inequivalent, with Larmor frequencies ν_1 and ν_2 ($\nu_1 \neq \nu_2$) and a mutual scalar coupling constant of $J_{1,2}$.

Under PASADENA (*para*hydrogen and synthesis allow dramatically enhanced nuclear alignment) conditions, hydrogenation takes place in a strong magnetic field, typically inside the NMR spectrometer [91]. In this high-field regime, the difference in chemical shift between the $p\mathrm{H}_2$-derived protons is much larger than their mutual scalar coupling ($|\nu_1 - \nu_2| \gg J_{1,2}$), and so they may be described as a weakly coupled AX spin system. Here, the $|\alpha\beta\rangle$ and $|\beta\alpha\rangle$ states are nearly degenerate, such that the initial overpopulation of the $|S_0\rangle$ state of $p\mathrm{H}_2$ is distributed approximately equally between the two. The four allowed transitions from these states (all to $|\alpha\alpha\rangle$ or $|\beta\beta\rangle$) produce a characteristic anti-phase doublet for each proton (Fig. 11, top).

Conversely, under ALTADENA (adiabatic longitudinal transport after dissociation engenders net alignment) conditions, the hydrogenation reaction is performed in a weak magnetic field before the sample is transported to the NMR spectrometer for detection [119]. In this low-field regime, the chemical shift difference between the $p\mathrm{H}_2$-derived protons in the product is comparable in magnitude to their mutual scalar coupling ($|\nu_1 - \nu_2| \approx J_{1,2}$), and so they form a strongly coupled AB spin system. Therefore, it is a superposition of the $|\alpha\beta\rangle$ and $|\beta\alpha\rangle$ states that is preferentially overpopulated from the $|S_0\rangle$ starting state. Following adiabatic transfer of the sample into the high field of the NMR spectrometer, the spins are transformed into a weakly coupled AX spin system that exhibits a preferential overpopulation of either the $|\alpha\beta\rangle$ or $|\beta\alpha\rangle$ state. This is illustrated schematically in Fig. 11 for the case where $|\alpha\beta\rangle$ is overpopulated. The NMR spectrum thus takes the form of preferential enhancement of one half of an anti-phase doublet for each proton, each with opposing phase (Fig. 11, bottom). Which of the $|\alpha\beta\rangle$ or $|\beta\alpha\rangle$ states is favoured depends on the details of the spin

system and the effects of NMR relaxation between polarisation transfer in the low-field regime and NMR detection at high field.

Hydrogenative PHIP is an excellent tool for NMR based mechanistic studies of hydrogenation reactions, because not only does it enhance the signals of the product molecules, it can also enhance otherwise unobserved low-concentration intermediates that break the symmetry of the $p\mathrm{H}_2$-derived protons on a suitable timescale [95]. It has also been explored for the production of hyperpolarised contrast agents for *in vivo* magnetic resonance imaging [96–102]. For broader analytical applications, however, the limited substrate scope of hydrogenative PHIP is a significant drawback. This is because the technique requires a starting material that can accept a hydrogen molecule, typically those which contain unsaturated moieties. An increase in the scope of analytes is afforded by the "PHIP by sidearm hydrogenation" (PHIP-SAH) method [98], in which a precursor to the target molecule containing an unsaturated sidearm is first hydrogenated. Polarisation is then transferred from the sidearm to nuclei on the target molecule, by either field cycling in ALTADENA-type experiments [120], or radiofrequency (RF)-driven transfer in PASADENA-type experiments [121,122]. In both cases, it is beneficial to transfer polarisation to $^{13}\mathrm{C}$ nuclei to take advantage of their slower longitudinal (T_1) relaxation, and hence longer hyperpolarisation lifetimes. Finally, rapid cleavage of the sidearm provides the hyperpolarised target analyte. PHIP-SAH has shown promise for the development of hyperpolarised MRI contrast agents [123]. However, the need to synthesise a suitable precursor and the irreversibility of the hydrogenation reaction impose significant limitations on its use in analytical applications.

The recent chemical-exchange-based hydrogenative PHIP method, known alternatively as PHIP-X [124], or PHIP-Relay [125], overcomes the limitations of traditional PHIP and extends its applicability to a broad range of substrates containing exchangeable protons. This method, shown schematically in Fig. 12, is analogous to the earlier SABRE-Relay approach (described in Section 3.1.2) [126]. In the following discussion we will use the term PHIP-Relay as this maintains a clear link with the associated SABRE-Relay method, and avoids
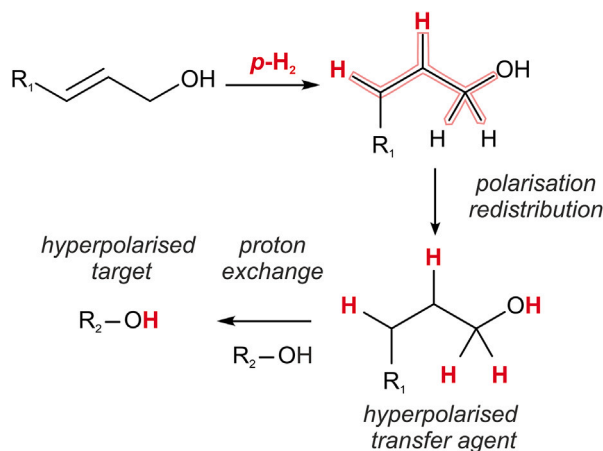
Fig. 12. Schematic representation of the PHIP-Relay hyperpolarisation process. A relay molecule is first hyperpolarised using standard hydrogenative PHIP approaches. Following polarisation redistribution within the relay molecule, hyperpolarisation is transferred to the target analyte *via* proton exchange.

Fig. 13. Schematic representation of the SABRE hyperpolarisation process. One molecule of *para*hydrogen and three molecules of substrate, here 3,5-difluoropyridine, bind reversibly to an iridium complex containing a stabilising ligand (IMes). Polarisation is transferred from the pH_2-derived hydrides to the substrate through the network of scalar couplings in this transient iridium complex.

potential confusion with the use of "X" to denote polarisation transfer to heteronuclei.

In the PHIP-Relay approach, pH_2 is first incorporated (under either PASADENA or ALTADENA conditions) into an unsaturated molecule, the hyperpolarisation transfer agent, which contains an exchangeable proton group (*e.g.*, an alcohol). The hyperpolarisation is then distributed throughout the transfer agent, such that its exchangeable proton becomes hyperpolarised. The target molecule, which need only contain an exchangeable proton and not an unsaturated moiety, becomes hyperpolarised upon proton exchange with the transfer agent. As in other PHIP experiments, the hyperpolarisation can then be redistributed within the target molecule, including to heteronuclei such as ^{13}C and ^{15}N, *via* spontaneous or RF-driven polarisation transfer [125]. At first glance, PHIP-Relay appears to be a single-shot method, as the initial hydrogenation of the relay molecule is irreversible. However, if the rate of this reaction is slow compared to the rate of proton exchange, multiple hyperpolarisation experiments can be performed using the same sample because the polarisation transfer step is fully reversible. Therefore, as long as the starting material remains in the sample in excess, the same target analyte can be re-polarised multiple times *via* the exchange mechanism. The PHIP-Relay method has been successfully used to hyperpolarise ^1H in water and alcohols up to $P \approx$ 1 % [124], as well as ^{13}C and ^{15}N for a range of metabolites at natural isotopic abundance, including urea and glucose [125].

3.1.2. Signal amplification by reversible exchange (SABRE)

Introduced in 2009, the signal amplification by reversible exchange (SABRE) method addresses key limitations of hydrogenative PHIP approaches; specifically, the need for a suitable unsaturated precursor and the irreversibility of the hydrogenation reaction [103]. In SABRE, one pH_2 molecule and one or more molecules of the target analyte reversibly bind to a polarisation transfer catalyst (Fig. 13), typically an octahedral organoiridium complex of the form $[Ir(H)_2(NHC)(substrate)_3]^+$, where NHC represents a stabilising nitrogen-containing heterocyclic carbene such as 1,3-bis(2,4,6-trimethylphenyl)-1,3-dihydro-2*H*-imidazol-2-ylidene (IMes) [127]. Within this transient complex, a network of scalar couplings exists between the pH_2-derived hydrides and NMR-active nuclei in the substrate, providing a conduit for polarisation transfer to the target molecule.

Formation of the SABRE-active catalyst is achieved through hydrogenation of a stable pre-catalyst in the presence of an excess of substrate (*i.e.*, the molecule to be hyperpolarised). It is then the substrate molecules bound *trans* to the hydrides that dissociate to facilitate
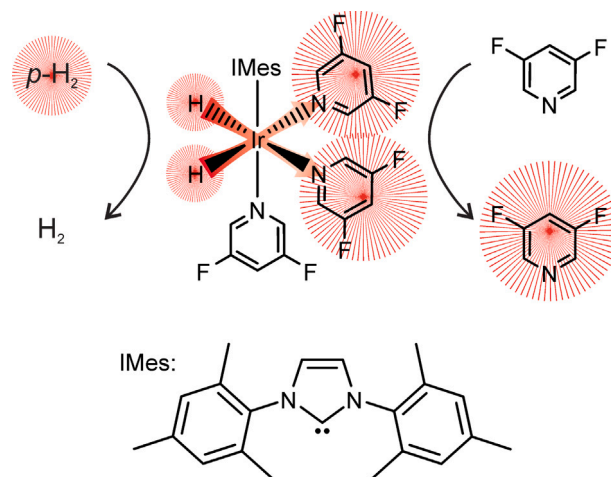
both pH_2 and substrate exchange. As both dihydrogen and the substrate exchange reversibly with an excess in solution, the source of polarisation, pH_2, is continuously refreshed and is able to hyperpolarise new units of substrate. The exchange process promotes a build up of hyperpolarised substrate in free solution, which can provide very high levels of spin polarisation ($P > 50 \%$) [128].

Unlike in hydrogenative PHIP, SABRE does not require the incorporation of the protons from pH_2 into the target analyte. The target therefore remains chemically unchanged, and can be re-polarised as long as fresh pH_2 is supplied [129]. In principle, SABRE can be applied to any molecule that can bind reversibly to the SABRE catalyst on a suitable timescale. The classic example of an efficient SABRE substrate is pyridine, which was used in the first demonstrations of this method [103]. The SABRE activity of pyridine, along with many other nitrogen-containing heterocycles, has been studied extensively in the literature [103,130–138]. SABRE has also been demonstrated for a range of other analytes, including nitriles [139–141], Schiff bases [142], nitrites [143], amino acids and oligopeptides [144–146], thiophenes [147], and phosphines [148]. A comprehensive list of molecules enhanced by SABRE, up to 2019, is available in the review by Barskiy and co-workers [149].

Polarisation transfer in SABRE is mediated by strong coupling between the pH_2-derived hydrides and nuclei in the substrate in the low-field regime [150,151]. It is therefore similar to the ALTADENA experiment (Section 3.1.1). An important difference is that the pH_2-derived hyperpolarisation is transferred *via* the transient scalar coupling network of the polarisation transfer catalyst. The mechanism of transfer is most easily understood through the concept of level anti-crossings (LACs). In the following we provide a brief summary of how LACs can be used to understand polarisation transfer in SABRE. For a more comprehensive theoretical treatment, we refer interested readers to previous review articles on this topic [149,152].

A LAC occurs when two eigenstates approach the same energy, but do not cross due to the presence of a perturbation that lifts the degeneracy between the two states. The role of LACs in the active SABRE catalyst can be understood by considering an AA'B three-spin system, formed by the pH_2-derived hydrides (AA') and a spin-1/2 nucleus (B) on the substrate (Fig. 14). In this system, the hydrides are chemically equivalent ($\nu_A = \nu_{A'}$) but couple differently to the substrate nucleus, $J_{AB} - J_{A'B} \neq 0$, which resonates at different frequency, ν_B. Following the formalism of Ivanov et al. [152], we define a zero-order Hamiltonian, $\hat{H}_0$, that contains the nuclear Zeeman interactions of all
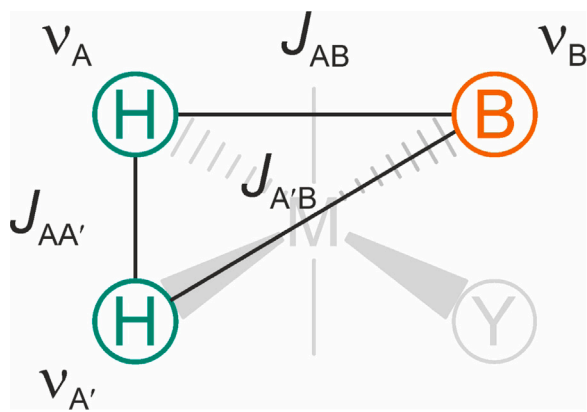
Fig. 14. Schematic of an AA'B system. Spins A and A' represent the hydride nuclei in the active SABRE catalyst. These are chemically equivalent ($\nu_A = \nu_{A'}$), but their magnetic equivalence is broken by the difference in their scalar coupling ($J_{AB} \neq J_{A'B}$) to substrate nucleus B, with Larmor frequency, ν_B.

Fig. 15. Energy levels of the $+\frac{1}{2}$ manifold of an AA'B spin system as a function of magnetic field with (a) $J_{AB} = J_{A'B} = 0$ and (b) $J_{A'B} = 1$ Hz ($J_{AB} = 0$). The energies were calculated for $\delta_A = \delta_{A'} = -23$ ppm, $\delta_B = 8$ ppm and $J_{AA'} = -8.5$ Hz. The calculations were carried out in the rotating frame with the centre frequency set to -12.5 ppm. The energy levels are labelled according to the eigenstates of the zero-order nuclear spin Hamiltonian, $\hat{H}_0$. The circle highlights the location of the LAC in (b).

spins with the magnetic field, B_0, and the scalar coupling between the hydrides, $J_{AA'}$. The perturbation Hamiltonian, $\hat{H}_1$, contains the scalar coupling between the hydrides and the substrate nucleus (J_{AB} and $J_{A'B}$). This formulation assumes that the coupling interactions in $\hat{H}_1$ are much smaller than the interactions in $\hat{H}_0$.

We can describe the energy levels for this AA'B spin system using the singlet–triplet basis ($|S_0\rangle, |T_{+1}\rangle, |T_0\rangle, |T_{-1}\rangle$) for the hydride spins (AA') and $|\alpha\rangle$ and $|\beta\rangle$ for the substrate spin, B. This three-spin system can be divided into four manifolds based on the z-projection of the total angular momentum, **F**, which can take values of $m_F = \pm\frac{3}{2}$ and $m_F = \pm\frac{1}{2}$. The states in each of the four manifolds are given in Eq. (13).

$$
\begin{aligned}
m_F = +\tfrac{3}{2} &\quad |T_{+1}\alpha\rangle \\
m_F = +\tfrac{1}{2} &\quad |T_{+1}\beta\rangle;\ |T_0\alpha\rangle;\ |S_0\alpha\rangle \\
m_F = -\tfrac{1}{2} &\quad |T_{-1}\alpha\rangle;\ |T_0\beta\rangle;\ |S_0\beta\rangle \\
m_F = -\tfrac{3}{2} &\quad |T_{-1}\beta\rangle
\end{aligned}
\tag{13}
$$

LACs can occur within the three states of the $\pm\frac{1}{2}$ manifolds, with both manifolds exhibiting a LAC in the region of $B_0 = 0$ [152]. Of significant interest to the SABRE case is the additional LAC in a non-zero field that occurs in one of these manifolds. Which manifold contains the LAC depends on the relative signs of the scalar couplings. Here we will consider the case where this is the $+\frac{1}{2}$ manifold. The energies of the three states in this manifold are shown as a function of magnetic field in Fig. 15. In the absence of coupling between the hydrides and the substrate nucleus (Fig. 15a, $J_{AB} = J_{A'B} = 0$) there is a crossing between the $|T_{+1}\beta\rangle$ and $|S_0\alpha\rangle$ states near 6 mT. In the presence of a coupling of $J_{A'B} = 1$ Hz (Fig. 15b), the perturbation Hamiltonian, $\hat{H}_1$, removes the degeneracy of the states, causing the crossing to be avoided. Importantly, in the region of the LAC, the states are mixed, allowing for efficient population transfer.

When a fresh molecule of pH_2 adds to the SABRE catalyst, the $|S_0\alpha\rangle$ and $|S_0\beta\rangle$ states are overpopulated relative to the other states in the spin system, due to the pure initial singlet state of pH_2. Immediately following binding, no hyperpolarisation is observed because the hydrides are in an NMR-silent singlet state and the $|\alpha\rangle$ and $|\beta\rangle$ states of the substrate spin are roughly equally populated (thermal equilibrium polarisation). However, if the sample is exposed to the magnetic field at which a LAC occurs within the $+\frac{1}{2}$ manifold, the $|S_0\alpha\rangle$ state will be mixed with the $|T_{+1}\beta\rangle$ state, as shown in Fig. 15b, allowing for efficient population transfer on a timescale corresponding to the inverse of the hydride–substrate coupling. This leads to a significant over-population of the $|\beta\rangle$ spin state of the substrate nucleus, giving rise to a strong
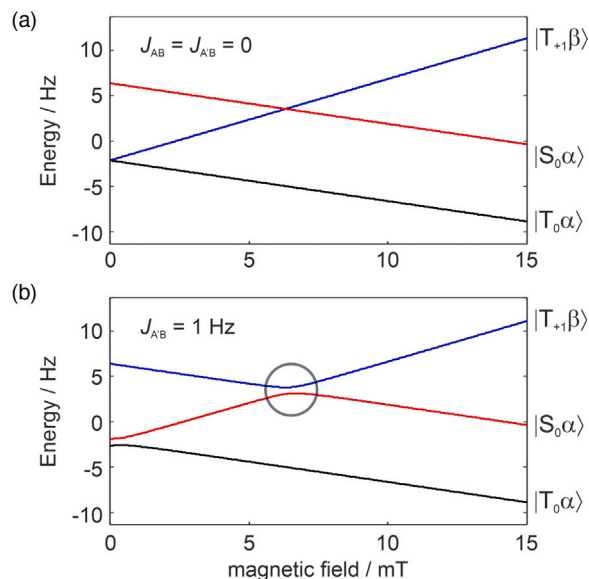
emission signal in an NMR spectrum. Achieving optimal polarisation transfer in SABRE, therefore, requires knowledge of the magnetic field at which a LAC occurs.

A LAC is observed when the difference in Larmor frequency between the pH_2-derived hydrides and the nucleus in the substrate is matched to the effective scalar coupling (J_{eff}) of the system [153]. Under typical conditions, $|J_{AA'}|$ is considerably larger than $|J_{AB}|$ and $|J_{A'B}|$, making it approximately equal to the effective scalar coupling of this system (Eq. (14)) [149].

$$
\Delta\nu = J_{eff} \approx J_{AA'}
\tag{14}
$$

The scalar coupling values remain unchanged at different magnetic fields. Therefore the difference in Larmor frequency, $\Delta\nu$, can be adjusted to meet the LAC condition (Eq. (14)) by applying an appropriate magnetic field, commonly known as the polarisation transfer field (B_{PTF}). For transfer to ^{1}H nuclei, the appropriate B_{PTF} is given by Eq. (15), where the difference in Larmor frequency between the hydrides (AA') and nucleus (B) is determined by the difference in chemical shift, $\Delta\delta$.

$$
B_{PTF} = 2\pi \frac{J_{AA'}}{\gamma_{^1H}\Delta\delta}
\tag{15}
$$

Using the most common Ir-based SABRE catalyst (Fig. 13) with pyridine or a pyridine derivative as the substrate, the chemical shift difference between the hydride signals (-23 ppm) and the substrate nuclei ($7 - 8$ ppm) is typically matched to the effective scalar coupling, $|J_{AA'}| \approx 6 - 10$ Hz, in a polarisation transfer field $B_{PTF} \approx 6.5$ mT. In practice, the spin system of the active catalyst is far more complex than the AA'B system described here. However, it has been found experimentally that Eq. (15) provides a good estimate of the optimal value for B_{PTF} and that the resonance condition is generally quite broad, with significant enhancements observed over a range of several mT [137,152,154].

Other heteronuclei in the substrate molecule (*e.g.*, ^{13}C, ^{15}N, etc.) can also be enhanced using what is commonly known as SABRE-SHEATH (SHield Enables Alignment Transfer to Heteronuclei) [130]. The optimum field for polarisation transfer in this case (Eq. (16)) is considerably lower (nT to µT), as the difference in Larmor frequency between the hydrides and the target nucleus is dominated by the

difference in gyromagnetic ratio between the protons, γ_H, and the heteronucleus, γ_X (Eq. (16)). Through this approach, hyperpolarisation of a wide range of nuclei including ^{13}C, ^{15}N, ^{19}F and ^{31}P has been reported [130,136,148,155–158].

$$B_{PTF} = 2\pi \frac{J_{AA'}}{\gamma_{1H}(1 - \delta_{1H}) - \gamma_X(1 - \delta_X)} \qquad (16)$$

We note that in the case of ^{15}N, where the target nucleus is directly bound to the Ir catalyst (*e.g.*, in ^{15}N-pyridine), the hydride–substrate coupling (*e.g.*, $J_{A'B} \approx 25$ Hz) is larger than the hydride–hydride coupling, $J_{AA'}$. This violates the assumptions underpinning the perturbation treatment used above to define the position of the LAC, so Eq. (16) does not apply. Highly efficient strategies for SABRE polarisation transfer in this case have been developed by Warren and co-workers, based on novel numerical simulation approaches for chemically exchanging systems and field modulation in the μT regime [159,160].

In the majority of SABRE experiments, hyperpolarisation is built up in solution at B_{PTF} over a period of seconds, before the sample is transported into the NMR spectrometer for detection. Alternatively, polarisation can be transferred directly inside the magnetic field of the NMR spectrometer. High-field polarisation transfer strategies rely on LAC conditions being met under continuous wave RF irradiation [161–164], or coherent transfer techniques using INEPT-like pulse sequences [165]. Details of the theory behind the different polarisation transfer approaches in SABRE can be found in the review article of Barskiy et al. [149]

The level of signal enhancement that can be achieved *via* SABRE is system-specific, but can be optimised by careful selection of experimental conditions. One of the key factors controlling SABRE efficiency is the residence time of the target molecule on the iridium complex [166]. This period of time should be long enough for the polarisation to be transferred onto the analyte, but not so long that it promotes the relaxation of the hyperpolarised signal. It has been proposed that the optimal substrate dissociation rate for ^1H hyperpolarisation is around 4.5 s^{-1} [166,167]. The substrate dissociation rate is controlled by the identity of the target substrate [166], the steric bulk and electron-donating properties of the catalyst-bound co-ligand and NHC [127, 128], as well as the temperature at which the reaction is performed [166]. One strategy used to optimise the efficiency of the SABRE process is to selectively deuterate the NHC on the catalyst. This acts to increase the nuclear spin relaxation times of the nuclei on the substrate bound to the catalyst, as well as to reduce the number of nuclei amongst which the polarisation is shared [128]. Under optimised conditions, ^1H polarisation levels of 63% have been reported [128]. By understanding the role of such variables on the maximum polarisation levels, it is possible to tailor the SABRE experiment to optimise signal enhancement for the target analyte.

One limitation on the range of analytes whose NMR signals can be efficiently enhanced by SABRE is the need for three molecules of the substrate to bind to form the active SABRE catalyst (Fig. 13). This form of the active catalyst is not suitable for substrates that are sterically hindered, or those which prefer a bidentate binding mode [168–170]. In addition, for weakly binding substrates, multiple catalyst species are often observed in solution, including solvent adducts [171]. The presence of multiple catalyst species leads to more complex kinetics in solution and may limit hyperpolarisation efficiency. These challenges can be overcome through the introduction of one or more co-substrates into solution to promote the formation and stabilisation of a suitable active polarisation transfer catalyst [170]. This co-substrate approach has been used to hyperpolarise the metabolite pyruvate, which adopts a bidentate binding mode in the presence of the co-substrate DMSO and the standard SABRE pre-catalyst [172]. Further optimisation of this pyruvate and DMSO system has led to the first demonstration of *in vivo* MRI using a SABRE-hyperpolarised contrast agent [173]. In the context of analytical applications, a further significant benefit of the co-substrate approach in SABRE is that it provides a route to
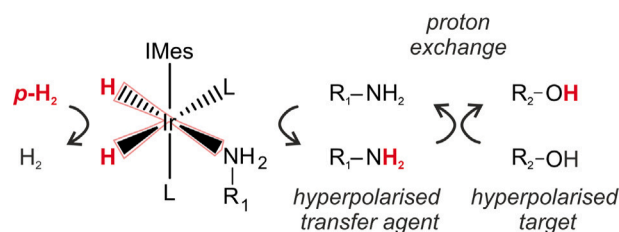

Fig. 16. Schematic representation of the SABRE-Relay hyperpolarisation process. The polarisation transfer agent (typically an amine) is first hyperpolarised through reversible binding to the SABRE catalyst. Following dissociation, hyperpolarisation is transferred to the target analyte *via* proton exchange in solution.

quantification. Tessari and co-workers have demonstrated that when a target analyte is present in sub-stoichiometric amounts relative to an active catalyst species stabilised by one or more co-substrates, a linear SABRE hyperpolarisation response is observed as a function of the target analyte concentration [174]. Under these conditions, nicotinamide and other pyridine-based substrates were quantified at low micromolar concentrations within a complex mixture using high-field (14 T, 600 MHz) NMR detection [175].

A further limit on the range of analytes amenable to SABRE hyperpolarisation is the need for the target substrate to bind reversibly to the active SABRE catalyst on a suitable timescale. This challenge can be overcome using the SABRE-Relay method illustrated in Fig. 16 [126, 176]. In SABRE-Relay, a polarisation transfer agent that contains exchangeable protons (typically an amine) is first hyperpolarised through reversible binding to the SABRE catalyst. In the second step, the target analyte in solution is hyperpolarised *via* proton exchange with the polarisation transfer agent. In this way, hyperpolarisation is achieved for analytes that do not bind to the SABRE catalyst. In principle, the SABRE-Relay approach extends the applicability of SABRE to any chemical species that contains exchangeable protons, including but not limited to alcohols, carboxylic acids, phosphates and carbonates [126].

3.2. Integration of pH$_2$ hyperpolarisation with benchtop NMR detection

A simple way to integrate *para*hydrogen hyperpolarisation with benchtop NMR detection is to carry out the reaction within a sealed NMR tube fitted with a J Young valve. In this approach, pH_2 is added to the headspace of the tube and mixed into solution by vigorous shaking for several seconds. The sample is then inserted into the benchtop NMR spectrometer for signal detection. Whilst in hydrogenative PHIP experiments the strength of the magnetic field in which hydrogenation occurs affects only the form of the hyperpolarised NMR spectrum (and not the efficiency of polarisation transfer), to optimise the build-up of hyperpolarisation in SABRE experiments the sample must be exposed to a particular B_{PTF} during shaking. As the strength of this field is weak ($B_{PTF} < 10$ mT) and need not be particularly homogeneous, a simple handheld permanent magnet array [177], or a solenoid electromagnet [178] can be used. To enable direct SABRE transfer to low gyromagnetic ratio heteronuclei, a μ-metal shield can be employed to exclude the Earth's magnetic field and achieve polarisation transfer fields in the nT to μT range [130,136,148,155–158]. Early demonstrations of SABRE-enhanced benchtop NMR spectroscopy employed this manual "shake-and-drop" approach [156,177,179]. ^1H NMR signal enhancements of up to 17000-fold were observed for pyridine with detection at 1 T, with comparable polarisation levels observed for benchtop and high-field NMR detection (Fig. 17) [156]. In addition, INEPT polarisation transfer has been used to obtain ^{13}C NMR signal enhancements up to 45500-fold for samples at natural isotopic abundance [156]. Hyperpolarised ^{13}C benchtop NMR spectra of glucose have also been obtained using SABRE-Relay and the manual shake-and-drop approach [180].
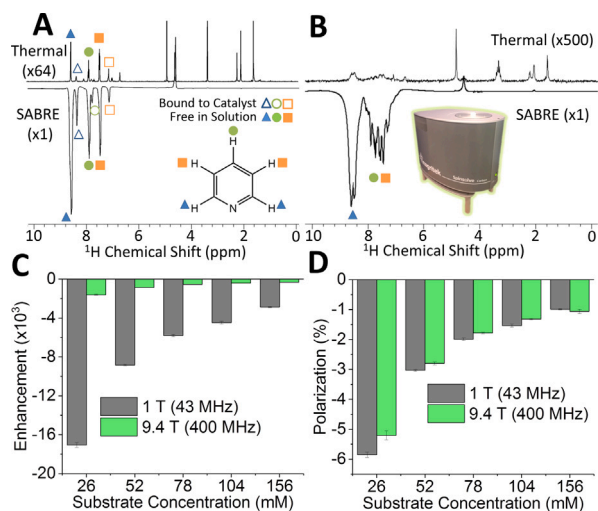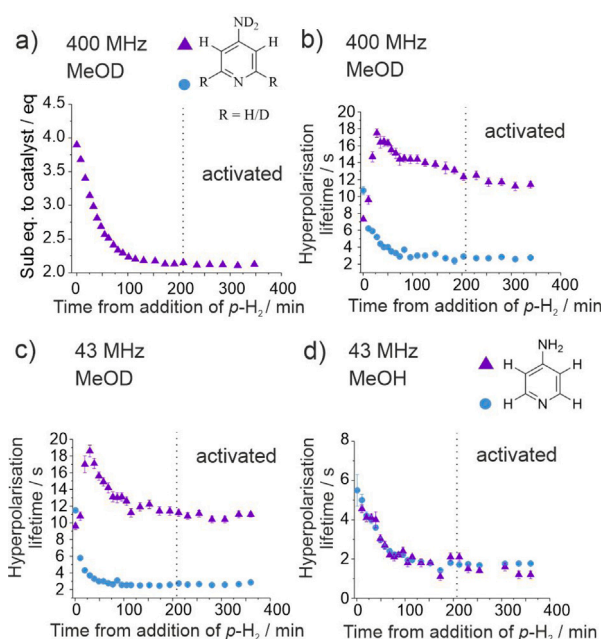
Fig. 17. Comparison of thermally polarised (top) and SABRE-enhanced (bottom) ^{1}H NMR spectra of pyridine at (a) 400 MHz and (b) 43 MHz. Comparison of (c) SABRE enhancement factor and (d) SABRE polarisation level as a function of pyridine concentration for samples containing 5 mM of the SABRE catalyst in methanol-d_4 at 400 MHz (green) and 43 MHz (grey). Reprinted with permission under a CC-BY licence from Ref. [156].

Fig. 18. (a) Reduction in ^{1}H NMR signal of free 4-aminopyridine as a function of time since the first addition of pH$_2$, due to the consumption of 4-aminopyridine during SABRE catalyst activation in methanol-d_4. (b, c) Single-shot hyperpolarisation lifetime measurements for the two proton resonances of 4-aminopyridine as a function of time after the first addition of pH$_2$, with detection at (b) 400 MHz and (c) 43 MHz. The initial increase in the hyperpolarisation lifetime of the *meta* resonance (purple triangles) is due to deuteration of the *ortho* position of 4-aminopyridine (blue circles), while the overall reduction in lifetime is due to catalyst activation. (d) Repetition of the same experiment as (c) in protiomethanol showing the effect of catalyst activation on hyperpolarisation lifetime in the absence of hydrogen isotope exchange. Reprinted with permission under a CC-BY licence from Ref. [183].

The shake-and-drop SABRE approach with benchtop NMR detection has been explored for forensic applications, such as the detection of drug adulteration. Specifically, it has been used to hyperpolarise piperazine-based drugs in a simulated tablet [181], as well as mirfentanil in heroin at concentrations below 1% w/w [182]. In forensic applications, the ability to transport the benchtop NMR detector to the point-of-need is particularly advantageous.

A further application of *para*hydrogen-enhanced benchtop NMR spectroscopy is that to reaction monitoring. In 2019, Semenova et al. used shake-and-drop SABRE experiments to investigate the reactivity of the SABRE catalyst. Single-shot measurements of hyperpolarisation lifetime were used to simultaneously follow activation of the SABRE catalyst and the effects of substrate hydrogen isotope exchange [183], with comparable results obtained for both high-field (400 MHz) and benchtop (43 MHz) NMR detection (Fig. 18). The comparatively weaker solvent response of the benchtop NMR spectrometer enabled the use of protio solvents (Fig. 18d). By removing the source of deuterium, benchtop NMR experiments were able to isolate the effects of catalyst activation on hyperpolarisation lifetime measurements from that of hydrogen isotope exchange.

Similarly, the hydrogenative PHIP response has been used for quantitative monitoring of the oxidative addition of pH$_2$ to Vaska's complex (as well as to associated derivatives) in both single- and multiple-component systems [184]. Here, the reduced background signal of the benchtop NMR spectrometer presents an advantage over comparable hyperpolarised high field NMR measurements. At high field, as the reaction proceeds, the thermally polarised signal from the product increases, interfering with the hyperpolarised response and complicating the kinetic analysis. Spectral editing methods are typically used to differentiate between hyperpolarised and non-hyperpolarised signals to simplify the analysis. However, this comes with a sensitivity penalty. On a benchtop NMR spectrometer, no non-hyperpolarised signals are observed for the product, allowing for a simple and efficient pulse-acquire experiment to be used for the detection of the hyperpolarised signals.

Whilst the manual pH$_2$ hyperpolarisation approach benefits from simplicity, repeat sample shaking is impractical and suffers from poor reproducibility and repeatability. Instead, many pH$_2$ hyperpolarisation experiments are performed by bubbling pH$_2$ through a capillary into solution, with an electromagnet used to generate B_{PTF} where required,

followed by manual transport of the sample to the benchtop NMR spectrometer for detection. The use of microcontroller-driven solenoid valves provides precise control of pH$_2$ delivery, which can be interfaced with the spectrometer control software to enable synchronisation within an NMR pulse sequence. This semi-automated approach has been widely used within the hyperpolarisation community to develop new pH$_2$-based hyperpolarisation methods [124,185–188], to optimise signal enhancement for target molecules of analytical interest [189–191], and for the development of hyperpolarised contrast agents for *in vivo* MRI [141,192–195]. Jeong and co-workers have also used this approach to monitor an esterification reaction [196]. Here, pH$_2$ was bubbled through the reaction mixture in an NMR tube in a B_{PTF} of 7 mT. The reaction was successfully monitored using the SABRE-hyperpolarised signals of the product following manual transfer of the sample into the benchtop NMR spectrometer at 1 min intervals over a period of 30 min. This approach was also used to provide mechanistic insight into a copper-catalysed azide-alkyne click reaction through SABRE-derived signal enhancement of low-concentration intermediates over a period of 120 min [197].

Further improvement in repeatability is obtained by automating the entire hyperpolarisation process (*i.e.*, sample transfer as well as pH$_2$ delivery). Fully automated SABRE hyperpolarisation was first integrated with benchtop NMR detection in 2018 [156,177,198], by adapting a stopped-flow system originally designed for high-field NMR detection [199,200]. As in the semi-automated approach, pH$_2$ is first bubbled through the sample in a reaction cell held inside an electromagnet at B_{PTF}. Following the build-up of hyperpolarisation, the sample is pneumatically transferred (under nitrogen gas pressure) into the benchtop NMR spectrometer for detection. The high repeatability of fully automated pH$_2$-hyperpolarisation was found to enable its application to a variety of multi-step NMR experiments, including 2D NMR

experiments such as ^1H-^1H homonuclear and ^1H-^{13}C heteronuclear correlation spectroscopy [156,198].

Continuous-flow approaches to pH$_2$ hyperpolarisation have also been demonstrated, by using a peristaltic pump to flow the sample between the reaction chamber and the benchtop NMR spectrometer [201–203]. Jeong and co-workers used continuous-flow PHIP to monitor the Wilkinson's catalyst-mediated hydrogenation of styrene over a period of 20 min, by bubbling pH$_2$ through an *ex situ* reaction vessel and continuously flowing a small proportion of the reaction mixture through the benchtop NMR spectrometer for detection [201]. Similarly, Golowicz et al. used a continuous-flow apparatus to follow the simultaneous hydrogenation of ethyl phenylpropiolate and ethyl 2-butynoate with time-resolved non-uniformly sampled (TR-NUS) 2D benchtop NMR experiments [202]. Lehmkuhl and co-workers have also integrated continuous-flow SABRE hyperpolarisation with benchtop NMR detection, by employing a semi-permeable membrane through which pH$_2$ effuses into circulating solution [204]. Further development of this approach by TomHon et al. produced a tube-in-tube spin transfer automated reactor [203]. The higher interfacial area between pH$_2$ and solution with a tubular membrane was found to provide more efficient pH$_2$ mass transfer and reduced solvent evaporation compared to bubbling through a capillary. The authors demonstrated continuous-flow ^1H, ^{13}C and ^{15}N SABRE hyperpolarisation, and reported comparable signal enhancements to those obtained using a semi-automated SABRE approach.

One limitation of flow-based automated pH$_2$ hyperpolarisation approaches is the length of time taken to transport the sample between polarisation and detection. Faster sample transfer preserves more hyperpolarisation by minimising relaxation, and reduces the minimum repetition time between experiments to improve overall efficiency. Shorter repetition delays can be achieved by using mechanical transport. One simple approach is to employ a robotic arm to rapidly transfer the sample between B_{PTF} and the benchtop NMR spectrometer. This method was used by Alcicek et al. to optimise ^{13}C and ^{15}N hyperpolarisation generated by PHIP-Relay for biologically relevant metabolites at natural isotopic abundance [125]. Alternatively, the rack and pinion actuator of Hövener and co-workers achieves rapid shuttling (36 cm in *ca.* 0.4 s) by limiting the motion of the sample to a single vertical axis [205].

Polarisation transfer within the magnetic field of the benchtop NMR spectrometer eliminates the need for sample transport, further improving the reproducibility of pH$_2$ hyperpolarisation experiments. In hydrogenative PHIP experiments, *in situ* signal enhancement can be achieved *via* the PASADENA effect. Ellermann et al. demonstrate average ^1H polarisation levels of 16.2% for ethyl acetate-d_6 following hydrogenation of vinyl pyruvate-d_6 at 0.55 T using this approach [206]. For SABRE experiments, the absence of LACs in the comparatively high detection field of a benchtop NMR spectrometer limits spontaneous polarisation transfer *in situ*. However, polarisation transfer can be achieved by using tailored RF irradiation to bring the spin system to an appropriate LAC condition in the rotating frame of reference [207,208]. A number of pulse schemes for *in situ* polarisation transfer to heteronuclei and ^1H have been developed for use at high field [161–164,207,209–211]. Of these, the spin-lock induced crossing (SLIC) method has been combined with benchtop NMR detection to achieve *in situ* ^{13}C and ^{15}N SABRE hyperpolarisation for a range of analytes at natural isotopic abundance, as demonstrated for ^{15}N in Fig. 19. A maximum of 12.1% and 0.4% ^{15}N and ^{13}C polarisation, respectively, was observed for 60 mM 4-aminopyridine [212].

A pertinent instrumentation challenge associated with combining all pH$_2$ bubbling methods with benchtop NMR detection is the field inhomogeneity caused by the introduction of a capillary into the detection region of the spectrometer. In contrast to the standard geometry of high-field NMR spectrometers, where the capillary is parallel to the B_0 field, most benchtop NMR spectrometers employ a magnetic field oriented perpendicular to the vertical sample axis. Therefore, despite
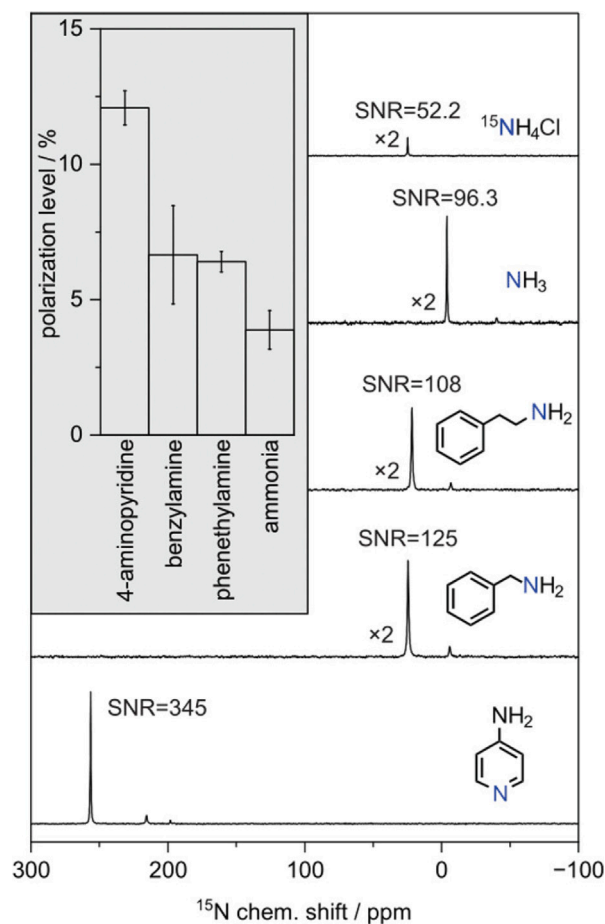
Fig. 19. ^{15}N benchtop (1 T) NMR spectra of a range of analytes at natural abundance hyperpolarised using SLIC-SABRE, with associated polarisation levels. Reprinted with permission from R. Kircher, J. Xu, D. A. Barskiy, Journal of the American Chemical Society 146 (1) (2024) 514–520. Copyright 2024 American Chemical Society.

the lower magnetic field, line broadening can be significant. This is particularly problematic for ^1H nuclei due to their narrow chemical shift range and higher gyromagnetic ratio compared to ^{13}C and ^{15}N. These effects can be avoided by terminating the capillary above the detection region (at the expense of pH$_2$ mixing efficiency), or minimised by using a very narrow capillary.

4. Chemically-induced dynamic nuclear polarisation (CIDNP)

4.1. Background theory of CIDNP and photo-CIDNP

Chemically-induced dynamic nuclear polarisation (CIDNP) is a hyperpolarisation phenomenon that was first observed by Bargon, Fischer and Johnsen in 1967 [213], with independent observations made by Ward and Lawler [214] later that same year. The respective authors reported anomalous signal intensities for products of chemical reactions involving free radical intermediates, indicating that these molecules were formed with non-equilibrium nuclear spin polarisation. Ward and Lawler suggested that this was the result of an electron–nuclear cross-relaxation effect in free radicals, similar to the Overhauser effect [214]. However, this mechanism was found to be inconsistent with a range of additional experimental observations, such as the dependence of signal enhancement on the type of chemical reaction performed, or the observation of hyperpolarisation in the absence of an external magnetic field [215]. A radical pair mechanism (RPM) was subsequently proposed by Closs [216,217], and Kaptein and Oosterhoff [218], to comprehensively explain the form of the observed CIDNP spectra.

The RPM arises from the conservation of electron spin angular momentum during a chemical reaction. This strong conservation effect means that nuclear spin states affect the reactivity of radical pairs, leading to spin-selective chemistry and the production of reaction products with non-equilibrium nuclear spin populations [152]. In 1978, Kaptein et al. demonstrated that the same hyperpolarisation effect could be observed in photochemical reactions between a photo-excited dye and certain amino acid residues (*e.g.*, histidine, tyrosine, and tryptophan) on the surface of a protein [219]. The photochemically induced dynamic nuclear polarisation (photo-CIDNP) effect has subsequently developed into a useful tool for the study of reactivity of short-lived free radicals of biologically relevant molecules, as well as for the study of protein structure and dynamics [220,221].

The CIDNP radical pair mechanism can be understood through consideration of the reaction scheme shown in Fig. 20 [222]. A molecule (P) that has been excited into a triplet state accepts an electron from a donor (Q) to form a spin correlated radical pair. This radical pair exists in a triplet electronic state, $^3P^{\bullet-}Q^{\bullet+}$, in order to satisfy the requirement that electron spin angular momentum is conserved. Once formed, the radical pair will either recombine, to form the original molecule (P) and donor (Q) as recombination products, or it will escape the solvent cage, diffuse apart, and eventually be scavenged to form escape products (P–X and Q–Y). In order to recombine, the radical pair must be in a singlet electronic state, meaning that it must first undergo triplet to singlet interconversion. The rate of triplet–singlet interconversion will depend on the spin states of any nuclei in $P^{\bullet-}$ or $Q^{\bullet+}$ that have a significant hyperfine coupling to the unpaired electrons. In the example in Fig. 20, the $|\beta\rangle$ state of a ^1H nucleus in $Q^{\bullet+}$ is assumed to give rise to a much faster rate of singlet–triplet interconversion than the $|\alpha\rangle$ state. In this case, radical pairs containing a ^1H spin in the $|\beta\rangle$ state will be much more likely to form the recombination products than those containing a ^1H in the $|\alpha\rangle$ state. Therefore, the radical pairs containing an $|\alpha\rangle$-state ^1H spin will have a greater probability of diffusing apart to eventually form the escape products (P–X and Q–Y). Due to this nuclear spin-selective reactivity, both the escape and recombination products will be formed with non-Boltzmann populations (*i.e.*, with a bias towards either the $|\beta\rangle$ or $|\alpha\rangle$ nuclear spin state), leading to the creation of hyperpolarisation. For the spin selection in this example, Q^* will be overpopulated in the $|\beta\rangle$ state and so will appear as an enhanced emission peak in the NMR spectrum, while $Q^* – Y$ will appear as an enhanced absorption peak due to an overpopulation of the $|\alpha\rangle$ state (Fig. 20). [222]

Photo-CIDNP is often carried out using a reversible reaction, where following separation the radicals react to reform the initial molecules, P and Q. In this case, one might expect to see no net hyperpolarisation because of the destructive interference between the negative polarisation for the in-cage recombination products and the positive polarisation for the escape products. In practice, the lifetime of the escaped radicals is much longer than for the radicals that recombine inside the solvent cage. Therefore, the enhanced nuclear spin polarisation of the escape radicals relaxes significantly, due to paramagnetic effects, prior to recombination. As a result, hyperpolarisation can be observed for the in-cage recombination products without destructive interference from the escape products [222]. The benefit of this reversible photo-CIDNP experiment is that it allows for repeated hyperpolarisation experiments on a single sample, through repeat irradiation.

4.2. Integration of photo-CIDNP with benchtop NMR detection

The experimental implementation of photo-CIDNP requires the addition of a small concentration of a photo-active dye to the solution, and the facility to irradiate the sample in order to photo-excite the dye. Photo-CIDNP is therefore significantly less demanding in terms of instrumentation than other hyperpolarisation methods and can be interfaced with the benchtop NMR spectrometer in a very straightforward manner. Bernarding et al. have recently demonstrated ^{19}F
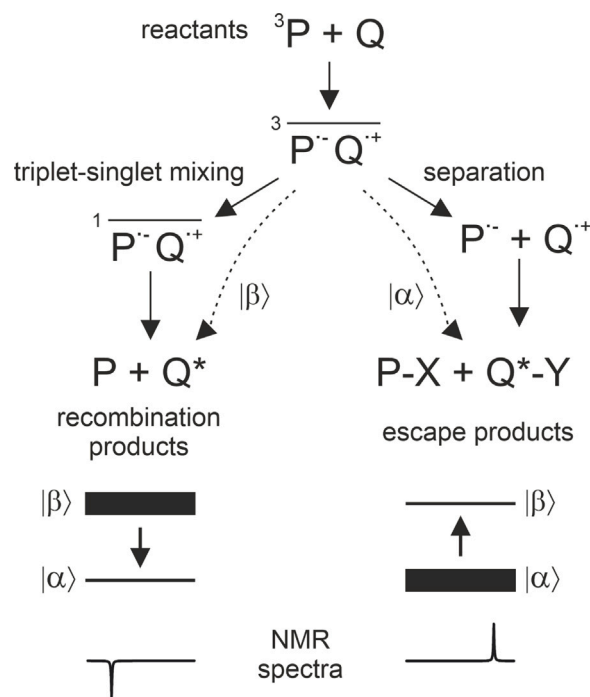

Fig. 20. Photo-CIDNP reaction scheme. Molecule P is photo-excited into a triplet state, which accepts an electron from a donor, Q, to produce a radical pair, $^3\overline{P^{\bullet-}Q^{\bullet+}}$. The triplet radical pair can either undergo triplet–singlet conversion and react to give recombination products (P and Q), or escape from the solvent cage, diffuse apart and get scavenged to give escape products (P–X and Q–Y). Here, faster triplet–singlet interconversion for radical pairs containing a Q proton in the $|\beta\rangle$ state results in a sorting of the $|\beta\rangle$ and $|\alpha\rangle$ nuclear spin states in Q between the recombination products and the escape products. As a result of the spin selection, both the recombination and escape products are formed with non-Boltzmann spin populations, as denoted by an asterisk, giving rise to NMR signal enhancement, illustrated schematically below [222].

photo-CIDNP with detection at 0.6 T using a low-cost, high-power blue LED for *in situ* sample irradiation [223]. While the focus of this work was on enhanced ^{19}F MRI, the authors demonstrated photo-CIDNP ^{19}F NMR spectra of an aqueous solution of 3-fluoro-D/L-tyrosine with the chromophore riboflavin 5'-monophosphate as the photosensitiser. The photo-CIDNP spectra were acquired following 15 s of illumination to produce an estimated signal enhancement factor of 465 relative to the spectrum without illumination. In this case the spectral resolution, and consequently the SNR, was limited by the instrumentation, which was optimised for MRI and therefore did not have high field homogeneity. Nevertheless, these promising results show the potential for photo-CIDNP to be implemented for *in situ* hyperpolarisation on a benchtop NMR spectrometer.

Another approach to photo-CIDNP-enhanced benchtop NMR spectroscopy was presented by Sheberstov et al. in 2021, in which ^{13}C and ^1H photo-CIDNP hyperpolarisation was generated by sample irradiation in the zero-to-ultra-low field (ZULF) or Earth's magnetic field (40 µT) regime, and then detected following sample transport into a 60 MHz (1.4 T) benchtop NMR spectrometer [224]. In these experiments, photo-CIDNP of *para*-benzoquinone was generated with tetraphenylporphyrin as the photosensitiser. Enhancement factors of approximately 200 were observed for ^1H nuclei directly bonded to ^{13}C, with significant hyperpolarisation also observed in $^{13}C\{^1H\}$ NMR spectra when photo-CIDNP was performed under ZULF conditions. These results were found to be repeatable over 100 repeat illuminations, highlighting the reversibility of the photo-CIDNP effect and the feasibility of using signal averaging to improve SNR. Sample transport between the ZULF or Earth's field regime into the benchtop NMR spectrometer was achieved using a robotic arm.
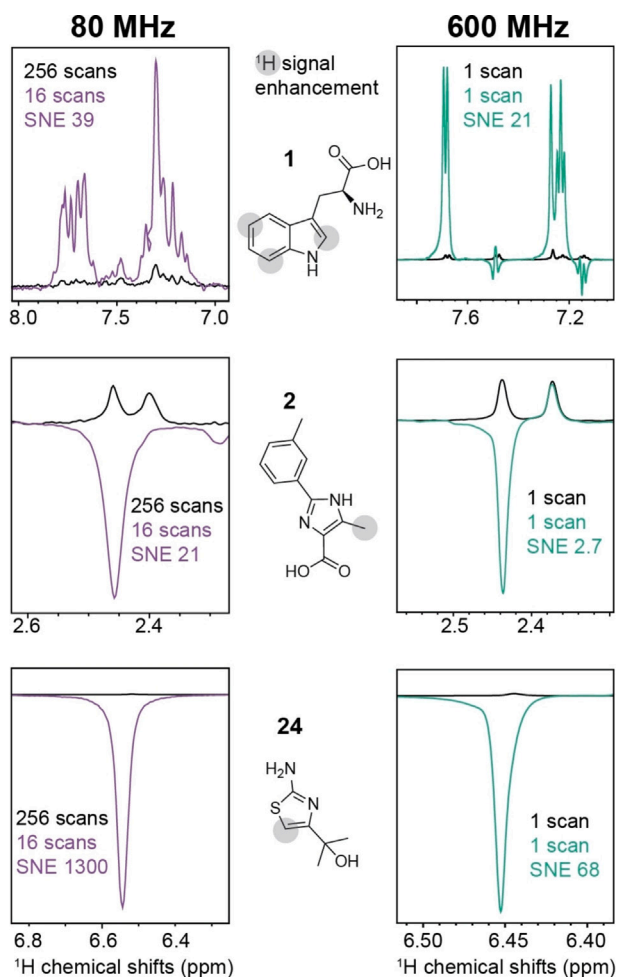
Fig. 21. Comparison of thermally polarised and photo-CIDNP hyperpolarised ^{1}H 1D spectra for **1**, **2** and **24** at 80 MHz (left) and 600 MHz (right). Samples contained 500 µM of each compound in photo-CIDNP buffer and were irradiated for 6 s (80 MHz) or 2 s (600 MHz) prior to each scan. Spectra show the signals with the largest enhancements for each compound, which are highlighted in grey on the chemical structure. Reprinted with permission under a CC-BY licence from Ref. [225].

More recently, Stadler et al. have demonstrated *in situ* photo-CIDNP on an 80 MHz (1.9 T) benchtop NMR spectrometer for fragment screening applications [225]. In these experiments, fluorescein was used as the photosensitiser and irradiation was achieved at 450 nm (1 W) by a laser diode coupled to an optical fibre inserted into the NMR sample inside the benchtop NMR spectrometer. A range of compounds in the millimolar concentration regime were enhanced by factors ranging from 20 to 1300-fold (Fig. 21). These were directly compared to results acquired at 600 MHz, where the maximum enhancement for the same compounds was 68-fold. The repeatability of photo-CIDNP was exploited to signal average for 3 min to optimise SNR, enabling detection of 2-(2-aminothiazol-4-yl)propan-2-ol down to a concentration of 250 nM.

Photo-CIDNP presents a number of very promising advantages for hyperpolarised benchtop NMR spectroscopy applications, including the limited instrumentation and sample preparation requirements; the generation of renewable *in situ* hyperpolarisation, which enables signal averaging and multi-step experiments; and the high level of signal enhancement observed in the moderate fields of benchtop NMR spectrometers. One potential limitation of this approach is the range of molecules that can be enhanced. Until recently, photo-CIDNP research has focused on a relatively restricted chemical space comprising the

aromatic amino acids (tryptophan, tyrosine, histidine) and their derivatives [222,226,227]. However, recent work by Torres et al. [228] has demonstrated observable photo-CIDNP enhancement for a much broader range of small molecules that include aromatic functionality. Following screening of a library of small molecules (<300 Da), each containing at least one aromatic feature, 340 were found to produce an observable photo-CIDNP response, while 266 were not photo-CIDNP active. This promising success rate suggests that the scope of potential targets for hyperpolarisation by photo-CIDNP is likely to be much larger than previously thought.

Fragment screening for drug discovery is a very promising application of photo-CIDNP that has been implemented with both high-field [228] and benchtop NMR detection [225]. This method takes advantage of the fact that when a hyperpolarised molecule binds to the target, for example a protein, its hyperpolarisation lifetime is significantly reduced due to enhanced longitudinal relaxation [228]. In these photo-CIDNP experiments, the hyperpolarisation is built up over a period of time during irradiation (2–6 s). The level of hyperpolarisation that is observed following irradiation will be influenced by the hyperpolarisation lifetime. To detect a binding event, the researchers measured a polarisation ratio, $P_{PL/L} = P_{PL}/P_L$, from measurements of the polarisation level of the ligand in the presence of the protein, P_{PL}, and in the absence of protein, P_L. A value of $P_{PL/L} = 1$ indicates no change in polarisation level and hence no binding, while $P_{PL/L} = 0$ indicates a reduction in hyperpolarisation lifetime such that no signal is observed in the presence of the protein (strong binding). In the study of Stadler et al., 32 fragments that showed photo-CIDNP activity were screened with the cancer-related protein PIN1 using benchtop NMR detection with 3 min of signal averaging [225]. Using a cut-off of $P_{PL/L} = 0.9$ to define a 'hit' and 500 µM of fragment to 10 µM of protein, 6 hits were identified and verified through literature experiments and comparison to standard high-field fragment screening methods. Comparison with analogous experiments using 600 MHz (14.1 T) NMR detection showed that larger polarisation differences were observed with benchtop NMR detection, reflecting the enhanced relaxation contrast at 1.9 T. Therefore, this very promising application of photo-CIDNP is a case where not only does hyperpolarisation enable the use of cheaper and more portable instrumentation, but the quality of the information obtained is also improved.

5. Perspectives for analytical applications

The use of hyperpolarisation to overcome the sensitivity limitations of benchtop NMR opens up a range of new potential applications. Of particular interest are applications outside of the traditional laboratory environment or where the cost and maintenance requirements of standard high-field NMR spectrometers are prohibitive.

One application is for the study of complex mixtures, including for the analysis of biofluids in clinical practice or in the field of metabolomics. The reduced size and cost of benchtop NMR instrumentation would allow for integration within routine clinical practice, making it particularly attractive for point-of-care diagnostics [229, 230]. Similarly, the portability and accessibility of benchtop NMR holds promise for applications in detecting food adulteration [231,232], environmental monitoring [20,233], and forensics [234]. In all of these cases, hyperpolarisation can be exploited to reduce the limits of detection of benchtop NMR to clinically and environmentally relevant levels, and to enable detection of information-rich, low-sensitivity nuclei such as ^{13}C at natural isotopic abundance.

Hyperpolarisation using dDNP has been successfully combined with high-field ^{1}H and ^{13}C NMR detection for the analysis of biofluids for metabolomic applications [235–238]. Dissolution DNP is a particularly promising method for untargeted analysis due to the non-specific nature of the polarisation transfer. One limitation of dDNP is that it requires significant sample preparation to enable efficient polarisation transfer at cryogenic temperatures, and, in general, a single sample

can only be hyperpolarised once. A recent working paper by Bocquelet et al. proposes a novel route to renewable dDNP polarisation through repeated freeze-DNP-melt-flow cycles, where polarisation transfer is achieved at 77 K in a 1 T permanent magnet array [239]. If fully realised, this approach would overcome many of the limitations of dDNP for analytical applications that were highlighted above.

An alternative approach is to use the chemical specificity of *para*hydrogen-based methods to target a subgroup of molecules containing a specific chemical moiety within a complex mixture. An example of this is the chemo-sensing method, non-hydrogenative (nh) PHIP [240]. As in SABRE, nhPHIP uses a transition metal complex to reversibly bind pH_2 and generate hyperpolarisation. A key difference is that in nhPHIP the hyperpolarisation of the pH_2-derived hydrides is detected without polarisation transfer to the target analyte. Target molecules that reversibly bind to the hyperpolarisation complex are detected indirectly through the pH_2-derived hydrides, whose chemical shifts are highly sensitive to the identity of the other ligands bound to the metal centre. High-field ^1H NMR coupled with nhPHIP has been used for the detection and quantification of amino acids in urine [241], and to perform pharmacokinetic studies of nicotine and its metabolites in urine [242]. A significant advantage of nhPHIP is that it is a liquid-phase technique and the sample can be repolarised multiple times. A limitation, particularly for use with benchtop NMR, is signal overlap in the hydride region of the ^1H NMR spectrum.

A standard method to address spectral congestion in NMR is to spread the peaks over multiple axes. A challenge for hyperpolarised multidimensional NMR is the single shot nature of many hyperpolarisation techniques. Even for methods like ODNP, SABRE, nhPHIP, and photo-CIDNP, where a single sample can be re-polarised multiple times, the reproducibility of the hyperpolarisation response is crucial for obtaining high quality spectra. Furthermore, 2D spectral acquisition can be very time-consuming. A promising approach to overcome these issues is to combine hyperpolarisation with ultrafast (UF) NMR experiments, where spatial encoding is used to acquire a 2D spectrum within a single acquisition period [243]. UF benchtop NMR spectroscopy has been implemented by Gouilleux et al. [244], and was recently combined with the HYPNOESYS (Hyperpolarized Nuclear Overhauser Effect System) hyperpolarisation method by Parker et al. [245] Non-uniform sampling (NUS) is another approach to improving the efficiency of 2D spectral acquisition [246]. NUS has been found to improve the performance of multidimensional benchtop NMR measurements [247], and has been successfully integrated with PHIP hyperpolarisation on a benchtop NMR spectrometer [202].

Peak overlap can also be overcome through the use of spectral editing to simplify benchtop NMR spectra. This can be achieved using selective detection methods, such as Designed Refocused Excitation And optional Mixing for Targets In vivo and Mixture Elucidation (DREAMTIME) [248], and Gradient-Enhanced Multiplet-Selective Targeted-Observation NMR Experiment (GEMSTONE) [249], or pure shift approaches that remove homonuclear couplings [250–252]. Recently, these methods have been implemented successfully on a benchtop NMR spectrometer [253,254]. While effective for the analysis of complex mixtures by NMR, selective detection and pure shift methods almost always lead to a significant reduction in sensitivity. Therefore, combining them with hyperpolarisation, as previously demonstrated at high field [255–257], presents a particularly attractive prospect for benchtop NMR spectroscopy.

Another benefit of the compact nature of benchtop NMR is that it can be integrated with other orthogonal analytical methods, such as ultraviolet (UV) [258] and infrared (IR) [259] spectroscopy or mass spectrometry, [260,261] to provide enhanced chemical discrimination. Integrating hyperpolarisation to increase the sensitivity of the benchtop NMR detection would further boost the analytical power of these methods. Similarly, *in situ* UV–visible irradiation can be achieved in a relatively straightforward way with benchtop NMR, as demonstrated in the photo-CIDNP experiments of Stadler et al. [225] Photo-irradiation

can also be used in combination with *para*hydrogen based hyperpolarisation techniques, as previously demonstrated using high-field NMR detection [262–265].

Probing biomolecular interactions using hyperpolarised NMR is an area that has seen significant progress in recent years. At high field, water hyperpolarised by dDNP has been used to enhance the signals of labile protons in solvent-exposed protein residues, to boost sensitivity and enable the study of structural dynamics at physiological concentrations [266–269]. While a similar hyperpolarisation approach would be feasible with benchtop NMR detection, the analysis of biomolecules at low field is significantly limited by signal overlap. A more promising approach is to use a hyperpolarised probe molecule to detect biomolecular interactions, as in the fragment-based screening experiments of Stadler et al. [225] In this case, only the hyperpolarised probe molecule is directly detected and so the protein signals do not need to be resolved. Background-free measurements can be achieved using ^{19}F NMR detection, as has been demonstrated at high field, where ^{19}F hyperpolarisation was generated *via* transfer from dDNP-enhanced water [270] or direct ^{19}F dDNP [271]. The use of ^{19}F detection is particularly promising for benchtop NMR because additional instrumentation is not typically required to detect ^{19}F due to the close proximity of the Larmor frequencies of ^1H and ^{19}F in fields of 1–2 T. Recently, Pham and Hilty have demonstrated a SABRE-based hyperpolarisation approach to observe biomolecular interactions *via* low-field NMR detection without the need for chemical shift resolution [272]. In this work, protein–ligand interactions were probed through changes in the transverse relaxation rate of a protein-specific molecule optimised for ^{19}F SABRE hyperpolarisation. The hyperpolarised ^{19}F-containing molecule acts as a reporter for the binding of the target ligand, *via* competition. The authors demonstrated that the dissociation constant for the target could be determined from changes in the R_2 relaxation rate of the ^{19}F molecule enhanced by SABRE [272].

Reaction and process monitoring is another area where hyperpolarised benchtop NMR can make a significant impact. On-line and at-line process monitoring using benchtop NMR for industrial applications has been explored previously in the literature [273–275]. Benchtop NMR has also been implemented into high-throughput screening workflows to monitor and optimise synthetic procedures [19,276]. Process monitoring and optimisation are often carried out under continuous flow, which exacerbates the sensitivity challenge of benchtop NMR due to the short residence time of the sample in the magnetic field of the spectrometer. Hyperpolarisation under continuous flow conditions has been demonstrated for ODNP [58], SABRE [277] and hydrogenative PHIP [202]. A significant advantage of the ODNP approach of Kircher et al. is that the polarisation transfer agent is immobilised within the ODNP polariser that is in-line with the benchtop NMR detector, meaning that it does not need to be added to the sample under investigation. The development of heterogeneous catalysts for PHIP and SABRE could enable a similar approach to be used for *para*hydrogen hyperpolarisation [278,279]. The SWAMP (surface waters are magnetised by *para*hydrogen) method, introduced by Bowers and co-workers in 2018, could also provide a route to continuous pH_2 hyperpolarisation [280]. In this method, hyperpolarisation is achieved through adsorption of pH_2 onto the surface of a Pt_3Sn nanoparticle encapsulated in mesoporous silica. Spin–spin interactions with the surface break the symmetry of pH_2, generating hyperpolarisation. Subsequent proton exchange enables the transfer of polarisation to solvent molecules at the surface (*e.g.*, water, methanol or ethanol). The SWAMP effect was demonstrated with benchtop NMR detection by Norcott in 2023, who showed that it could be achieved using simple, commercially available heterogeneous hydrogenation catalysts, such as platinum-on-carbon, at room temperature [188]. In this case an additive is required to regenerate the surface and allow for renewable hyperpolarisation.

6. Conclusions

The development of hyperpolarised benchtop NMR spectroscopy has progressed rapidly since the first demonstrations of dDNP [85] and SABRE-enhanced [179] benchtop NMR in 2016. In terms of volume of literature, the dominant technique has been pH$_2$ hyperpolarisation. This is likely due to the fact that the instrumentation requirements for pH$_2$ hyperpolarisation are simpler and cheaper than for other methods, and pH$_2$ instrumentation developed for high-field NMR detection is easily transferable to benchtop NMR. Furthermore, since the levels of hyperpolarisation observed are independent of detection field strength, there has been wide uptake of benchtop NMR detection within the pH$_2$ hyperpolarisation community as a cost-effective route for method development and optimisation [124,186–189,194,281–283]. This latter point is equally true for dDNP, leading to a growing number of dDNP developments that were first demonstrated using benchtop NMR detection [68,86–89]. The recent demonstration of photo-CIDNP for fragment-based screening on a benchtop NMR spectrometer [225], where the instrumentation requirements are arguably even simpler and cheaper than for pH$_2$ hyperpolarisation, is likely to stimulate a lot of interest and development in the area of photo-induced hyperpolarisation with benchtop NMR detection.

This review has focused on the hyperpolarisation approaches of DNP, PHIP and photo-CIDNP, which have already been successfully combined with benchtop NMR and show promise for analytical applications. However, the analytical potential of hyperpolarised benchtop NMR is not limited to these methods. A wide range of further hyperpolarisation techniques exist or are under development, as illustrated in the recent comprehensive review of spin hyperpolarisation by Eills et al. [25] This includes methods such as HYPNOESYS [245,284], that have been demonstrated using benchtop NMR detection. Therefore, we believe that the potential of hyperpolarised benchtop NMR spectroscopy is very broad, and will continue to expand as new methods are introduced. Going forward, there remain barriers to the uptake of hyperpolarised benchtop NMR for analytical applications outside of the expert hyperpolarisation community. These include the limited commercial availability of instrumentation and consumables, such as polarisation agents and catalysts; the amount of optimisation required to achieve high levels of polarisation for a wide range of target molecules; and ongoing challenges associated with the reproducibility and quantification of hyperpolarised signals. These aspects are all under active investigation within the hyperpolarisation community, and given the remarkable pace of progress in recent years we expect that it will not be long before the first real-world analytical applications of hyperpolarised benchtop NMR spectroscopy emerge.

CRediT authorship contribution statement

Ana I. Silva Terra: Writing – original draft, Writing – review & editing. **Daniel A. Taylor:** Writing – original draft, Writing – review & editing. **Meghan E. Halse:** Writing – original draft, Writing – review & editing.

Declaration of competing interest

The authors declare that they have no known competing financial interests or personal relationships that could have appeared to influence the work reported in this paper.

Acknowledgements

Data availability

No data was used for the research described in the article.

References

[1] E. Luchinat, L. Barbieri, M. Cremonini, L. Banci, Protein in-cell NMR spectroscopy at 1.2 GHz, J. Biomol. NMR 75 (2–3) (2021) 97–107, http://dx.doi.org/10.1007/s10858-021-00358-w.

[2] A. Siddhantakar, J. Santillán-Saldivar, T. Kippes, G. Sonnemann, A. Reller, S.B. Young, Helium resource global supply and demand: Geopolitical supply risk analysis, Resour. Conserv. Recy. 193 (2023) 106935, http://dx.doi.org/10.1016/j.resconrec.2023.106935.

[3] B. Blümich, K. Singh, Desktop NMR and its applications from materials science to organic chemistry, Angew. Chem. Int. Ed. 57 (24) (2018) 6996–7010, http://dx.doi.org/10.1002/anie.201707084.

[4] S.S. Zalesskiy, E. Danieli, B. Blümich, V.P. Ananikov, Miniaturization of NMR systems: Desktop spectrometers, microcoil spectroscopy, and "NMR on a chip" for chemistry, biochemistry, and industry, Chem. Rev. 114 (11) (2014) 5641–5694, http://dx.doi.org/10.1021/cr400063g.

[5] D. Capitani, A.P. Sobolev, V. Di Tullio, L. Mannina, N. Proietti, Portable NMR in food analysis, Chem. Biol. Technol. Agric. 4 (1) (2017) 17, http://dx.doi.org/10.1186/s40538-017-0100-1.

[6] B.P. Hills, Applications of low-field NMR to food science, in: G.A. Webb (Ed.), in: Annual Reports on NMR Spectroscopy, vol. 58, Academic Press, 2006, pp. 177–230, http://dx.doi.org/10.1016/S0066-4103(05)58004-9.

[7] M. Elsayed, A. Isah, M. Hiba, A. Hassan, K. Al-Garadi, M. Mahmoud, A. El-Husseiny, A.E. Radwan, A review on the applications of nuclear magnetic resonance (NMR) in the oil and gas industry: laboratory and field-scale measurements, J. Petroleum Explor. Prod. Technol. 12 (10) (2022) 2747–2784, http://dx.doi.org/10.1007/s13202-022-01476-3.

[8] S. Luo, J. Guo, L. Xiao, Prospects of borehole NMR instruments and applications, Magn. Reson. Lett. 2 (4) (2022) 224–232, http://dx.doi.org/10.1016/j.mrl.2022.08.002.

[9] M. Pinter, T. Harter, M. McCarthy, M. Augustine, Towards using NMR to screen for spoiled tomatoes stored in 1,000 L, aseptically sealed, metal-lined totes, Sensors 14 (3) (2014) 4167–4176, http://dx.doi.org/10.3390/s140304167.

[10] Y.-Q. Song, R. Kausik, NMR application in unconventional shale reservoirs – A new porous media research frontier, Prog. Nucl. Magn. Reson. Spectrosc. 112–113 (2019) 17–33, http://dx.doi.org/10.1016/j.pnmrs.2019.03.002.

[11] E. Danieli, J. Mauler, J. Perlo, B. Blümich, F. Casanova, Mobile sensor for high resolution NMR spectroscopy and imaging, J. Magn. Reson. 198 (1) (2009) 80–87, http://dx.doi.org/10.1016/j.jmr.2009.01.022.

[12] B. Blümich, Low-field and benchtop NMR, J. Magn. Reson. 306 (2019) 27–35, http://dx.doi.org/10.1016/j.jmr.2019.07.030.

[13] Nanalysis, Nanalysis, URL https://www.nanalysis.com.

[14] Magritek, Magritek | Benchtop NMR performance and quality, URL https://magritek.com/.

[15] Q Magnetics, Q Magnetics | 125 MHz benchtop NMR spectrometer, URL https://www.qmagnetics.com.

[16] Bruker, Benchtop NMR | system | solutions, URL https://www.bruker.com/en/products-and-solutions/mr/nmr/fourier80.html.

[17] S.K. Küster, E. Danieli, B. Blümich, F. Casanova, High-resolution NMR spectroscopy under the fume hood, Phys. Chem. Chem. Phys. 13 (29) (2011) 13172, http://dx.doi.org/10.1039/c1cp21180c.

[18] G. Pagès, A. Gerdova, D. Williamson, V. Gilard, R. Martino, M. Malet-Martino, Evaluation of a benchtop cryogen-free low-field ^{1}H NMR spectrometer for the analysis of sexual enhancement and weight loss dietary supplements adulterated with pharmaceutical substances, Anal. Chem. 86 (23) (2014) 11897–11904, http://dx.doi.org/10.1021/ac503699u.

[19] S. Kern, L. Wander, K. Meyer, S. Guhl, A.R.G. Mukkula, M. Holtkamp, M. Salge, C. Fleischer, N. Weber, R. King, S. Engell, A. Paul, M.P. Remelhe, M. Maiwald, Flexible automation with compact NMR spectroscopy for continuous production of pharmaceuticals, Anal. Bioanal. Chem. 411 (14) (2019) 3037–3046, http://dx.doi.org/10.1007/s00216-019-01752-y.

[20] K. Heerah, S. Waclawek, J. Konzuk, J.G. Longstaffe, Benchtop ^{19}F NMR spectroscopy as a practical tool for testing of remedial technologies for the degradation of perfluorooctanoic acid, a persistent organic pollutant, Magn. Reson. Chem. 58 (12) (2020) 1160–1167, http://dx.doi.org/10.1002/mrc.5005.

[21] R. Chen, P. Singh, S. Su, S. Kocalar, X. Wang, N. Mandava, S. Venkatesan, A. Ferguson, A. Rao, E. Le, C. Rojas, E. Njoo, Benchtop ^{19}F nuclear magnetic resonance (NMR) spectroscopy provides mechanistic insight into the biginelli condensation toward the chemical synthesis of novel trifluorinated dihydro- and tetrahydropyrimidinones as antiproliferative agents, ACS Omega 8 (11) (2023) 10545–10554, http://dx.doi.org/10.1021/acsomega.3c00290.

[22] B. Gouilleux, N.V. Christensen, K.G. Malmos, T. Vosegaard, Analytical evaluation of low-field ^{31}P NMR spectroscopy for lipid analysis, Anal. Chem. 91 (4) (2019) 3035–3042, http://dx.doi.org/10.1021/acs.analchem.8b05416.

[23] L. Tadiello, H.-J. Drexler, T. Beweries, Low-field flow ^{31}P NMR spectroscopy for organometallic chemistry: On-line analysis of highly air-sensitive rhodium diphosphine complexes, Organometallics 41 (20) (2022) 2833–2843, http://dx. doi.org/10.1021/acs.organomet.2c00301.

[24] B. Bogun, S. Moore, 1H and 31P benchtop NMR of liquids and solids used in and/or produced during the manufacture of methamphetamine by the HI reduction of pseudoephedrine/ephedrine, Forensic Sci. Int. 278 (2017) 68–77, http://dx.doi.org/10.1016/j.forsciint.2017.06.026.

[25] J. Eills, D. Budker, S. Cavagnero, E.Y. Chekmenev, S.J. Elliott, S. Jannin, A. Lesage, J. Matysik, T. Meersmann, T. Prisner, J.A. Reimer, H. Yang, I.V. Koptyug, Spin hyperpolarization in modern magnetic resonance, Chem. Rev. 123 (4) (2023) 1417–1551, http://dx.doi.org/10.1021/acs.chemrev.2c00534.

[26] A.W. Overhauser, Overhauser, albert w.: Dynamic nuclear polarization, in: R.K. Harris (Ed.), Encyclopedia of Magnetic Resonance, John Wiley & Sons, Ltd, Chichester, UK, 2007, p. emrhp0135, http://dx.doi.org/10.1002/9780470034590.emrhp0135.

[27] A.W. Overhauser, Paramagnetic relaxation in metals, Phys. Rev. 89 (4) (1953) 689–700, http://dx.doi.org/10.1103/PhysRev.89.689.

[28] T.R. Carver, C.P. Slichter, Polarization of nuclear spins in metals, Phys. Rev. 92 (1) (1953) 212–213, http://dx.doi.org/10.1103/PhysRev.92.212.2.

[29] R.A. Wind, M.J. Duijvestijn, C. van der Lugt, A. Manenschijn, J. Vriend, Applications of dynamic nuclear polarization in 13C NMR in solids, Prog. Nucl. Magn. Reson. Spectrosc. 17 (1985) 33–67, http://dx.doi.org/10.1016/0079-6565(85)80005-4.

[30] L.R. Becerra, G.J. Gerfen, R.J. Temkin, D.J. Singel, R.G. Griffin, Dynamic nuclear polarization with a cyclotron resonance maser at 5 T, Phys. Rev. Lett. 71 (21) (1993) 3561–3564, http://dx.doi.org/10.1103/PhysRevLett.71.3561.

[31] D.A. Hall, D.C. Maus, G.J. Gerfen, S.J. Inati, L.R. Becerra, F.W. Dahlquist, R.G. Griffin, Polarization-enhanced NMR spectroscopy of biomolecules in frozen solution, Science 276 (5314) (1997) 930–932, http://dx.doi.org/10.1126/science.276.5314.930.

[32] Y. Su, L. Andreas, R.G. Griffin, Magic angle spinning NMR of proteins: High-frequency dynamic nuclear polarization and 1H detection, Annu. Rev. Biochem. 84 (1) (2015) 465–497, http://dx.doi.org/10.1146/annurev-biochem-060614-034206.

[33] Q.Z. Ni, E. Daviso, T.V. Can, E. Markhasin, S.K. Jawla, T.M. Swager, R.J. Temkin, J. Herzfeld, R.G. Griffin, High frequency dynamic nuclear polarization, Acc. Chem. Res. 46 (9) (2013) 1933–1941, http://dx.doi.org/10.1021/ar300348n.

[34] A.G.M. Rankin, J. Trébosc, F. Pourpoint, J.-P. Amoureux, O. Lafon, Recent developments in MAS DNP-NMR of materials, Solid State Nucl. Magn. Reson. 101 (2019) 116–143, http://dx.doi.org/10.1016/j.ssnmr.2019.05.009.

[35] A.J. Rossini, A. Zagdoun, M. Lelli, A. Lesage, C. Copéret, L. Emsley, Dynamic nuclear polarization surface enhanced NMR spectroscopy, Acc. Chem. Res. 46 (9) (2013) 1942–1951, http://dx.doi.org/10.1021/ar300322x.

[36] L.H. Bennett, H.C. Torrey, High negative nuclear polarizations in a liquid, Phys. Rev. 108 (2) (1957) 499–500, http://dx.doi.org/10.1103/PhysRev.108.499.

[37] J.M. Franck, A. Pavlova, J.A. Scott, S. Han, Quantitative cw overhauser effect dynamic nuclear polarization for the analysis of local water dynamics, Prog. Nucl. Magn. Reson. Spectrosc. 74 (2013) 33–56, http://dx.doi.org/10.1016/j.pnmrs.2013.06.001.

[38] J.H. Ardenkjær-Larsen, B. Fridlund, A. Gram, G. Hansson, L. Hansson, M.H. Lerche, R. Servin, M. Thaning, K. Golman, Increase in signal-to-noise ratio of > 10,000 times in liquid-state NMR, Proc. Natl. Acad. Sci. 100 (18) (2003) 10158–10163, http://dx.doi.org/10.1073/pnas.1733835100.

[39] K. Golman, R. in 't Zandt, M. Thaning, Real-time metabolic imaging, Proc. Natl. Acad. Sci. 103 (30) (2006) 11270–11275, http://dx.doi.org/10.1073/pnas.0601319103.

[40] F.A. Gallagher, M.I. Kettunen, K.M. Brindle, Biomedical applications of hyperpolarized 13C magnetic resonance imaging, Prog. Nucl. Magn. Reson. Spectrosc. 55 (4) (2009) 285–295, http://dx.doi.org/10.1016/j.pnmrs.2009.06.001.

[41] S.J. Nelson, J. Kurhanewicz, D.B. Vigneron, P.E.Z. Larson, A.L. Harzstark, M. Ferrone, M. van Criekinge, J.W. Chang, R. Bok, I. Park, G. Reed, L. Carvajal, E.J. Small, P. Munster, V.K. Weinberg, J.H. Ardenkjaer-Larsen, A.P. Chen, R.E. Hurd, L.-I. Odegardstuen, F.J. Robb, J. Tropp, J.A. Murray, Metabolic imaging of patients with prostate cancer using hyperpolarized [1-13C]pyruvate, Sci. Transl. Med. 5 (198) (2013) http://dx.doi.org/10.1126/scitranslmed.3006070.

[42] F.A. Gallagher, R. Woitek, M.A. McLean, A.B. Gill, R. Manzano Garcia, E. Provenzano, F. Riemer, J. Kaggie, A. Chhabra, S. Ursprung, J.T. Grist, C.J. Daniels, F. Zaccagna, M.-C. Laurent, M. Locke, S. Hilborne, A. Frary, T. Torheim, C. Boursnell, A. Schiller, I. Patterson, R. Slough, B. Carmo, J. Kane, H. Biggs, E. Harrison, S.S. Deen, A. Patterson, T. Lanz, Z. Kingsbury, M. Ross, B. Basu, R. Baird, D.J. Lomas, E. Sala, J. Wason, O.M. Rueda, S.-F. Chin, I.B. Wilkinson, M.J. Graves, J.E. Abraham, F.J. Gilbert, C. Caldas, K.M. Brindle, Imaging breast cancer using hyperpolarized carbon-13 MRI, Proc. Natl. Acad. Sci. 117 (4) (2020) 2092–2098, http://dx.doi.org/10.1073/pnas.1913841117.

[43] J.-N. Dumez, J. Milani, B. Vuichoud, A. Bornet, J. Lalande-Martin, I. Tea, M. Yon, M. Maucourt, C. Deborde, A. Moing, L. Frydman, G. Bodenhausen, S. Jannin, P. Giraudeau, Hyperpolarized NMR of plant and cancer cell extracts at natural abundance, Analyst 140 (17) (2015) 5860–5863, http://dx.doi.org/10.1039/C5AN01203A.

[44] A. Bornet, M. Maucourt, C. Deborde, D. Jacob, J. Milani, B. Vuichoud, X. Ji, J.-N. Dumez, A. Moing, G. Bodenhausen, S. Jannin, P. Giraudeau, Highly repeatable dissolution dynamic nuclear polarization for heteronuclear NMR metabolomics, Anal. Chem. 88 (12) (2016) 6179–6183, http://dx.doi.org/10.1021/acs.analchem.6b01094.

[45] I. Solomon, Relaxation processes in a system of two spins, Phys. Rev. 99 (2) (1955) 559–565, http://dx.doi.org/10.1103/PhysRev.99.559.

[46] M. Bennati, C. Luchinat, G. Parigi, M.-T. Türke, Water 1H relaxation dispersion analysis on a nitroxide radical provides information on the maximal signal enhancement in overhauser dynamic nuclear polarization experiments, Phys. Chem. Chem. Phys. 12 (22) (2010) 5902, http://dx.doi.org/10.1039/c002304n.

[47] E. Ravera, C. Luchinat, G. Parigi, Basic facts and perspectives of overhauser DNP NMR, J. Magn. Reson. 264 (2016) 78–87, http://dx.doi.org/10.1016/j.jmr.2015.12.013.

[48] N.M. Loening, M. Rosay, V. Weis, R.G. Griffin, Solution-state dynamic nuclear polarization at high magnetic field, J. Am. Chem. Soc. 124 (30) (2002) 8808–8809, http://dx.doi.org/10.1021/ja026660g.

[49] D. Sezer, M.J. Prandolini, T.F. Prisner, Dynamic nuclear polarization coupling factors calculated from molecular dynamics simulations of a nitroxide radical in water, Phys. Chem. Chem. Phys. 11 (31) (2009) 6626, http://dx.doi.org/10.1039/b905709a.

[50] S.E. Küçük, T. Biktagirov, D. Sezer, Carbon and proton overhauser DNP from MD simulations and ab initio calculations: TEMPOL in acetone, Phys. Chem. Chem. Phys. 17 (38) (2015) 24874–24884, http://dx.doi.org/10.1039/C5CP04405G.

[51] B.D. Armstrong, M.D. Lingwood, E.R. McCarney, E.R. Brown, P. Blümler, S. Han, Portable X-band system for solution state dynamic nuclear polarization, J. Magn. Reson. 191 (2) (2008) 273–281, http://dx.doi.org/10.1016/j.jmr.2008.01.004.

[52] K. Münnemann, C. Bauer, J. Schmiedeskamp, H.W. Spiess, W.G. Schreiber, D. Hinderberger, A mobile DNP polarizer for clinical applications, Appl. Magn. Reson. 34 (3–4) (2008) 321–330, http://dx.doi.org/10.1007/s00723-008-0130-8.

[53] T. Überrück, M. Adams, J. Granwehr, B. Blümich, A compact X-band ODNP spectrometer towards hyperpolarized 1H spectroscopy, J. Magn. Reson. 314 (2020) 106724, http://dx.doi.org/10.1016/j.jmr.2020.106724.

[54] T.J. Keller, A.J. Laut, J. Sirigiri, T. Maly, High-resolution overhauser dynamic nuclear polarization enhanced proton NMR spectroscopy at low magnetic fields, J. Magn. Reson. 313 (2020) 106719, http://dx.doi.org/10.1016/j.jmr.2020.106719.

[55] Y.-s. Lee, D.-Y. Lim, J.H. Shim, Overhauser dynamic nuclear polarization for benchtop NMR system using a permanent magnet of 1.56 T, J. Korean Magn. Reson. Soc. 23 (3) (2019) 81–86, http://dx.doi.org/10.6564/JKMRS.2019.23.3.081.

[56] C. Griesinger, M. Bennati, H. Vieth, C. Luchinat, G. Parigi, P. Höfer, F. Engelke, S. Glaser, V. Denysenkov, T. Prisner, Dynamic nuclear polarization at high magnetic fields in liquids, Prog. Nucl. Magn. Reson. Spectrosc. 64 (2012) 4–28, http://dx.doi.org/10.1016/j.pnmrs.2011.10.002.

[57] M. Reinhard, M. Levien, M. Bennati, T. Orlando, Large 31 P-NMR enhancements in liquid state dynamic nuclear polarization through radical/target molecule non-covalent interaction, Phys. Chem. Chem. Phys. 25 (1) (2023) 822–828, http://dx.doi.org/10.1039/D2CP04092A.

[58] R. Kircher, H. Hasse, K. Münnemann, High flow-rate benchtop NMR spectroscopy enabled by continuous overhauser DNP, Anal. Chem. 93 (25) (2021) 8897–8905, http://dx.doi.org/10.1021/acs.analchem.1c01118.

[59] E.R. McCarney, B.D. Armstrong, M.D. Lingwood, S. Han, Hyperpolarized water as an authentic magnetic resonance imaging contrast agent, Proc. Natl. Acad. Sci. 104 (6) (2007) 1754–1759, http://dx.doi.org/10.1073/pnas.0610540104.

[60] E.R. McCarney, S. Han, Spin-labeled gel for the production of radical-free dynamic nuclear polarization enhanced molecules for NMR spectroscopy and imaging, J. Magn. Reson. 190 (2) (2008) 307–315, http://dx.doi.org/10.1016/j.jmr.2007.11.013.

[61] S. Ebert, A. Amar, C. Bauer, M. Kölzer, P. Blümler, H.W. Spiess, D. Hinderberger, K. Münnemann, A mobile DNP polarizer for continuous flow applications, Appl. Magn. Reson. 43 (1–2) (2012) 195–206, http://dx.doi.org/10.1007/s00723-012-0344-7.

[62] R. Gitti, C. Wild, C. Tsiao, K. Zimmer, T.E. Glass, H.C. Dorn, Solid/liquid intermolecular transfer of dynamic nuclear polarization. enhanced flowing fluid proton NMR signals via immobilized spin labels, J. Am. Chem. Soc. 110 (7) (1988) 2294–2296, http://dx.doi.org/10.1021/ja00215a047.

[63] H.C. Dorn, J. Wang, L. Allen, D. Sweeney, T.E. Glass, Flow dynamic nuclear polarization, a novel method for enhancing NMR signals in flowing fluids, J. Magn. Reson. (1969) 79 (3) (1988) 404–412, http://dx.doi.org/10.1016/0022-2364(88)90078-9.

[64] H.C. Dorn, R. Gitti, K.H. Tsai, T.E. Glass, The flow transfer of a bolus with 1H dynamic nuclear polarization from low to high magnetic fields, Chem. Phys. Lett. 155 (2) (1989) 227–232, http://dx.doi.org/10.1016/0009-2614(89)85354-0.

[65] N. Bloembergen, On the interaction of nuclear spins in a crystalline lattice, Physica 15 (3) (1949) 386–426, http://dx.doi.org/10.1016/0031-8914(49)90114-7.

[66] G.R. Khutsishvili, Spin diffusion, magnetic relaxation, and dynamic polarization of nuclei, JETP 16 (6) (1963) 1540.

[67] A. Bornet, J. Milani, B. Vuichoud, A.J. Perez Linde, G. Bodenhausen, S. Jannin, Microwave frequency modulation to enhance dissolution dynamic nuclear polarization, Chem. Phys. Lett. 602 (2014) 63–67, http://dx.doi.org/10.1016/j.cplett.2014.04.013.

[68] S.J. Elliott, O. Cala, Q. Stern, S.F. Cousin, M. Ceillier, V. Decker, S. Jannin, Boosting dissolution-dynamic nuclear polarization by multiple-step dipolar order mediated 1H→13C cross-polarization, J. Magn. Reson. Open 8–9 (2021) 100018, http://dx.doi.org/10.1016/j.jmro.2021.100018.

[69] S.J. Elliott, Q. Stern, M. Ceillier, T. El Daraï, S.F. Cousin, O. Cala, S. Jannin, Practical dissolution dynamic nuclear polarization, Prog. Nucl. Magn. Reson. Spectrosc. 126–127 (2021) 59–100, http://dx.doi.org/10.1016/j.pnmrs.2021.04.002.

[70] A. Bornet, A. Pinon, A. Jhajharia, M. Baudin, X. Ji, L. Emsley, G. Bodenhausen, J.H. Ardenkjaer-Larsen, S. Jannin, Microwave-gated dynamic nuclear polarization, Phys. Chem. Chem. Phys. 18 (44) (2016) 30530–30535, http://dx.doi.org/10.1039/C6CP05587G.

[71] R. Shankar Palani, M. Mardini, Y. Quan, R.G. Griffin, Dynamic nuclear polarization with trityl radicals, J. Magn. Reson. 349 (2023) 107411, http://dx.doi.org/10.1016/j.jmr.2023.107411.

[72] A.W. Overhauser, Polarization of nuclei in metals, Phys. Rev. 92 (2) (1953) 411–415, http://dx.doi.org/10.1103/PhysRev.92.411.

[73] B. Corzilius, A.A. Smith, R.G. Griffin, Solid effect in magic angle spinning dynamic nuclear polarization, J. Chem. Phys. 137 (5) (2012) 054201, http://dx.doi.org/10.1063/1.4738761.

[74] M. Abraham, R.W. Kedzie, C.D. Jeffries, Gamma-ray anisotropy of Co^60 nuclei polarized by paramagnetic resonance saturation, Phys. Rev. 106 (1) (1957) 165–166, http://dx.doi.org/10.1103/PhysRev.106.165.

[75] C.F. Hwang, D.A. Hill, Phenomenological model for the new effect in dynamic polarization, Phys. Rev. Lett. 19 (18) (1967) 1011–1014, http://dx.doi.org/10.1103/PhysRevLett.19.1011.

[76] M. Borghini, Spin-temperature model of nuclear dynamic polarization using free radicals, Phys. Rev. Lett. 20 (9) (1968) 419–421, http://dx.doi.org/10.1103/PhysRevLett.20.419.

[77] W.T. Wenckebach, Dynamic nuclear polarization via the cross effect and thermal mixing: A. the role of triple spin flips, J. Magn. Reson. 299 (2019) 124–134, http://dx.doi.org/10.1016/j.jmr.2018.12.018.

[78] W.T. Wenckebach, Dynamic nuclear polarization via the cross effect and thermal mixing: B. Energy transport, J. Magn. Reson. 299 (2019) 151–167, http://dx.doi.org/10.1016/j.jmr.2018.12.020.

[79] K.R. Thurber, R. Tycko, Theory for cross effect dynamic nuclear polarization under magic-angle spinning in solid state nuclear magnetic resonance: the importance of level crossings, J. Chem. Phys. 137 (8) (2012) 084508, http://dx.doi.org/10.1063/1.4747449.

[80] T.V. Can, M.A. Caporini, F. Mentink-Vigier, B. Corzilius, J.J. Walish, M. Rosay, W.E. Maas, M. Baldus, S. Vega, T.M. Swager, R.G. Griffin, Overhauser effects in insulating solids, J. Chem. Phys. 141 (6) (2014) 064202, http://dx.doi.org/10.1063/1.4891866.

[81] A. Gurinov, B. Sieland, A. Kuzhelev, H. Elgabarty, T.D. Kühne, T. Prisner, J. Paradies, M. Baldus, K.L. Ivanov, S. Pylaeva, Mixed-valence compounds as polarizing agents for overhauser dynamic nuclear polarization in solids**, Angew. Chem. Int. Ed. 60 (28) (2021) 15371–15375, http://dx.doi.org/10.1002/anie.202103215.

[82] K.-N. Hu, H.-h. Yu, T.M. Swager, R.G. Griffin, Dynamic nuclear polarization with biradicals, J. Am. Chem. Soc. 126 (35) (2004) 10844–10845, http://dx.doi.org/10.1021/ja039749a.

[83] D.J. Kubicki, G. Casano, M. Schwarzwälder, S. Abel, C. Sauvée, K. Ganesan, M. Yulikov, A.J. Rossini, G. Jeschke, C. Copéret, A. Lesage, P. Tordo, O. Ouari, L. Emsley, Rational design of dinitroxide biradicals for efficient cross-effect dynamic nuclear polarization, Chem. Sci. 7 (1) (2015) 550–558, http://dx.doi.org/10.1039/C5SC02921J.

[84] J. Milani, B. Vuichoud, A. Bornet, P. Miéville, R. Mottier, S. Jannin, G. Bodenhausen, A magnetic tunnel to shelter hyperpolarized fluids, Rev. Sci. Instrum. 86 (2) (2015) 024101, http://dx.doi.org/10.1063/1.4908196.

[85] S.S. Tee, V. DiGialleonardo, R. Eskandari, S. Jeong, K.L. Granlund, A. Milousheva, A.J. Poot, S. Truong, J.A. Alvarez, H.N. Aldeborgh, K.R. Keshari, Sampling hyperpolarized molecules utilizing a 1 tesla permanent magnetic field, Sci. Rep. 6 (1) (2016) 32846, http://dx.doi.org/10.1038/srep32846.

[86] M. Ceillier, O. Cala, T. El Daraï, S.F. Cousin, Q. Stern, S. Guibert, S.J. Elliott, A. Bornet, B. Vuichoud, J. Milani, C. Pages, D. Eshchenko, J.G. Kempf, C. Jose, S.A. Lambert, S. Jannin, An automated system for fast transfer and injection of hyperpolarized solutions, J. Magn. Reson. Open 8–9 (2021) 100017, http://dx.doi.org/10.1016/j.jmro.2021.100017.

[87] T. El Daraï, S.F. Cousin, Q. Stern, M. Ceillier, J. Kempf, D. Eshchenko, R. Melzi, M. Schnell, L. Gremillard, A. Bornet, J. Milani, B. Vuichoud, O. Cala, D. Montarnal, S. Jannin, Porous functionalized polymers enable generating and transporting hyperpolarized mixtures of metabolites, Nature Commun. 12 (1) (2021) 4695, http://dx.doi.org/10.1038/s41467-021-24279-2.

[88] Q. Stern, Q. Reynard-Feytis, S.J. Elliott, M. Ceillier, O. Cala, K. Ivanov, S. Jannin, Rapid and simple 13C-hyperpolarization by 1H dissolution dynamic nuclear polarization followed by an inline magnetic field inversion, J. Am. Chem. Soc. 145 (50) (2023) 27576–27586, http://dx.doi.org/10.1021/jacs.3c09209.

[89] J.P. Peters, A. Brahms, V. Janicaud, M. Anikeeva, E. Peschke, F. Ellermann, A. Ferrari, D. Hellmold, J. Held-Feindt, N.-m. Kim, J. Meiser, K. Aden, R. Herges, J.-B. Hoevener, A.N. Pravdivtsev, Nitrogen-15 dynamic nuclear polarization of nicotinamide derivatives in biocompatible solutions, Sci. Adv. 9 (34) (2023) eadd3643, http://dx.doi.org/10.1126/sciadv.add3643.

[90] C.R. Bowers, D.P. Weitekamp, Transformation of symmetrization order to nuclear-spin magnetization by chemical reaction and nuclear magnetic resonance, Phys. Rev. Lett. 57 (21) (1986) 2645–2648, http://dx.doi.org/10.1103/PhysRevLett.57.2645.

[91] C.R. Bowers, D.P. Weitekamp, Parahydrogen and synthesis allow dramatically enhanced nuclear alignment, J. Am. Chem. Soc. 109 (18) (1987) 5541–5542, http://dx.doi.org/10.1021/ja00252a049.

[92] T.C. Eisenschmid, R.U. Kirss, P.P. Deutsch, S.I. Hommeltoft, R. Eisenberg, J. Bargon, R.G. Lawler, A.L. Balch, Para hydrogen induced polarization in hydrogenation reactions, J. Am. Chem. Soc. 109 (26) (1987) 8089–8091, http://dx.doi.org/10.1021/ja00260a026.

[93] S.I. Hommeltoft, D.H. Berry, R. Eisenberg, Metal-centered radical-pair mechanism for alkyne hydrogenation with a binuclear rhodium hydride complex. CIDNP without organic radicals, J. Am. Chem. Soc. 108 (17) (1986) 5345–5347, http://dx.doi.org/10.1021/ja00277a050.

[94] J. Natterer, J. Bargon, Parahydrogen induced polarization, Prog. Nucl. Magn. Reson. Spectrosc. 31 (4) (1997) 293–315, http://dx.doi.org/10.1016/S0079-6565(97)00007-1.

[95] S.B. Duckett, R.E. Mewis, Application of parahydrogen induced polarization techniques in NMR spectroscopy and imaging, Acc. Chem. Res. 45 (8) (2012) 1247–1257, http://dx.doi.org/10.1021/ar2003094.

[96] J.-B. Hövener, A.N. Pravdivtsev, B. Kidd, C.R. Bowers, S. Glöggler, K.V. Kovtunov, M. Plaumann, R. Katz-Brull, K. Buckenmaier, A. Jerschow, T. Theis, R.V. Shchepin, R. Wagner, P. Bhattacharya, N.M. Zacharias, E.Y. Chekmenev, Parahydrogen-based hyperpolarization for biomedicine, Angew. Chem. Int. Ed. 57 (35) (2018) 11140–11162, http://dx.doi.org/10.1002/anie.201711842.

[97] P. Bhattacharya, K. Harris, A.P. Lin, M. Mansson, V.A. Norton, W.H. Perman, D.P. Weitekamp, B.D. Ross, Ultra-fast three dimensional imaging of hyperpolarized 13C in vivo, Magn. Reson. Mater. Phys. Biol. Med. 18 (5) (2005) 245–256, http://dx.doi.org/10.1007/s10334-005-0007-x.

[98] F. Reineri, T. Boi, S. Aime, ParaHydrogen induced polarization of 13C carboxylate resonance in acetate and pyruvate, Nature Commun. 6 (1) (2015) 5858, http://dx.doi.org/10.1038/ncomms6858.

[99] A.M. Coffey, R.V. Shchepin, M.L. Truong, K. Wilkens, W. Pham, E.Y. Chekmenev, Open-source automated parahydrogen hyperpolarizer for molecular imaging using ¹³C metabolic contrast agents, Anal. Chem. 88 (16) (2016) 8279–8288, http://dx.doi.org/10.1021/acs.analchem.6b02130.

[100] E. Cavallari, C. Carrera, M. Sorge, G. Bonne, A. Muchir, S. Aime, F. Reineri, The 13C hyperpolarized pyruvate generated by ParaHydrogen detects the response of the heart to altered metabolism in real time, Sci. Rep. 8 (1) (2018) 8366, http://dx.doi.org/10.1038/s41598-018-26583-2.

[101] A.B. Schmidt, S. Berner, M. Braig, M. Zimmermann, J. Hennig, D. Von Elverfeldt, J.-B. Hövener, In vivo 13C-MRI using SAMBADENA, in: D. Hinderberger (Ed.), PLoS One 13 (7) (2018) e0200141, http://dx.doi.org/10.1371/journal.pone.0200141.

[102] S. Knecht, J.W. Blanchard, D. Barskiy, E. Cavallari, L. Dagys, E. Van Dyke, M. Tsukanov, B. Bliemel, K. Münnemann, S. Aime, F. Reineri, M.H. Levitt, G. Buntkowsky, A. Pines, P. Blümler, D. Budker, J. Eills, Rapid hyperpolarization and purification of the metabolite fumarate in aqueous solution, Proc. Natl. Acad. Sci. 118 (13) (2021) e2025383118, http://dx.doi.org/10.1073/pnas.2025383118.

[103] R.W. Adams, J.A. Aguilar, K.D. Atkinson, M.J. Cowley, P.I.P. Elliott, S.B. Duckett, G.G.R. Green, I.G. Khazal, J. López-Serrano, D.C. Williamson, Reversible interactions with para-hydrogen enhance NMR sensitivity by polarization transfer, Science 323 (5922) (2009) 1708–1711, http://dx.doi.org/10.1126/science.1168877.

[104] J.W. Leachman, R.T. Jacobsen, S.G. Penoncello, E.W. Lemmon, Fundamental equations of state for parahydrogen, normal hydrogen, and orthohydrogen, J. Phys. Chem. Ref. Data 38 (3) (2009) 721–748, http://dx.doi.org/10.1063/1.3160306.

[105] W. Pauli, The connection between spin and statistics, Phys. Rev. 58 (8) (1940) 716–722, http://dx.doi.org/10.1103/PhysRev.58.716.

[106] H.J. Bernstein, J.A. Pople, W.G. Schneider, The analysis of nuclear magnetic resonance spectra: I. Systems of two and three nuclei, Can. J. Chem. 35 (1) (1957) 67–83, http://dx.doi.org/10.1139/v57-011.

[107] J.A. Pople, W.G. Schneider, H.J. Bernstein, The analysis of nuclear magnetic resonance spectra: II. Two pairs of two equivalent nuclei, Can. J. Chem. 35 (9) (1957) 1060–1072, http://dx.doi.org/10.1139/v57-143.

[108] A. Gamliel, H. Allouche-Arnon, R. Nalbandian, C.M. Barzilay, J.M. Gomori, R. Katz-Brull, An apparatus for production of isotopically and spin-enriched hydrogen for induced polarization studies, Appl. Magn. Reson. 39 (4) (2010) 329–345, http://dx.doi.org/10.1007/s00723-010-0161-9.

[109] M. Matsumoto, J.H. Espenson, Kinetics of the interconversion of parahydrogen and orthohydrogen catalyzed by paramagnetic complex ions, J. Am. Chem. Soc. 127 (32) (2005) 11447–11453, http://dx.doi.org/10.1021/ja0524292.

[110] C. Aroulanda, L. Starovoytova, D. Canet, Longitudinal nuclear spin relaxation of ortho- and para-hydrogen dissolved in organic solvents, J. Phys. Chem. A 111 (42) (2007) 10615–10624, http://dx.doi.org/10.1021/jp073162r.

[111] L. Buljubasich, M.B. Franzoni, K. Münnemann, Parahydrogen induced polarization by homogeneous catalysis: Theory and applications, in: L.T. Kuhn (Ed.), Hyperpolarization Methods in NMR Spectroscopy, in: Topics in Current Chemistry, Springer, Berlin, Heidelberg, 2013, pp. 33–74.

[112] F. Ellermann, A. Pravdivtsev, J.-B. Hövener, Open-source, partially 3D-printed, high-pressure (50-bar) liquid-nitrogen-cooled parahydrogen generator, Magn. Reson. 2 (1) (2021) 49–62, http://dx.doi.org/10.5194/mr-2-49-2021.

[113] B. Chapman, B. Joalland, C. Meersman, J. Ettedgui, R.E. Swenson, M.C. Krishna, P. Nikolaou, K.V. Kovtunov, O.G. Salnikov, I.V. Koptyug, M.E. Gemeinhardt, B.M. Goodson, R.V. Shchepin, E.Y. Chekmenev, Low-cost high-pressure clinical-scale 50% parahydrogen generator using liquid nitrogen at 77 K, Anal. Chem. 93 (24) (2021) 8476–8483, http://dx.doi.org/10.1021/acs.analchem.1c00716.

[114] J.R. Birchall, A.M. Coffey, B.M. Goodson, E.Y. Chekmenev, High-pressure clinical-scale 87% parahydrogen generator, Anal. Chem. 92 (23) (2020) 15280–15284, http://dx.doi.org/10.1021/acs.analchem.0c03358.

[115] S. Nantogma, B. Joalland, K. Wilkens, E.Y. Chekmenev, Clinical-scale production of nearly pure (>98.5%) parahydrogen and quantification by benchtop NMR spectroscopy, Anal. Chem. 93 (7) (2021) 3594–3601, http://dx.doi.org/10.1021/acs.analchem.0c05129.

[116] J.-B. Hoevener, S. Baer, J. Leupold, K. Jenne, D. Leibfritz, J. Hennig, S.B. Duckett, D. von Elverfeldt, A continuous-flow, high-throughput, high-pressure parahydrogen converter for hyperpolarization in a clinical setting, NMR Biomed. 26 (2) (2013) 124–131, http://dx.doi.org/10.1002/nbm.2827.

[117] B. Feng, A.M. Coffey, R.D. Colon, E.Y. Chekmenev, K.W. Waddell, A pulsed injection parahydrogen generator and techniques for quantifying enrichment, J. Magn. Reson. 214 (2012) 258–262, http://dx.doi.org/10.1016/j.jmr.2011.11.015.

[118] P.M. Richardson, R.O. John, A.J. Parrott, P.J. Rayner, W. Iali, A. Nordon, M.E. Halse, S.B. Duckett, Quantification of hyperpolarisation efficiency in SABRE and SABRE-relay enhanced NMR spectroscopy, Phys. Chem. Chem. Phys. 20 (41) (2018) 26362–26371, http://dx.doi.org/10.1039/C8CP05473H.

[119] M.G. Pravica, D.P. Weitekamp, Net NMR alignment by adiabatic transport of parahydrogen addition products to high magnetic field, Chem. Phys. Lett. 145 (4) (1988) 255–258, http://dx.doi.org/10.1016/0009-2614(88)80002-2.

[120] E. Cavallari, C. Carrera, T. Boi, S. Aime, F. Reineri, Effects of magnetic field cycle on the polarization transfer from parahydrogen to heteronuclei through long-range J-couplings, J. Phys. Chem. B 119 (31) (2015) 10035–10041, http://dx.doi.org/10.1021/acs.jpcb.5b06222.

[121] Y. Ding, S. Korchak, S. Mamone, A.P. Jagtap, G. Stevanato, S. Sternkopf, D. Moll, H. Schroeder, S. Becker, A. Fischer, E. Gerhardt, T.F. Outeiro, F. Opazo, C. Griesinger, S. Glöggler, Rapidly signal-enhanced metabolites for atomic scale monitoring of living cells with magnetic resonance, Chemistry–Methods 2 (7) (2022) e202200023, http://dx.doi.org/10.1002/cmtd.202200023.

[122] S. Korchak, S. Yang, S. Mamone, S. Glöggler, Pulsed magnetic resonance to signal-enhance metabolites within seconds by utilizing parahydrogen, ChemistryOpen 7 (5) (2018) 344–348, http://dx.doi.org/10.1002/open.201800024.

[123] T. Hune, S. Mamone, H. Schroeder, A.P. Jagtap, S. Sternkopf, G. Stevanato, S. Korchak, C. Fokken, C.A. Müller, A.B. Schmidt, D. Becker, S. Glöggler, Metabolic tumor imaging with rapidly signal-enhanced 1-13C-pyruvate-d3, ChemPhysChem n/a (n/a) (2023) e202200615, http://dx.doi.org/10.1002/cphc.202200615.

[124] K. Them, F. Ellermann, A.N. Pravdivtsev, O.G. Salnikov, I.V. Skovpin, I.V. Koptyug, R. Herges, J.-B. Hövener, Parahydrogen-induced polarization relayed via proton exchange, J. Am. Chem. Soc. 143 (34) (2021) 13694–13700, http://dx.doi.org/10.1021/jacs.1c05254.

[125] S. Alcicek, E. Van Dyke, J. Xu, S. Pustelny, D.A. Barskiy, 13C and 15N benchtop NMR detection of metabolites via relayed hyperpolarization**, Chemistry–Methods n/a (n/a) (2023) e202200075, http://dx.doi.org/10.1002/cmtd.202200075.

[126] W. Iali, P.J. Rayner, S.B. Duckett, Using parahydrogen to hyperpolarize amines, amides, carboxylic acids, alcohols, phosphates, and carbonates, Sci. Adv. 4 (1) (2018) eaao6250, http://dx.doi.org/10.1126/sciadv.aao6250.

[127] M.J. Cowley, R.W. Adams, K.D. Atkinson, M.C.R. Cockett, S.B. Duckett, G.G.R. Green, J.A.B. Lohman, R. Kerssebaum, D. Kilgour, R.E. Mewis, Iridium N-heterocyclic carbene complexes as efficient catalysts for magnetization transfer from para-hydrogen, J. Am. Chem. Soc. 133 (16) (2011) 6134–6137, http://dx.doi.org/10.1021/ja200299u.

[128] P.J. Rayner, P. Norcott, K.M. Appleby, W. Iali, R.O. John, S.J. Hart, A.C. Whitwood, S.B. Duckett, Fine-tuning the efficiency of para-hydrogen-induced hyperpolarization by rational N-heterocyclic carbene design, Nature Commun. 9 (1) (2018) 4251, http://dx.doi.org/10.1038/s41467-018-06766-1.

[129] K.D. Atkinson, M.J. Cowley, S.B. Duckett, P.I.P. Elliott, G.G.R. Green, J. López-Serrano, I.G. Khazal, A.C. Whitwood, Para-hydrogen induced polarization without incorporation of para-hydrogen into the analyte, Inorg. Chem. 48 (2) (2009) 663–670, http://dx.doi.org/10.1021/ic8020029.

[130] T. Theis, M.L. Truong, A.M. Coffey, R.V. Shchepin, K.W. Waddell, F. Shi, B.M. Goodson, W.S. Warren, E.Y. Chekmenev, Microtesla SABRE enables 10% nitrogen-15 nuclear spin polarization, J. Am. Chem. Soc. 137 (4) (2015) 1404–1407, http://dx.doi.org/10.1021/ja512242d.

[131] V. Daniele, F.-X. Legrand, P. Berthault, J.-N. Dumez, G. Huber, Single-scan multidimensional NMR analysis of mixtures at sub-millimolar concentrations by using SABRE hyperpolarization, ChemPhysChem 16 (16) (2015) 3413–3417, http://dx.doi.org/10.1002/cphc.201500535.

[132] N.V. Chukanov, O.G. Salnikov, R.V. Shchepin, A. Svyatova, K.V. Kovtunov, I.V. Koptyug, E.Y. Chekmenev, 19F hyperpolarization of 15N-3-19F-pyridine via signal amplification by reversible exchange, J. Phys. Chem. C 122 (40) (2018) 23002–23010, http://dx.doi.org/10.1021/acs.jpcc.8b06654.

[133] K.M. Appleby, R.E. Mewis, A.M. Olaru, G.G.R. Green, I.J.S. Fairlamb, S.B. Duckett, Investigating pyridazine and phthalazine exchange in a series of iridium complexes in order to define their role in the catalytic transfer of magnetisation from para-hydrogen, Chem. Sci. 6 (7) (2015) 3981–3993, http://dx.doi.org/10.1039/C5SC00756A.

[134] S. Glöggler, M. Emondts, J. Colell, R. Müller, B. Blümich, S. Appelt, Selective drug trace detection with low-field NMR, Analyst 136 (8) (2011) 1566, http://dx.doi.org/10.1039/c0an01048k.

[135] J.-B. Hövener, N. Schwaderlapp, T. Lickert, S.B. Duckett, R.E. Mewis, L.A.R. Highton, S.M. Kenny, G.G.R. Green, D. Leibfritz, J.G. Korvink, J. Hennig, D. von Elverfeldt, A hyperpolarized equilibrium for magnetic resonance, Nature Commun. 4 (1) (2013) 2946, http://dx.doi.org/10.1038/ncomms3946.

[136] J.F.P. Colell, A.W.J. Logan, Z. Zhou, R.V. Shchepin, D.A. Barskiy, G.X. Ortiz, Q. Wang, S.J. Malcolmson, E.Y. Chekmenev, W.S. Warren, T. Theis, Generalizing, extending, and maximizing nitrogen-15 hyperpolarization induced by parahydrogen in reversible exchange, J. Phys. Chem. C 121 (12) (2017) 6626–6634, http://dx.doi.org/10.1021/acs.jpcc.6b12097.

[137] E.B. Dücker, L.T. Kuhn, K. Münnemann, C. Griesinger, Similarity of SABRE field dependence in chemically different substrates, J. Magn. Reson. 214 (2012) 159–165, http://dx.doi.org/10.1016/j.jmr.2011.11.001.

[138] M. Fekete, P.J. Rayner, G.G.R. Green, S.B. Duckett, Harnessing polarisation transfer to indazole and imidazole through signal amplification by reversible exchange to improve their NMR detectability, Magn. Reson. Chem. 55 (10) (2017) 944–957, http://dx.doi.org/10.1002/mrc.4607.

[139] M. Fekete, O. Bayfield, S.B. Duckett, S. Hart, R.E. Mewis, N. Pridmore, P.J. Rayner, A. Whitwood, Iridium(III) hydrido N-heterocyclic carbene–phosphine complexes as catalysts in magnetization transfer reactions, Inorg. Chem. 52 (23) (2013) 13453–13461, http://dx.doi.org/10.1021/ic401783c.

[140] R.E. Mewis, R.A. Green, M.C.R. Cockett, M.J. Cowley, S.B. Duckett, G.G.R. Green, R.O. John, P.J. Rayner, D.C. Williamson, Strategies for the hyperpolarization of acetonitrile and related ligands by SABRE, J. Phys. Chem. B 119 (4) (2015) 1416–1424, http://dx.doi.org/10.1021/jp511492q.

[141] K. MacCulloch, A. Browning, P. TomHon, S. Lehmkuhl, E.Y. Chekmenev, T. Theis, Parahydrogen in reversible exchange induces long-lived 15N hyperpolarization of anticancer drugs anastrozole and letrozole, Anal. Chem. 95 (20) (2023) 7822–7829, http://dx.doi.org/10.1021/acs.analchem.2c04817.

[142] A.W.J. Logan, T. Theis, J.F.P. Colell, W.S. Warren, S.J. Malcolmson, Hyperpolarization of nitrogen-15 schiff bases by reversible exchange catalysis with para-hydrogen, Chemistry – Eur. J. 22 (31) (2016) 10777–10781, http://dx.doi.org/10.1002/chem.201602393.

[143] P.J. Rayner, M. Fekete, C.A. Gater, F. Ahwal, N. Turner, A.J. Kennerley, S.B. Duckett, Real-time high-sensitivity reaction monitoring of important nitrogen-cycle synthons by 15N hyperpolarized nuclear magnetic resonance, J. Am. Chem. Soc. 144 (19) (2022) 8756–8769, http://dx.doi.org/10.1021/jacs.2c02619.

[144] S. Glöggler, R. Müller, J. Colell, M. Emondts, M. Dabrowski, B. Blümich, S. Appelt, Para-hydrogen induced polarization of amino acids, peptides and deuterium–hydrogen gas, Phys. Chem. Chem. Phys. 13 (30) (2011) 13759–13764, http://dx.doi.org/10.1039/C1CP20992B.

[145] L. Dreisewerd, R.L.E.G. Aspers, M.C. Feiters, F.P.J.T. Rutjes, M. Tessari, NMR discrimination of d- and l-alpha-amino acids at submicromolar concentration via parahydrogen-induced hyperpolarization, J. Am. Chem. Soc. 145 (3) (2023) 1518–1523, http://dx.doi.org/10.1021/jacs.2c11285.

[146] E. Vaneeckhaute, J.-M. Tyburn, J.G. Kempf, J.A. Martens, E. Breynaert, Reversible parahydrogen induced hyperpolarization of 15N in unmodified amino acids unraveled at high magnetic field, Adv. Sci. 10 (23) (2023) 2207112, http://dx.doi.org/10.1002/advs.202207112.

[147] R.V. Shchepin, D.A. Barskiy, A.M. Coffey, B.M. Goodson, E.Y. Chekmenev, NMR signal amplification by reversible exchange of sulfur-heterocyclic compounds found in petroleum, ChemistrySelect 1 (10) (2016) 2552–2555, http://dx.doi.org/10.1002/slct.201600761.

[148] V.V. Zhivonitko, I.V. Skovpin, I.V. Koptyug, Strong 31P nuclear spin hyperpolarization produced via reversible chemical interaction with parahydrogen, Chem. Commun. 51 (13) (2015) 2506–2509, http://dx.doi.org/10.1039/C4CC08115C.

[149] D.A. Barskiy, S. Knecht, A.V. Yurkovskaya, K.L. Ivanov, SABRE: Chemical kinetics and spin dynamics of the formation of hyperpolarization, Prog. Nucl. Magn. Reson. Spectrosc. 114–115 (2019) 33–70, http://dx.doi.org/10.1016/j.pnmrs.2019.05.005.

[150] R.A. Green, R.W. Adams, S.B. Duckett, R.E. Mewis, D.C. Williamson, G.G.R. Green, The theory and practice of hyperpolarization in magnetic resonance using parahydrogen, Prog. Nucl. Magn. Reson. Spectrosc. 67 (2012) 1–48, http://dx.doi.org/10.1016/j.pnmrs.2012.03.001.

[151] R.W. Adams, S.B. Duckett, R.A. Green, D.C. Williamson, G.G.R. Green, A theoretical basis for spontaneous polarization transfer in non-hydrogenative parahydrogen-induced polarization, J. Chem. Phys. 131 (19) (2009) 194505, http://dx.doi.org/10.1063/1.3254386.

[152] K.L. Ivanov, A.N. Pravdivtsev, A.V. Yurkovskaya, H.-M. Vieth, R. Kaptein, The role of level anti-crossings in nuclear spin hyperpolarization, Prog. Nucl. Magn. Reson. Spectrosc. 81 (2014) 1–36, http://dx.doi.org/10.1016/j.pnmrs.2014.06.001.

[153] A.N. Pravdivtsev, K.L. Ivanov, A.V. Yurkovskaya, P.A. Petrov, H.-H. Limbach, R. Kaptein, H.-M. Vieth, Spin polarization transfer mechanisms of SABRE: A magnetic field dependent study, J. Magn. Reson. 261 (2015) 73–82, http://dx.doi.org/10.1016/j.jmr.2015.10.006.

[154] A.N. Pravdivtsev, A.V. Yurkovskaya, H.-M. Vieth, K.L. Ivanov, R. Kaptein, Level anti-crossings are a key factor for understanding para-hydrogen-induced hyperpolarization in SABRE experiments, ChemPhysChem 14 (14) (2013) 3327–3331, http://dx.doi.org/10.1002/cphc.201300595.

[155] M. Fekete, F. Ahwal, S.B. Duckett, Remarkable levels of 15N polarization delivered through SABRE into unlabeled pyridine, pyrazine, or metronidazole enable single scan NMR quantification at the mM level, J. Phys. Chem. B 124 (22) (2020) 4573–4580, http://dx.doi.org/10.1021/acs.jpcb.0c02583.

[156] P.M. Richardson, A.J. Parrott, O. Semenova, A. Nordon, S.B. Duckett, M.E. Halse, SABRE hyperpolarization enables high-sensitivity ^{1}H and ^{13}C benchtop NMR spectroscopy, Analyst 143 (14) (2018) 3442–3450, http://dx.doi.org/10.1039/C8AN00596F.

[157] R.V. Shchepin, B.M. Goodson, T. Theis, W.S. Warren, E.Y. Chekmenev, Toward hyperpolarized ^{19}F molecular imaging via reversible exchange with parahydrogen, ChemPhysChem 18 (15) (2017) 1961–1965, http://dx.doi.org/10.1002/cphc.201700594.

[158] D.A. Barskiy, R.V. Shchepin, C.P.N. Tanner, J.F.P. Colell, B.M. Goodson, T. Theis, W.S. Warren, E.Y. Chekmenev, The absence of quadrupolar nuclei facilitates efficient 13C hyperpolarization via reversible exchange with parahydrogen, ChemPhysChem 18 (12) (2017) 1493–1498, http://dx.doi.org/10.1002/cphc.201700416.

[159] J.R. Lindale, S.L. Eriksson, C.P.N. Tanner, Z. Zhou, J.F.P. Colell, G. Zhang, J. Bae, E.Y. Chekmenev, T. Theis, W.S. Warren, Unveiling coherently driven hyperpolarization dynamics in signal amplification by reversible exchange, Nature Commun. 10 (1) (2019) 395, http://dx.doi.org/10.1038/s41467-019-08298-8.

[160] X. Li, J.R. Lindale, S.L. Eriksson, W.S. Warren, SABRE enhancement with oscillating pulse sequences, Phys. Chem. Chem. Phys. 24 (27) (2022) 16462–16470, http://dx.doi.org/10.1039/D2CP00899H.

[161] T. Theis, M. Truong, A.M. Coffey, E.Y. Chekmenev, W.S. Warren, LIGHT-SABRE enables efficient in-magnet catalytic hyperpolarization, J. Magn. Reson. 248 (2014) 23–26, http://dx.doi.org/10.1016/j.jmr.2014.09.005.

[162] A.N. Pravdivtsev, A.V. Yurkovskaya, H.-M. Vieth, K.L. Ivanov, RF-SABRE: A way to continuous spin hyperpolarization at high magnetic fields, J. Phys. Chem. B 119 (43) (2015) 13619–13629, http://dx.doi.org/10.1021/acs.jpcb.5b03032.

[163] S. Knecht, A.S. Kiryutin, A.V. Yurkovskaya, K.L. Ivanov, Efficient conversion of anti-phase spin order of protons into ^{15}N magnetisation using SLIC-SABRE, Mol. Phys. 117 (19) (2019) 2762–2771, http://dx.doi.org/10.1080/00268976.2018.1515999.

[164] S.S. Roy, G. Stevanato, P.J. Rayner, S.B. Duckett, Direct enhancement of nitrogen-15 targets at high-field by fast ADAPT-SABRE, J. Magn. Reson. 285 (2017) 55–60, http://dx.doi.org/10.1016/j.jmr.2017.10.006.

[165] A.N. Pravdivtsev, A.V. Yurkovskaya, H. Zimmermann, H.-M. Vieth, K.L. Ivanov, Enhancing NMR of insensitive nuclei by transfer of SABRE spin hyperpolarization, Chem. Phys. Lett. 661 (2016) 77–82, http://dx.doi.org/10.1016/j.cplett.2016.08.037.

[166] E.V. Stanbury, P.M. Richardson, S.B. Duckett, Understanding substrate substituent effects to improve catalytic efficiency in the SABRE hyperpolarisation process, Catal. Sci. Technol. 9 (15) (2019) 3914–3922, http://dx.doi.org/10.1039/C9CY00396G.

[167] D.A. Barskiy, A.N. Pravdivtsev, K.L. Ivanov, K.V. Kovtunov, I.V. Koptyug, A simple analytical model for signal amplification by reversible exchange (SABRE) process, Phys. Chem. Chem. Phys. 18 (1) (2015) 89–93, http://dx.doi.org/10.1039/C5CP05134G.

[168] B.J. Tickner, O. Semenova, W. Iali, P.J. Rayner, A.C. Whitwood, S.B. Duckett, Optimisation of pyruvate hyperpolarisation using SABRE by tuning the active magnetisation transfer catalyst, Catal. Sci. Technol. 10 (5) (2020) 1343–1355, http://dx.doi.org/10.1039/C9CY02498K.

[169] B. J. Tickner, Y. Borozdina, S. B. Duckett, G. Angelovski, Exploring the hyperpolarisation of EGTA-based ligands using SABRE, Dalton Trans. 50 (7) (2021) 2448–2461, http://dx.doi.org/10.1039/D0DT03839C.

[170] P.J. Rayner, J.P. Gillions, V.D. Hannibal, R.O. John, S.B. Duckett, Hyperpolarisation of weakly binding N-heterocycles using signal amplification by reversible exchange, Chem. Sci. 12 (16) (2021) 5910–5917, http://dx.doi.org/10.1039/D0SC06907H.

[171] A.M. Olaru, T.B.R. Robertson, J.S. Lewis, A. Antony, W. Iali, R.E. Mewis, S.B. Duckett, Extending the scope of ^{19}F hyperpolarization through signal amplification by reversible exchange in MRI and NMR spectroscopy, ChemistryOpen 7 (1) (2018) 97–105, http://dx.doi.org/10.1002/open.201700166.

[172] W. Iali, S.S. Roy, B.J. Tickner, F. Ahwal, A.J. Kennerley, S.B. Duckett, Hyperpolarising pyruvate through signal amplification by reversible exchange (SABRE), Angew. Chem. Int. Ed. 58 (30) (2019) 10271–10275, http://dx.doi.org/10.1002/anie.201905483.

[173] H. de Maissin, P.R. Groß, O. Mohiuddin, M. Weigt, L. Nagel, M. Herzog, Z. Wang, R. Willing, W. Reichardt, M. Pichotka, L. Heß, T. Reinheckel, H.J. Jessen, R. Zeiser, M. Bock, D. von Elverfeldt, M. Zaitsev, S. Korchak, S. Glöggler, J.-B. Hövener, E.Y. Chekmenev, F. Schilling, S. Knecht, A.B. Schmidt, In vivo metabolic imaging of [1-13C]pyruvate-d3 hyperpolarized by reversible exchange with parahydrogen**, Angew. Chem. Int. Ed. 62 (36) (2023) e202306654, http://dx.doi.org/10.1002/anie.202306654.

[174] N. Eshuis, N. Hermkens, B.J.A. van Weerdenburg, M.C. Feiters, F.P.J.T. Rutjes, S.S. Wijmenga, M. Tessari, Toward nanomolar detection by NMR through SABRE hyperpolarization, J. Am. Chem. Soc. 136 (7) (2014) 2695–2698, http://dx.doi.org/10.1021/ja412994k.

[175] N. Eshuis, B.J.A. vanWeerdenburg, M.C. Feiters, F.P.J.T. Rutjes, S.S. Wijmenga, M. Tessari, Quantitative trace analysis of complex mixtures using SABRE hyperpolarization, Angew. Chem., Int. Ed. 54 (5) (2015) 1481–1484, http://dx.doi.org/10.1002/anie.201409795.

[176] W. Iali, P.J. Rayner, A. Alshehri, A.J. Holmes, A.J. Ruddlesden, S.B. Duckett, Direct and indirect hyperpolarisation of amines using *para* hydrogen, Chem. Sci. 9 (15) (2018) 3677–3684, http://dx.doi.org/10.1039/C8SC00526E.

[177] P.M. Richardson, S. Jackson, A.J. Parrott, A. Nordon, S.B. Duckett, M.E. Halse, A simple hand-held magnet array for efficient and reproducible SABRE hyperpolarisation using manual sample shaking, Magn. Reson. Chem. 56 (7) (2018) 641–650, http://dx.doi.org/10.1002/mrc.4687.

[178] T.B.R. Robertson, L.H. Antonides, N. Gilbert, S.L. Benjamin, S.K. Langley, L.J. Munro, O.B. Sutcliffe, R.E. Mewis, Hyperpolarization of pyridyl fentalogues by signal amplification by reversible exchange (SABRE), ChemistryOpen 8 (12) (2019) 1375–1382, http://dx.doi.org/10.1002/open.201900273.

[179] M.E. Halse, Perspectives for hyperpolarisation in compact NMR, TRAC Trends Anal. Chem. 83 (2016) 76–83, http://dx.doi.org/10.1016/j.trac.2016.05.004.

[180] P. M. Richardson, W. Iali, S. S. Roy, P. J. Rayner, M. E. Halse, S. B. Duckett, Rapid 13 C NMR hyperpolarization delivered from para -hydrogen enables the low concentration detection and quantification of sugars, Chem. Sci. 10 (45) (2019) 10607–10619, http://dx.doi.org/10.1039/C9SC03450A.

[181] T. Tennant, M. Hulme, T. Robertson, O. Sutcliffe, R. Mewis, Benchtop NMR analysis of piperazine-based drugs hyperpolarised by SABRE, Magn. Reson. Chem. 58 (12) (2020) 1151–1159, http://dx.doi.org/10.1002/mrc.4999.

[182] T.B.R. Robertson, N. Gilbert, O.B. Sutcliffe, R.E. Mewis, Hyperpolarisation of mirfentanil by SABRE in the presence of heroin, Chemphyschem 22 (11) (2021) 1059–1064, http://dx.doi.org/10.1002/cphc.202100165.

[183] O. Semenova, P.M. Richardson, A.J. Parrott, A. Nordon, M.E. Halse, S.B. Duckett, Reaction monitoring using SABRE-hyperpolarized benchtop (1 T) NMR spectroscopy, Anal. Chem. 91 (10) (2019) 6695–6701, http://dx.doi.org/10.1021/acs.analchem.9b00729.

[184] A.D. Robinson, F. Hill-Casey, S.B. Duckett, M.E. Halse, Quantitative reaction monitoring using parahydrogen-enhanced benchtop NMR spectroscopy, Phys. Chem. Chem. Phys. 26 (19) (2024) 14317–14328, http://dx.doi.org/10.1039/D3CP06221J.

[185] A.N. Pravdivtsev, A. Brahms, F. Ellermann, T. Stamp, R. Herges, J.-B. Hövener, Parahydrogen-induced polarization and spin order transfer in ethyl pyruvate at high magnetic fields, Sci. Rep. 12 (1) (2022) 19361, http://dx.doi.org/10.1038/s41598-022-22347-1.

[186] C. Nelson, A.B. Schmidt, I. Adelabu, S. Nantogma, V.G. Kiselev, A. Abdurraheem, H. de Maissin, S. Lehmkuhl, S. Appelt, T. Theis, E.Y. Chekmenev, Parahydrogen-induced carbon-13 radiofrequency amplification by stimulated emission of radiation, Angew. Chem. 135 (5) (2023) e202215678, http://dx.doi.org/10.1002/ange.202215678.

[187] A. Duchowny, J. Denninger, L. Lohmann, T. Theis, S. Lehmkuhl, A. Adams, SABRE hyperpolarization with up to 200 bar parahydrogen in standard and quickly removable solvents, Int. J. Mol. Sci. 24 (3) (2023) 2465, http://dx.doi.org/10.3390/ijms24032465.

[188] P.L. Norcott, Benzoquinone enhances hyperpolarization of surface alcohols with para-hydrogen, J. Am. Chem. Soc. 145 (18) (2023) 9970–9975, http://dx.doi.org/10.1021/jacs.3c01593.

[189] K. Jeong, S. Min, H. Chae, S.K. Namgoong, Detecting low concentrations of unsaturated C—C bonds by parahydrogen-induced polarization using an efficient home-built parahydrogen generator, Magn. Reson. Chem. 56 (11) (2018) 1089–1093, http://dx.doi.org/10.1002/mrc.4756.

[190] K.H. Kim, J.W. Choi, C.S. Kim, K. Jeong, Parahydrogen-induced polarization in the hydrogenation of lignin-derived phenols using Wilkinson's catalyst, Fuel 255 (2019) 115845, http://dx.doi.org/10.1016/j.fuel.2019.115845.

[191] H.J. Jeong, S. Min, K. Jeong, Analysis of 1-aminoisoquinoline using the signal amplification by reversible exchange hyperpolarization technique, Analyst 145 (20) (2020) 6478–6484, http://dx.doi.org/10.1039/D0AN00967A.

[192] K. MacCulloch, P. Tomhon, A. Browning, E. Akeroyd, S. Lehmkuhl, E.Y. Chekmenev, T. Theis, Hyperpolarization of common antifungal agents with SABRE, Magn. Reson. Chem. 59 (12) (2021) 1225–1235, http://dx.doi.org/10.1002/mrc.5187.

[193] O.G. Salnikov, N.V. Chukanov, A. Svyatova, I.A. Trofimov, M.S.H. Kabir, J.G. Gelovani, K.V. Kovtunov, I.V. Koptyug, E.Y. Chekmenev, 15 N NMR hyperpolarization of radiosensitizing antibiotic nimorazole by reversible parahydrogen exchange in microtesla magnetic fields, Angew. Chem., Int. Ed. Engl. 60 (5) (2021) 2406–2413, http://dx.doi.org/10.1002/anie.202011698.

[194] A.B. Schmidt, J. Eills, L. Dagys, M. Gierse, M. Keim, S. Lucas, M. Bock, I. Schwartz, M. Zaitsev, E.Y. Chekmenev, S. Knecht, Over 20% carbon-13 polarization of perdeuterated pyruvate using reversible exchange with parahydrogen and spin-lock induced crossing at 50 microt, J. Phys. Chem. Lett. 14 (23) (2023) 5305–5309, http://dx.doi.org/10.1021/acs.jpclett.3c00707.

[195] I. Adelabu, M.R.H. Chowdhury, S. Nantogma, C. Oladun, F. Ahmed, L. Stilgenbauer, M. Sadagurski, T. Theis, B.M. Goodson, E.Y. Chekmenev, Efficient SABRE-SHEATH hyperpolarization of potent branched-chain-amino-acid metabolic probe [1-13C]ketoisocaproate, Metabolites 13 (2) (2023) 200, http://dx.doi.org/10.3390/metabo13020200.

[196] H. Chae, S. Min, H.J. Jeong, S.K. Namgoong, S. Oh, K. Kim, K. Jeong, Organic reaction monitoring of a glycine derivative using signal amplification by reversible exchange-hyperpolarized benchtop nuclear magnetic resonance spectroscopy, Anal. Chem. 92 (16) (2020) 10902–10907, http://dx.doi.org/10.1021/acs.analchem.0c01270.

[197] H.J. Jeong, S. Min, J. Baek, J. Kim, J. Chung, K. Jeong, Real-time reaction monitoring of azide–alkyne cycloadditions using benchtop NMR-based signal amplification by reversible exchange (SABRE), ACS Meas. Sci. Au 3 (2) (2023) 134–142, http://dx.doi.org/10.1021/acsmeasuresciau.2c00065.

[198] A.D. Robinson, P.M. Richardson, M.E. Halse, Hyperpolarised ^{1}H–^{13}C benchtop NMR spectroscopy, Appl. Sci. 9 (6) (2019) 1173, http://dx.doi.org/10.3390/app9061173.

[199] L.S. Lloyd, R.W. Adams, M. Bernstein, S. Coombes, S.B. Duckett, G.G.R. Green, R.J. Lewis, R.E. Mewis, C.J. Sleigh, Utilization of SABRE-derived hyperpolarization to detect low-concentration analytes via 1D and 2D NMR methods, J. Am. Chem. Soc. 134 (31) (2012) 12904–12907, http://dx.doi.org/10.1021/ja3051052.

[200] R.E. Mewis, K.D. Atkinson, M.J. Cowley, S.B. Duckett, G.G.R. Green, R.A. Green, L.A.R. Highton, D. Kilgour, L.S. Lloyd, J.A.B. Lohman, D.C. Williamson, Probing signal amplification by reversible exchange using an NMR flow system: Signal amplification by reversible exchange, Magn. Reson. Chem. 52 (7) (2014) 358–369, http://dx.doi.org/10.1002/mrc.4073.

[201] K. Jeong, S. Min, H. Chae, S.K. Namgoong, Monitoring of hydrogenation by benchtop NMR with parahydrogen-induced polarization, Magn. Reson. Chem. 57 (1) (2019) 44–48, http://dx.doi.org/10.1002/mrc.4791.

[202] D. Goł owicz, K. Kazimierczuk, M. Urbańczyk, T. Ratajczyk, Monitoring hydrogenation reactions using benchtop 2D NMR with extraordinary sensitivity and spectral resolution, ChemistryOpen 8 (2) (2019) 196–200, http://dx.doi.org/10.1002/open.201800294.

[203] P.M. TomHon, S. Han, S. Lehmkuhl, S. Appelt, E.Y. Chekmenev, M. Abolhasani, T. Theis, A versatile compact parahydrogen membrane reactor, ChemPhysChem 22 (24) (2021) 2526–2534, http://dx.doi.org/10.1002/cphc.202100667.

[204] S. Lehmkuhl, M. Wiese, L. Schubert, M. Held, M. Küppers, M. Wessling, B. Blümich, Continuous hyperpolarization with parahydrogen in a membrane reactor, J. Magn. Reson. 291 (2018) 8–13, http://dx.doi.org/10.1016/j.jmr.2018.03.012.

[205] F. Ellermann, P. Saul, J.-B. Hövener, A.N. Pravdivtsev, Modern manufacturing enables magnetic field cycling experiments and parahydrogen-induced hyperpolarization with a benchtop NMR, Anal. Chem. 95 (15) (2023) 6244–6252, http://dx.doi.org/10.1021/acs.analchem.2c03682.

[206] F. Ellermann, A. Sirbu, A. Brahms, C. Assaf, R. Herges, J.-B. Hövener, A.N. Pravdivtsev, Spying on parahydrogen-induced polarization transfer using a half-tesla benchtop MRI and hyperpolarized imaging enabled by automation, Nature Commun. 14 (1) (2023) 4774, http://dx.doi.org/10.1038/s41467-023-40539-9.

[207] A.N. Pravdivtsev, A.V. Yurkovskaya, H.-M. Vieth, K.L. Ivanov, Spin mixing at level anti-crossings in the rotating frame makes high-field SABRE feasible, Phys. Chem. Chem. Phys.: PCCP 16 (45) (2014) 24672–24675, http://dx.doi.org/10.1039/c4cp03765k.

[208] S.J. DeVience, R.L. Walsworth, M.S. Rosen, Preparation of nuclear spin singlet states using spin-lock induced crossing, Phys. Rev. Lett. 111 (17) (2013) 173002, http://dx.doi.org/10.1103/PhysRevLett.111.173002.

[209] A.N. Pravdivtsev, A.V. Yurkovskaya, N.N. Lukzen, K.L. Ivanov, H.-M. Vieth, Highly efficient polarization of spin-1/2 insensitive NMR nuclei by adiabatic passage through level anticrossings, J. Phys. Chem. Lett. 5 (19) (2014) 3421–3426, http://dx.doi.org/10.1021/jz501754j.

[210] A.N. Pravdivtsev, A.V. Yurkovskaya, H. Zimmermann, H.-M. Vieth, K.L. Ivanov, Transfer of SABRE-derived hyperpolarization to spin-1/2 heteronuclei, RSC Adv. 5 (78) (2015) 63615–63623, http://dx.doi.org/10.1039/C5RA13808F.

[211] T. Theis, N. Ariyasingha, R. Shchepin, J. Lindale, W. Warren, E. Chekmenev, Quasi-resonance signal amplification by reversible exchange, J. Phys. Chem. Lett. 9 (20) (2018) 6136–6142, http://dx.doi.org/10.1021/acs.jpclett.8b02669.

[212] R. Kircher, J. Xu, D.A. Barskiy, *In situ* hyperpolarization enables ^{15}N and ^{13}C benchtop NMR at natural isotopic abundance, J. Am. Chem. Soc. 146 (1) (2024) 514–520, http://dx.doi.org/10.1021/jacs.3c10030.

[213] J. Bargon, H. Fischer, U. Johnsen, Kernresonanz-emissionslinien während rascher radikalreaktionen: I. aufnahmeverfahren und beispiele, Z. Nat.forsch. A 22 (10) (1967) 1551–1555, http://dx.doi.org/10.1515/zna-1967-1014.

[214] H.R. Ward, R.G. Lawler, Nuclear magnetic resonance emission and enhanced absorption in rapid organometallic reactions, J. Am. Chem. Soc. 89 (21) (1967) 5518–5519, http://dx.doi.org/10.1021/ja00997a078.

[215] R. Kaptein, Chemically induced dynamic nuclear polarization. VIII. spin dynamics and diffusion of radical pairs, J. Am. Chem. Soc. 94 (18) (1972) 6251–6262, http://dx.doi.org/10.1021/ja00773a001.

[216] G.L. Closs, L.E. Closs, Induced dynamic nuclear spin polarization in reactions of photochemically and thermally generated triplet diphenylmethylene, J. Am. Chem. Soc. 91 (16) (1969) 4549–4550, http://dx.doi.org/10.1021/ja01044a041.

[217] G.L. Closs, A.D. Trifunac, Theory of chemically induced nuclear spin polarization. III. effect of isotropic g shifts in the components of radical pairs with one hyperfine interaction, J. Am. Chem. Soc. 92 (7) (1970) 2183–2184, http://dx.doi.org/10.1021/ja00710a092.

[218] R. Kaptein, J.L. Oosterhoff, Chemically induced dynamic nuclear polarization II: (relation with anomalous ESR spectra), Chem. Phys. Lett. 4 (4) (1969) 195–197, http://dx.doi.org/10.1016/0009-2614(69)80098-9.

[219] R. Kaptein, K. Dijkstra, K. Nicolay, Laser photo-CIDNP as a surface probe for proteins in solution, Nature 274 (5668) (1978) 293–294, http://dx.doi.org/10.1038/274293a0.

[220] O.B. Morozova, K.L. Ivanov, Time-resolved chemically induced dynamic nuclear polarization of biologically important molecules, ChemPhysChem 20 (2) (2019) 197–215, http://dx.doi.org/10.1002/cphc.201800566.

[221] F. Khan, I. Kuprov, T.D. Craggs, P.J. Hore, S.E. Jackson, 19F NMR studies of the native and denatured states of green fluorescent protein, J. Am. Chem. Soc. 128 (33) (2006) 10729–10737, http://dx.doi.org/10.1021/ja060618u.

[222] J. Hore, R. Broadhurst, Photo-CIDNP of biopolymers, Prog. Nucl. Magn. Reson. Spectrosc. 25 (4) (1993) 345–402, http://dx.doi.org/10.1016/0079-6565(93)80002-B.

[223] J. Bernarding, C. Bruns, I. Prediger, M. Plaumann, LED-based photo-CIDNP hyperpolarization enables 19F MR imaging and 19F NMR spectroscopy of 3-fluoro-DL-tyrosine at 0.6 T, Appl. Magn. Reson. 53 (10) (2022) 1375–1398, http://dx.doi.org/10.1007/s00723-022-01473-z.

[224] K.F. Sheberstov, L. Chuchkova, Y. Hu, I.V. Zhukov, A.S. Kiryutin, A.V. Eshtukov, D.A. Cheshkov, D.A. Barskiy, J.W. Blanchard, D. Budker, K.L. Ivanov, A.V. Yurkovskaya, Photochemically induced dynamic nuclear polarization of heteronuclear singlet order, J. Phys. Chem. Lett. 12 (19) (2021) 4686–4691, http://dx.doi.org/10.1021/acs.jpclett.1c00503.

[225] G.R. Stadler, T.F. Segawa, M. Bütikofer, V. Decker, S. Loss, B. Czarniecki, F. Torres, R.P. Riek, Fragment screening and fast micromolar detection on a benchtop NMR spectrometer boosted by photoinduced hyperpolarization, Angew. Chem. (Int. Ed. Engl.) (2023) e202308692, http://dx.doi.org/10.1002/anie.202308692.

[226] F. Torres, A. Sobol, J. Greenwald, A. Renn, O. Morozova, A. Yurkovskaya, R. Riek, Molecular features toward high photo-CIDNP hyperpolariztion explored through the oxidocyclization of tryptophan, Phys. Chem. Chem. Phys. 23 (11) (2021) 6641–6650, http://dx.doi.org/10.1039/D0CP06068B.

[227] F. Torres, A. Renn, R. Riek, Exploration of the close chemical space of tryptophan and tyrosine reveals importance of hydrophobicity in CW-photo-CIDNP performances, Magn. Reson. 2 (1) (2021) 321–329, http://dx.doi.org/10.5194/mr-2-321-2021.

[228] F. Torres, M. Bütikofer, G.R. Stadler, A. Renn, H. Kadavath, R. Bobrovs, K. Jaudzems, R. Riek, Ultrafast fragment screening using photo-hyperpolarized (CIDNP) NMR, J. Am. Chem. Soc. 145 (22) (2023) 12066–12080, http://dx.doi.org/10.1021/jacs.3c01392.

[229] P. Alonso-Moreno, I. Rodriguez, J.L. Izquierdo-Garcia, Benchtop NMR-based metabolomics: First steps for biomedical application, Metabolites 13 (5) (2023) http://dx.doi.org/10.3390/metabo13050614.

[230] B.C. Percival, M. Grootveld, M. Gibson, Y. Osman, M. Molinari, F. Jafari, T. Sahota, M. Martin, F. Casanova, M.L. Mather, M. Edgar, J. Masania, P.B. Wilson, Low-field, benchtop NMR spectroscopy as a potential tool for point-of-care diagnostics of metabolic conditions: Validation, protocols and computational models, High-Throughput 8 (1) (2018) 2, http://dx.doi.org/10.3390/ht8010002.

[231] Y. Rhee, E.R. Shilliday, Y. Matviychuk, T. Nguyen, N. Robinson, D.J. Holland, P.R.J. Connolly, M.L. Johns, Detection of honey adulteration using benchtop 1H NMR spectroscopy, Anal. Methods 15 (13) (2023) 1690–1699, http://dx.doi.org/10.1039/D2AY01757A.

[232] T. Parker, E. Limer, A.D. Watson, M. Defernez, D. Williamson, E.K. Kemsley, 60 MHz 1H NMR spectroscopy for the analysis of edible oils, TRAC Trends Anal. Chem. 57 (2014) 147–158, http://dx.doi.org/10.1016/j.trac.2014.02.006.

[233] D. Fallaise, H. Balkwill Tweedie, J. Konzuk, C. Cheyne, E.E. Mack, J.G. Longstaffe, Practical application of 1h benchtop NMR spectroscopy for the characterization of a nonaqueous phase liquid from a contaminated environment, Magn. Reson. Chem.: MRC (2018) http://dx.doi.org/10.1002/mrc.4816.

[234] S.L. Draper, E.R. McCarney, Benchtop nuclear magnetic resonance spectroscopy in forensic chemistry, Magn. Reson. Chem. n/a (n/a) (2021) http://dx.doi.org/10.1002/mrc.5197.

[235] A. Dey, B. Charrier, K. Lemaitre, V. Ribay, D. Eshchenko, M. Schnell, R. Melzi, Q. Stern, S.F. Cousin, J.G. Kempf, S. Jannin, J.-N. Dumez, P. Giraudeau, Fine optimization of a dissolution dynamic nuclear polarization experimental setting for 13C NMR of metabolic samples, Magn. Reson. 3 (2) (2022) 183–202, http://dx.doi.org/10.5194/mr-3-183-2022.

[236] A. Dey, B. Charrier, V. Ribay, J.-N. Dumez, P. Giraudeau, Hyperpolarized 1H and 13C NMR spectroscopy in a single experiment for metabolomics, Anal. Chem. 95 (46) (2023) 16861–16867, http://dx.doi.org/10.1021/acs.analchem.3c02614.

[237] C. Praud, V. Ribay, A. Dey, B. Charrier, J. Mandral, J. Farjon, J.-N. Dumez, P. Giraudeau, Optimization of heteronuclear ultrafast 2D NMR for the study of complex mixtures hyperpolarized by dynamic nuclear polarization, Anal. Methods 15 (45) (2023) 6209–6219, http://dx.doi.org/10.1039/D3AY01681A.

[238] V. Ribay, A. Dey, B. Charrier, C. Praud, J. Mandral, J.-N. Dumez, M.P.M. Letertre, P. Giraudeau, Hyperpolarized 13C NMR spectroscopy of urine samples at natural abundance by quantitative dissolution dynamic nuclear polarization, Angew. Chem. Int. Ed. 62 (27) (2023) e202302110, http://dx.doi.org/10.1002/anie.202302110.

[239] C. Bocquelet, N. Rougier, H.-N. Le, L. Veyre, C. Thieuleux, R. Melzi, A. Purea, D. Banks, J. Kempf, Q. Stern, E. Vaneeckhaute, S. Jannin, Boosting 1H and 13C NMR signals by orders of magnitude on a bench, 2024, http://dx.doi.org/10.26434/chemrxiv-2024-3nlnd.

[240] I. Reile, N. Eshuis, N.K.J. Hermkens, B.J.A.v. Weerdenburg, M.C. Feiters, F.P.J.T. Rutjes, M. Tessari, NMR detection in biofluid extracts at sub-microm concentrations via para-H2 induced hyperpolarization, Analyst 141 (13) (2016) 4001–4005, http://dx.doi.org/10.1039/C6AN00804F.

[241] L. Sellies, R.L.E.G. Aspers, M.C. Feiters, F.P.J.T. Rutjes, M. Tessari, Parahydrogen hyperpolarization allows direct NMR detection of alpha-amino acids in complex (bio)mixtures, Angew. Chem. Int. Ed. 60 (52) (2021) 26954–26959, http://dx.doi.org/10.1002/anie.202109588.

[242] N. Reimets, K. Ausmees, S. Vija, I. Reile, Developing analytical applications for parahydrogen hyperpolarization: Urinary elimination pharmacokinetics of nicotine, Anal. Chem. 93 (27) (2021) 9480–9485, http://dx.doi.org/10.1021/acs.analchem.1c01281.

[243] L. Frydman, T. Scherf, A. Lupulescu, The acquisition of multidimensional NMR spectra within a single scan, Proc. Natl. Acad. Sci. 99 (25) (2002) 15858–15862, http://dx.doi.org/10.1073/pnas.252644399.

[244] B. Gouilleux, B. Charrier, S. Akoka, F.-X. Felpin, M. Rodriguez-Zubiri, P. Giraudeau, Ultrafast 2D NMR on a benchtop spectrometer: Applications and perspectives, SI: Compact NMR, TRAC Trends Anal. Chem. 83 (2016) 65–75, http://dx.doi.org/10.1016/j.trac.2016.01.014.

[245] A.J. Parker, A. Dey, M. Usman Qureshi, J.M. Steiner, J.W. Blanchard, J. Scheuer, N. Tomek, S. Knecht, F. Josten, C. Müller, P. Hautle, I. Schwartz, P. Giraudeau, T.R. Eichhorn, J.-N. Dumez, Solution-state 2D NMR spectroscopy of mixtures HyperpolarizedUsing optically polarized crystals, Angew. Chem. Int. Ed. 62 (50) (2023) e202312302, http://dx.doi.org/10.1002/anie.202312302.

[246] V.Y. Orekhov, V.A. Jaravine, Analysis of non-uniformly sampled spectra with multi-dimensional decomposition, Prog. Nucl. Magn. Reson. Spectrosc. 59 (3) (2011) 271–292, http://dx.doi.org/10.1016/j.pnmrs.2011.02.002.

[247] T. Castaing-Cordier, S. Crasnier, D. Dubois, V. Ladroue, A. Buleté, C. Prudhomme, C. Charvoz, F. Besacier, D. Jacquemin, P. Giraudeau, J. Farjon, Non-uniform sampling to enhance the performance of compact NMR for characterizing new psychoactive substances, Magn. Reson. Chem. n/a (n/a) (2023) http://dx.doi.org/10.1002/mrc.5416.

[248] A. Jenne, W. Bermel, C.A. Michal, O. Gruschke, R. Soong, R. Ghosh Biswas, M. Bastawrous, A.J. Simpson, DREAMTIME NMR spectroscopy: Targeted multi-compound selection with improved detection limits, Angew. Chem. Int. Ed. 61 (19) (2022) e202110044, http://dx.doi.org/10.1002/anie.202110044.

[249] P. Kiraly, N. Kern, M.P. Plesniak, M. Nilsson, D.J. Procter, G.A. Morris, R.W. Adams, Single-scan selective excitation of individual NMR signals in overlapping multiplets, Angew. Chem. Int. Ed. 60 (2) (2021) 666–669, http://dx.doi.org/10.1002/anie.202011642.

[250] K. Zangger, Pure shift NMR, Prog. Nucl. Magn. Reson. Spectrosc. 86–87 (2015) 1–20, http://dx.doi.org/10.1016/j.pnmrs.2015.02.002.

[251] R.W. Adams, Pure shift NMR spectroscopy, in: EMagRes, John Wiley & Sons, Ltd, 2014, pp. 295–310, http://dx.doi.org/10.1002/9780470034590.emrstm1362.

[252] L. Castañar, Pure shift 1H NMR: what is next? Magn. Reson. Chem. 55 (1) (2017) 47–53, http://dx.doi.org/10.1002/mrc.4545.

[253] T. Castaing-Cordier, D. Bouillaud, P. Bowyer, O. Gonçalves, P. Giraudeau, J. Farjon, Highly resolved pure-shift spectra on a compact NMR spectrometer, ChemPhysChem 20 (5) (2019) 736–744, http://dx.doi.org/10.1002/cphc.201801116.

[254] K. Downey, W. Bermel, R. Soong, D.H. Lysak, K. Ronda, K. Steiner, P.M. Costa, W.W. Wolff, V. Decker, F. Busse, B. Goerling, A. Haber, M.J. Simpson, A.J. Simpson, Low-field, not low quality: 1D simplification, selective detection, and heteronuclear 2D experiments for improving low-field NMR spectroscopy of environmental and biological samples, Magn. Reson. Chem. 62 (5) (2024) 345–360, http://dx.doi.org/10.1002/mrc.5401.

[255] D. Taylor, L. Natrajan, M. Nilsson, R. Adams, SABRE-enhanced real-time pure shift NMR spectroscopy, Magn. Reson. Chem. (2021) http://dx.doi.org/10.1002/mrc.5206.

[256] P.L. Norcott, Selective NMR detection of individual reaction components hyperpolarised by reversible exchange with para-hydrogen, Phys. Chem. Chem. Phys. 24 (22) (2022) 13527–13533, http://dx.doi.org/10.1039/D2CP01657E.

[257] K.J. Donovan, L. Frydman, HyperBIRD: A sensitivity-enhanced approach to collecting homonuclear-decoupled proton NMR spectra, Angew. Chem. Int. Ed. 54 (2) (2015) 594–598, http://dx.doi.org/10.1002/anie.201407869.

[258] T.J. Trinklein, M. Thapa, L.A. Lanphere, J.A. Frost, S.M. Koresch, J.H. Aldstadt, Sequential injection analysis coupled to on-line benchtop proton NMR: Method development and application to the determination of synthetic cathinones in seized drug samples, Talanta 231 (2021) 122355, http://dx.doi.org/10.1016/j.talanta.2021.122355.

[259] T. Castaing-Cordier, A. Benavides Restrepo, D. Dubois, V. Ladroue, F. Besacier, A. Buleté, C. Charvoz, A. Goupille, D. Jacquemin, P. Giraudeau, J. Farjon, Characterization of new psychoactive substances by integrating benchtop NMR to multi-technique databases, Drug Test. Anal. 14 (9) (2022) 1629–1638, http://dx.doi.org/10.1002/dta.3332.

[260] L. Porwol, A. Henson, P.J. Kitson, D.-L. Long, L. Cronin, On the fly multi-modal observation of ligand synthesis and complexation of Cu complexes in flow with 'benchtop' NMR and mass spectrometry, Inorg. Chem. Front. 3 (7) (2016) 919–923, http://dx.doi.org/10.1039/C6QI00079G.

[261] D. Caramelli, J.M. Granda, S.H.M. Mehr, D. Cambié, A.B. Henson, L. Cronin, Discovering new chemistry with an autonomous robotic platform driven by a reactivity-seeking neural network, ACS Cent. Sci. 7 (11) (2021) 1821–1830, http://dx.doi.org/10.1021/acscentsci.1c00435.

[262] A.S. Kiryutin, V.P. Kozinenko, A.V. Yurkovskaya, Photo-SABRE: Nuclear spin hyperpolarization of *cis-trans* photoswitchable molecules by parahydrogen, Chemphotochem (2023) http://dx.doi.org/10.1002/cptc.202300151.

[263] E.E. Brown, I. Mandzhieva, P.M. TomHon, T. Theis, F.N. Castellano, Triplet photosensitized para-hydrogen induced polarization, ACS Cent. Sci. 8 (11) (2022) 1548–1556, http://dx.doi.org/10.1021/acscentsci.2c01003.

[264] M.E. Halse, B. Procacci, S.-L. Henshaw, R.N. Perutz, S.B. Duckett, Coherent evolution of parahydrogen induced polarisation using laser pump, NMR probe spectroscopy: Theoretical framework and experimental observation, J. Magn. Reson. 278 (2017) 25–38, http://dx.doi.org/10.1016/j.jmr.2017.03.005.

[265] B. Procacci, P.M. Aguiar, M.E. Halse, R.N. Perutz, S.B. Duckett, Photochemical pump and NMR probe to monitor the formation and kinetics of hyperpolarized metal dihydrides, Chem. Sci. 7 (12) (2016) 7087–7093, http://dx.doi.org/10.1039/C6SC01956K.

[266] C. Hilty, D. Kurzbach, L. Frydman, Hyperpolarized water as universal sensitivity booster in biomolecular NMR, Nat. Protoc. 17 (7) (2022) 1621–1657, http://dx.doi.org/10.1038/s41596-022-00693-8.

[267] L.M. Epasto, K. Che, F. Kozak, A. Selimovic, P. Kadeřávek, D. Kurzbach, Toward protein NMR at physiological concentrations by hyperpolarized water— Finding and mapping uncharted conformational spaces, Sci. Adv. 8 (31) (2022) eabq5179, http://dx.doi.org/10.1126/sciadv.abq5179.

[268] P. Kadeřávek, F. Ferrage, G. Bodenhausen, D. Kurzbach, High-resolution NMR of folded proteins in hyperpolarized physiological solvents, Chemistry – Eur. J. 24 (51) (2018) 13418–13423, http://dx.doi.org/10.1002/chem.201802885.

[269] M. Negroni, D. Kurzbach, Residue-resolved monitoring of protein hyperpolarization at sub-second time resolution, Commun. Chem. 4 (1) (2021) 1–7, http://dx.doi.org/10.1038/s42004-021-00587-y.

[270] J. Hu, J. Kim, C. Hilty, Detection of protein–ligand interactions by 19F nuclear magnetic resonance using hyperpolarized water, J. Phys. Chem. Lett. 13 (17) (2022) 3819–3823, http://dx.doi.org/10.1021/acs.jpclett.2c00448.

[271] Y. Lee, H. Zeng, S. Ruedisser, A.D. Gossert, C. Hilty, Nuclear magnetic resonance of hyperpolarized fluorine for characterization of protein–ligand interactions, J. Am. Chem. Soc. 134 (42) (2012) 17448–17451, http://dx.doi.org/10.1021/ja308437h.

[272] P. Pham, C. Hilty, Biomolecular interactions studied by low-field NMR using SABRE hyperpolarization, Chem. Sci. 14 (37) (2023) 10258–10263, http://dx.doi.org/10.1039/d3sc02365f.

[273] B. Picard, B. Gouilleux, T. Lebleu, J. Maddaluno, I. Chataigner, M. Penhoat, F.-X. Felpin, P. Giraudeau, J. Legros, Oxidative neutralization of mustard-gas simulants in an on-board flow device with in-line NMR monitoring, Angew. Chem. Int. Ed. 56 (26) (2017) 7568–7572, http://dx.doi.org/10.1002/anie.201702744.

[274] P. Giraudeau, F.-X. Felpin, Flow reactors integrated with in-line monitoring using benchtop NMR spectroscopy, React. Chem. Eng. 3 (4) (2018) 399–413, http://dx.doi.org/10.1039/C8RE00083B.

[275] A. Friebel, E. von Harbou, K. Münnemann, H. Hasse, Online process monitoring of a batch distillation by medium field NMR spectroscopy, Chem. Eng. Sci. 219 (2020) 115561, http://dx.doi.org/10.1016/j.ces.2020.115561.

[276] V. Sans, L. Porwol, V. Dragone, L. Cronin, A self optimizing synthetic organic reactor system using real-time in-line NMR spectroscopy, Chem. Sci. 6 (2) (2015) 1258–1264, http://dx.doi.org/10.1039/C4SC03075C.

[277] P. Štěpánek, C. Sanchez-Perez, V.-V. Telkki, V.V. Zhivonitko, A.M. Kantola, High-throughput continuous-flow system for SABRE hyperpolarization, J. Magn. Reson. 300 (2019) 8–17, http://dx.doi.org/10.1016/j.jmr.2019.01.003.

[278] K.V. Kovtunov, L.M. Kovtunova, M.E. Gemeinhardt, A.V. Bukhtiyarov, J. Gesiorski, V.I. Bukhtiyarov, E.Y. Chekmenev, I.V. Koptyug, B.M. Goodson, Heterogeneous microtesla SABRE enhancement of 15N NMR signals, Angew. Chem. (Int. ed. Engl.) 56 (35) (2017) 10433–10437, http://dx.doi.org/10.1002/anie.201705014.

[279] S. Min, J. Baek, J. Kim, H.J. Jeong, J. Chung, K. Jeong, Water-compatible and recyclable heterogeneous SABRE catalyst for NMR signal amplification, JACS Au 3 (10) (2023) 2912–2917, http://dx.doi.org/10.1021/jacsau.3c00487.

[280] E.W. Zhao, R. Maligal-Ganesh, Y. Du, T.Y. Zhao, J. Collins, T. Ma, L. Zhou, T.-W. Goh, W. Huang, C.R. Bowers, Surface-mediated hyperpolarization of liquid water from parahydrogen, Chem 4 (6) (2018) 1387–1403, http://dx.doi.org/10.1016/j.chempr.2018.03.004.

[281] B.A. Rodin, J. Eills, R. Picazo-Frutos, K.F. Sheberstov, D. Budker, K.L. Ivanov, Constant-adiabaticity ultralow magnetic field manipulations of parahydrogen-induced polarization: application to an AA'X spin system, Phys. Chem. Chem. Phys. 23 (12) (2021) 7125–7134, http://dx.doi.org/10.1039/D0CP06581A.

[282] T.B.R. Robertson, L.J. Clarke, R.E. Mewis, Rapid SABRE catalyst scavenging using functionalized silicas, Molecules 27 (2) (2022) 332, http://dx.doi.org/10.3390/molecules27020332.

[283] M. Gierse, L. Dagys, M. Keim, S. Lucas, F. Josten, M.B. Plenio, I. Schwartz, S. Knecht, J. Eills, Hyperpolarizing small molecules using parahydrogen and solid-state spin diffusion, Angew. Chem. Int. Ed. (2024) e202319341, http://dx.doi.org/10.1002/anie.202319341.

[284] T.R. Eichhorn, A.J. Parker, F. Josten, C. Müller, J. Scheuer, J.M. Steiner, M. Gierse, J. Handwerker, M. Keim, S. Lucas, M.U. Qureshi, A. Marshall, A. Salhov, Y. Quan, J. Binder, K.D. Jahnke, P. Neumann, S. Knecht, J.W. Blanchard, M.B. Plenio, F. Jelezko, L. Emsley, C.C. Vassiliou, P. Hautle, I. Schwartz, Hyperpolarized solution-state NMR spectroscopy with optically polarized crystals, J. Am. Chem. Soc. 144 (6) (2022) 2511–2519, http://dx.doi.org/10.1021/jacs.1c09119.

Abbreviations

ALTADENA: Adiabatic Longitudinal Transport After Dissociation Engenders Net Alignment.

CE: Cross Effect.

CIDNP: Chemically-Induced Dynamic Nuclear Polarisation.

dDNP: Dissolution Dynamic Nuclear Polarisation.

DNP: Dynamic Nuclear Polarisation.

DQ: Double Quantum.

DREAMTIME: Designed Refocused Excitation And optional Mixing for Targets In vivo and Mixture Elucidation.

EPR: Electron Paramagnetic Resonance.

GEMSTONE: Gradient-Enhanced Multiplet-Selective Targeted-Observation NMR Experiment.

HYPNOESYS: Hyperpolarized Nuclear Overhauser Effect System.

IR: Infrared.

LAC: Level Anti-Crossing.

LDH: Lactate Dehydrogenase.

MAS: Magic Angle Spinning.

MRI: Magnetic Resonance Imaging.

MW: Microwave.

NHC: N-Heterocyclic Carbene.

NMR: Nuclear Magnetic Resonance.

NUS: Non-Uniform Sampling.

ODNP: Overhauser Dynamic Nuclear Polarisation.

OE: Overhauser Effect.

*PASADENA: Para*hydrogen And Synthesis Allow Dramatically Enhanced Nuclear Alignment.

PHIP: Para-Hydrogen Induced Polarisation.

RF: Radiofrequency.

SABRE: Signal Amplification By Reversible Exchange.

SE: Solid Effect.

SEOP: Spin-Exchange Optical Pumping.

SLIC: Spin-Lock Induced Crossing.

SWAMP: Surface Waters Are Magnetised by Parahydrogen.

TM: Thermal Mixing.

TR-NUS: Time-Resolved Non-Uniform Sampling.

UF: Ultrafast.

UV: Ultraviolet.

ZQ: Zero Quantum.

ZULF: Zero-to-Ultra-Low Field.